

AD-A259 923



4

THE UNIVERSITY OF  
**ARIZONA**

TUCSON ARIZONA

FINAL REPORT

**DTIC**

**LECTE**

JAN 22 1993

**B D**

**NUMERICAL SIMULATIONS OF THE  
CONTROL OF WAVE PACKET DISTURBANCES IN THE  
BOUNDARY LAYER ON A FLAT PLATE**

by

Peter A. Dittrich and Hermann F. Fasel

Prepared from work done under Grant

ONR-N000-14-90-J-1274

Department of Aerospace and Mechanical Engineering  
University of Arizona  
Tucson, Arizona 85721  
October 1992

93-01082



15/88

# REPORT DOCUMENTATION PAGE

Form Approved  
OMB No. 0704-0188

Public reporting burden for this collection of information is estimated to average 1 hour per response, including the time for reviewing instructions, searching existing data sources, gathering and maintaining the data needed, and completing and reviewing the collection of information. Send comments regarding this burden estimate or any other aspect of the collection of information, including suggestions for reducing the burden, to Washington Headquarters Services, Directorate for Information Operations and Reports, 1215 Jefferson Davis Highway, Suite 1204, Arlington, VA 22202-4302, and to the Office of Management and Budget, Paperwork Reduction Project (0704-0188), Washington, DC 20503.

<b>1. AGENCY USE ONLY (Leave blank)</b>		<b>2. REPORT DATE</b> 11/12/92	<b>3. REPORT TYPE AND DATES COVERED</b> Final	
<b>4. TITLE AND SUBTITLE</b> Numerical Simulations of the Control of Wave Packet Disturbances in the Boundary Layer on a Flat Plate			<b>5. FUNDING NUMBERS</b> GN00014-90-J-1274	
<b>6. AUTHOR(S)</b> Peter A. Dittrich & Hermann F. Fasel				
<b>7. PERFORMING ORGANIZATION NAME(S) AND ADDRESS(ES)</b> Department of Aerospace & Mechanical Engineering College of Engineering & Mines The University of Arizona Tucson, AZ 85721			<b>8. PERFORMING ORGANIZATION REPORT NUMBER</b>	
<b>9. SPONSORING/MONITORING AGENCY NAME(S) AND ADDRESS(ES)</b> Department of the Navy Office of the Chief of Naval Research 800 N. Quincy Street, CODE 1513:MBL Arlington, VA 22217-5000			<b>10. SPONSORING/MONITORING AGENCY REPORT NUMBER</b>	
<b>11. SUPPLEMENTARY NOTES</b>				
<b>12a. DISTRIBUTION/AVAILABILITY STATEMENT</b> Approved for public release; distribution unlimited.			<b>12b. DISTRIBUTION CODE</b>	
<b>13. ABSTRACT (Maximum 200 words)</b>  The control of laminar turbulent transition in incompressible flat plate boundary layers is investigated using direct numerical simulations. The investigations focus in particular on the control of wave packet disturbances that are characteristic for natural transition. A fully implicit finite-difference/spectral method was developed to solve the governing equations. Wave packet disturbances are created by simulating the effect of thermally activated heater elements on the plate surface. Through controlled spanwise variation of the temperature of the heater elements, both two- and three-dimensional wave packet disturbances could be investigated. A transfer function technique was developed for the control strategy, where the transfer function is obtained directly from the numerical simulations. With this technique low amplitude, two-dimensional wave packet disturbances could be almost completely cancelled. Using a modified transfer function technique the control of three-dimensional wave packets was also very successful. It was found that the attenuation of only the two-dimensional components of a three-dimensional wave packet considerably delays the onset of the nonlinear interactions of the oblique modes.				
<b>14. SUBJECT TERMS</b> Direct Numerical Simulations, Transition Control, Wave Packets Laminar - Turbulent Transition, Computational Fluid Dynamics			<b>15. NUMBER OF PAGES</b> 151	
			<b>16. PRICE CODE</b>	
<b>17. SECURITY CLASSIFICATION OF REPORT</b> Unclassified	<b>18. SECURITY CLASSIFICATION OF THIS PAGE</b> Unclassified	<b>19. SECURITY CLASSIFICATION OF ABSTRACT</b> Unclassified	<b>20. LIMITATION OF ABSTRACT</b> UL	

FINAL REPORT

NUMERICAL SIMULATIONS OF THE  
CONTROL OF WAVE PACKET DISTURBANCES IN THE  
BOUNDARY LAYER ON A FLAT PLATE

by

Peter A. Dittrich and Hermann F. Fasel

Prepared from work done under Grant

ONR-N000-14-90-J-1274

Department of Aerospace and Mechanical Engineering  
University of Arizona  
Tucson, Arizona 85721  
October 1992

## TABLE OF CONTENTS

TABLE OF CONTENTS .....	5
LIST OF ILLUSTRATIONS .....	7
ABSTRACT .....	14
1. INTRODUCTION .....	16
1.1 Background .....	16
1.2 Linear Theory .....	19
1.3 Wave Packets .....	21
1.4 Control .....	22
1.5 Problem Statement .....	26
2. GOVERNING EQUATIONS .....	29
2.1 Equations for Two-Dimensional Flow .....	29
2.1.1 Boundary Conditions .....	32
2.2 Equations for Three-Dimensional Flow .....	35
2.2.1 Boundary Conditions .....	38
3. NUMERICAL METHOD .....	41
3.1 Calculation of Two-Dimensional Flow .....	42
3.2 Calculation of Three-Dimensional Flow .....	43
4. RESULTS .....	48
4.1 Computation of Two-Dimensional Flows .....	48
4.1.1 Wave Packet Disturbances .....	49
4.1.2 Passive Heated Segments .....	55
4.1.3 Transfer Function Concept .....	59
4.1.4 Boundary Layer Control of Two-Dimensional Wave Packets .....	61

4.2 Computation of Three-Dimensional Flows .....	64
4.2.1 Linear Spatial Stability Theory .....	65
4.2.2 Three-Dimensional Wave Packet Disturbances .....	68
4.2.3 Boundary Layer Control of Three-Dimensional Disturbances Waves	75
4.2.3.1 Control of the Two-Dimensional and Three-Dimensional	
Spanwise Mode .....	76
4.2.3.2 Control of the Two-Dimensional Mode .....	77
5. CONCLUSIONS .....	78
FIGURES .....	82
APPENDIX A: Fourier Transform of Non-Periodic Signals and Estimation of the	
Transfer Function .....	141
APPENDIX B: Finite Difference Approximations for the Energy	
Equation .....	145
LIST OF REFERENCES .....	148

DTIC QUALITY INSPECTED 5

<b>Accession For</b>	
NTIS GRA&I	<input checked="" type="checkbox"/>
DTIC TAB	<input type="checkbox"/>
Unannounced	<input type="checkbox"/>
Justification	
By _____	
Distribution/	
Availability Codes	
Dist	Avail and/or Special
A-1	

## List of Illustrations

Fig. 1:	Computational domain with flat plate model. ....	82
Fig. 2:	Computational domain in the x-y plane.....	82
Fig. 3:	Linear stability diagram and the modulus of the input spectrum of the first heater strip.....	83
Fig. 4:	Disturbance signal of wall vorticity at several timesteps. The heater strip location is at $20 \leq x/\Delta x \leq 30$ and the forcing is turned off at $t/\Delta t = 40$ . (Case with zero mean temperature over heater strip). ....	84
Fig. 5:	Temperature contours (grey-shaded) and lines of constant streamwise velocity.....	85
Fig. 6:	Disturbance signal of wall vorticity domain at several timesteps with the temperature forcing turned off at $t/\Delta t = 40$ . The heater strip location is at $30 \leq x/\Delta x \leq 40$ (Case with steady mean temperature over heater strip). ....	86
Fig. 7:	Perspective representation of the disturbance signal for a) $u'$ the streamwise velocity component, b) $v'$ the wall normal velocity component, c) $\omega'$ the vorticity and d) $\theta'$ the temperature at five time levels. ....	87
Fig. 8:	Amplitude- and Phase- spectra of the wall vorticity signal at several streamwise positions for the case with no control applied. ....	91
Fig. 9:	Amplitude- and Phase- spectra of the wall normal velocity signal at $y/\Delta y = 20$ at several streamwise positions for the case with no control applied. ....	92

- Fig. 10: Dispersion relation of the wall vorticity signal from a Navier-Stokes simulation at the streamwise position  $x/\Delta x = 140$ , ( $Re_{\delta_1} = 835$ ).....93
- Fig. 11: Comparison of a) the phase velocity  $c_{ph}$  and b) the rate of amplification  $\alpha_i$  of the Navier-Stokes calculation (solid line) with the linear spatial stability theory ('+' symbols) at the streamwise position,  $x/\Delta x = 140$ , ( $Re_{\delta_1} = 835$ ), by analyzing the wall vorticity signal of the Navier-Stokes simulation.....94
- Fig. 12: Comparison of a) the phase velocity  $c_{ph}$  and b) the rate of amplification  $\alpha_i$  of the Navier-Stokes calculation (solid line) with the linear spatial stability theory ('+' symbols) at the streamwise position  $x/\Delta x = 140$ , ( $Re_{\delta_1} = 835$ ), by analyzing the wall normal velocity signal at  $y/\Delta y = 30$  of the Navier-Stokes simulation.....95
- Fig. 13: Comparison of a) the phase velocity  $c_{ph}$  and b) the rate of amplification  $\alpha_i$  of the Navier-Stokes calculation (solid line) with the linear spatial stability theory ('+' symbols) at the streamwise position  $x/\Delta x = 140$ , ( $Re_{\delta_1} = 835$ ), by analyzing the vorticity signal at  $y/\Delta y = 20$  of the Navier-Stokes simulation..... 96
- Fig. 14: Streamwise amplification of the wall vorticity for several frequency components of the wave packet disturbance with a) the presence of a heated segment on the plate surface (steady wall temperature distribution shown below figure) and b) without the heated segment. .... 97
- Fig. 15: Comparison of the streamwise amplification of four frequency components of the wave packet disturbance with a steady (passive) heater temperature between  $70 \leq x/\Delta x \leq 90$  (solid line) and without a heater strip (dashed line) for a) the wall vorticity, b) the wall normal velocity component  $y/\Delta y = 10$ .....98

- Fig. 16: Comparison of the rate of amplification  $-\alpha_i$  of the wall vorticity signal at  $x/\Delta x=140$  for the case with the passive heater (at  $70 \leq x/\Delta x \leq 90$ ) and without the passive heater present. ....100
- Fig. 17: Steady streamwise velocity  $u_{\text{base}}$  and vorticity  $\omega_{\text{base}}$  profiles at position  $x/\Delta x=100$ ,  $Re_{\delta 1} = 772$  for the case without the passive heater and the difference of  $u_{\text{base}}$  and  $\omega_{\text{base}}$  for the case with the heater and the case without the passive heater. ....101
- Fig. 18: The a) steady pressure gradient in streamwise direction  $dp/dx = \nu (d^2 u/dy^2) - (dv/d\theta) (d\theta/dy) (du/dy)$  at the wall surface ( $y=0$ ) and b) the steady wall temperature for two heaters. ...102
- Fig. 19: Schematic representation of the transfer function technique relating the temperature input at location  $x_0$  to a wall vorticity response at  $x_1$ . ....103
- Fig. 20: Modulus of the transfer function at the streamwise position  $x/\Delta x = 70$  for three different heater strip lengths  $N = 10$  ( $30 \leq x/\Delta x \leq 40$ ),  $N = 20$  ( $30 \leq x/\Delta x \leq 50$ ) and  $N = 30$  ( $30 \leq x/\Delta x \leq 60$ ). ....104
- Fig. 21: Modulus of transfer function at several streamwise positions for the heater strip width  $70 \leq x/\Delta x \leq 80$ . ....105
- Fig. 22: Temperature control signal  $T'_{\text{control}}$  for the controller strip. .... 106
- Fig. 23: Amplitude- and Phase- spectra of the wall vorticity signal at several streamwise positions, with control applied..... 107
- Fig. 24: Amplitude- and Phase- spectra of the wall normal velocity signal at  $y/\Delta y = 20$  at several streamwise positions, with control applied.....108

- Fig. 25: The a) rate of amplification, b) the phase velocity and c) the ratio of the spanwise to streamwise wave number from the linear spatial stability theory at two streamwise positions  $Re_{\delta 1} = 800, 1200$ , for  $\gamma = 0$ , and four oblique modes  $\gamma = 10, 20, 30, 40$ . .....109
- Fig. 26: Instantaneous wall temperature at  $t/\Delta t = 70$  with spanwise forcing of the first heater strip and a passive second heater.....111
- Fig. 27: Disturbance signal of the spanwise vorticity  $\omega'_{z, k=0}$  at several time levels for a) the two-dimensional mode, and b) the three-dimensional spanwise mode. End of forcing is at  $t/\Delta t = 120$ . .....112
- Fig. 28: Disturbance signal of the wall normal velocity  $v'_{k=0}$  at  $y/\Delta y = 40$  at several time levels for, a) the two-dimensional spanwise mode, and b) the three-dimensional spanwise mode. End of forcing is at  $t/\Delta t = 120$ . .....114
- Fig. 29: Streamwise disturbance velocity component at  $t/\Delta t = 130$  for a) the two-dimensional mode  $u'_{k=0}$  and b) the three-dimensional spanwise mode  $u'_{k=1}$  with no control applied. .... 116
- Fig. 30: Streamwise disturbance velocity component at  $t/\Delta t = 1200$ , for a) the two-dimensional mode  $u'_{k=0}$  and b) the three-dimensional spanwise mode  $u'_{k=1}$  with no control applied..... 117
- Fig. 31: Spanwise vorticity disturbance at  $t/\Delta t = 1200$  for a) the two-dimensional mode  $\omega_{z, k=0}$  and b) the three-dimensional spanwise mode  $\omega_{z, k=1}$  with no control applied. ....118
- Fig. 32: Amplitude- and Phase- spectra of the spanwise wall vorticity signal for a) the two-dimensional mode  $\omega'_{z, k=0}$  and for b) the three-dimensional mode  $\omega'_{z, k=1}$  with no control applied, at  $x/\Delta x = 90, 100, 110, 120, 130$  .....119

- Fig. 33: Amplitude- and Phase- spectra of the wall normal velocity signal at  $y/\Delta y=40$  for a) the two-dimensional mode  $v'_{k=0}$  and for b) the three-dimensional mode  $v'_{k=1}$  with no control applied, at  $x/\Delta x = 90,100,110,120,130$ . .....120
- Fig. 34: Amplitude- and Phase- spectra of the spanwise vorticity signal with no control applied, for a) the two-dimensional mode  $\omega'_{z k=0}$  at the wall surface and b) the three-dimensional mode  $\omega'_{z k=1}$  at the wall surface, and for c) the three-dimensional mode  $\omega'_{z k=1}$  at  $y/\Delta y = 10$ , at the streamwise positions  $x/\Delta x = 180, 260, 340, 420, 500$ . .....121
- Fig. 35: Amplitude- and Phase- spectra of the wall normal velocity signal at  $y/\Delta y=40$  for a) the two-dimensional mode  $v'_{k=0}$  and for b) the three-dimensional mode  $v'_{k=1}$  with no control applied, at  $x/\Delta x = 180,260,340,420,500$ . .....123
- Fig. 36: Comparison of the experimental amplitude spectra with the computed spectra of the linear spatial stability theory from Gaster and Grant (1975). The measured spectra are taken at a wall normal distance outside the boundary layer  $y/\delta = 1.1$ . .....124
- Fig. 37: Comparison of the phase velocities at  $x/\Delta x = 460$ , ( $Re_{\delta_1} = 1021$ ) with the linear stability theory ('+' symbols) for the two-dimensional ( $k=0$ ) and the three-dimensional ( $k=1$ ) spanwise modes of the wall normal velocity  $v'$  at  $y/\Delta y = 40$ . .....125
- Fig. 38: The streamwise velocity component  $u'$  in the horizontal plane at the disturbance maximum (grey-shaded contours) and the wall temperature disturbance  $\theta'$  (line contours) at  $t/\Delta t = 70$  during the forcing cycle. ....126
- Fig. 39: The wall normal velocity component  $v'$  in the horizontal plane at the disturbance maximum (grey-shaded contours) and the wall temperature disturbance  $\theta'$  (line contours) at  $t/\Delta t = 70$  during the forcing cycle. ....127

- Fig. 40: The spanwise velocity component  $w'$  in the horizontal plane at the disturbance maximum (grey-shaded contours) and the wall temperature disturbance  $\theta'$  (line contours) at  $t/\Delta t = 70$  during the forcing cycle. ....128
- Fig. 41: The streamwise vorticity  $\omega'_x$  in the horizontal plane at the disturbance maximum (grey-shaded contours) and the wall temperature disturbance  $\theta'$  (line contours) at  $t/\Delta t = 70$  during the forcing cycle.....129
- Fig. 42: The wall normal vorticity  $\omega'_y$  in the horizontal plane at the disturbance maximum (grey-shaded contours) and the wall temperature disturbance  $\theta'$  (line contours) at  $t/\Delta t = 70$  during the forcing cycle.....130
- Fig. 43: The spanwise vorticity  $\omega'_z$  in the horizontal plane at the disturbance maximum (grey-shaded contours) and the wall temperature disturbance  $\theta'$  (line contours) at  $t/\Delta t = 70$  during the forcing cycle.....131
- Fig. 44: The streamwise vorticity  $\omega'_x$  in the horizontal plane at the plate surface (grey-shaded contours) and the spanwise vorticity  $\omega'_z$  (line contours) at  $t/\Delta t = 1200$ .....132
- Fig. 45: Modulus and argument of the transfer function at several streamwise positions with the heater strip width  $130 \leq x/\Delta x \leq 145$  for a) the two-dimensional mode ( $k=0$ ) and b) the three-dimensional spanwise horizontal mode ( $k=1$ ). ....133
- Fig. 46: Amplitude- and Phase- spectra of the spanwise vorticity signal  $\omega'_{z,k=0}$  at the wall surface for the two- dimensional mode at several streamwise positions, with control applied. The control strip is at  $130 \leq x/\Delta x \leq 145$ .....135

- Fig. 47: Amplitude- and Phase- spectra of the spanwise vorticity signal  $\omega'_{z,k=1}$  at  $y/\Delta y=10$  for the three-dimensional mode at several streamwise positions, with control applied. The control strip is at  $130 \leq x/\Delta x \leq 145$ ..... 136
- Fig. 48: Amplitude- and Phase- spectra of the wall normal velocity signal  $v'_{k=0}$  at  $y/\Delta y=40$ , for the two-dimensional spanwise mode at several streamwise positions with control applied. The control strip is at  $130 \leq x/\Delta x \leq 145$ ..... 137
- Fig. 49: Amplitude- and Phase- spectra of the wall normal velocity signal  $v'_{k=1}$  at  $y/\Delta y=40$ , for the three-dimensional spanwise mode at several streamwise positions with control applied. The control strip is at  $130 \leq x/\Delta x \leq 145$ .....138
- Fig. 50: The spanwise vorticity  $\omega'_z$  in the horizontal plane at the plate surface for the control of the two-dimensional spanwise mode only (grey-shaded contours) and the spanwise vorticity  $\omega'_z$  for no control (line contours) at  $t/\Delta t = 1200$  .....139
- Fig. 51: Amplitude and Phase-spectra for the case of only the two-dimensional mode attenuated, for a) the three-dimensional wall normal velocity  $v'_{k=1}$  at  $y/\Delta y=40$  and b) the three-dimensional spanwise vorticity  $\omega'_{z,k=1}$  at  $y/\Delta y=10$ .....140

## Abstract

The control of the transition from laminar to turbulent flow in a boundary layer of a flat plate is investigated using numerical simulations. The numerical model is based on the incompressible Navier-Stokes equations, which are coupled with the energy equation through the temperature dependent viscosity. A fully implicit finite-difference spectral method was used to solve the governing equations. The numerical model allows for the spatial evolution of the disturbances in a non-parallel boundary layer. Active control of wave packet disturbances in the non-isothermal boundary layer is studied in detail. Wave packet disturbances are created in the flow field by simulating the effect of thermally activated heater elements on the plate surface. Through a controlled spanwise variation of the temperature of the heater elements, two- and three-dimensional wave packet disturbances can be studied. The propagation and amplification of the wave packet disturbances in the boundary layer is examined. The heater elements on the plate surface act as locally strong heat sources causing thermal wakes within the boundary layer that spread in the downstream direction. A transfer function technique is used for the control strategy. The transfer function is based on the vorticity response to a finite temperature fluctuation at the heater strip and is obtained from the numerical simulations. With additional heater segments (controller) located downstream of an excitation source, the possibility of attenuating wave packet disturbances is investigated. With the numerical transfer function, a successful control strategy for the wave packet cancellation could be developed. Initially, for the low amplitude, two-dimensional disturbances in the transition process the wave packet disturbances could be almost completely cancelled. For the attenuation of three-dimensional wave packet disturbances, the transfer function technique was extended to allow for spanwise variations. The attenuation of three-

dimensional wave packets with the modified transfer function technique was almost equally as successful as for the purely two-dimensional flow disturbances. For the simulation of the three-dimensional flow development with no control applied, nonlinear interaction of wave components of the wave packet first appeared for the oblique modes in the low frequency range, which was also observed in experimental investigations. The attenuation of only the two-dimensional components of a three-dimensional wave packet disturbance delays the onset of the nonlinear interaction of the oblique spanwise modes in the lower frequency range.

## 1. Introduction

The study of laminar to turbulent transition for wall bounded shear flows is of great practical interest for the application of flow control. The delay of transition from laminar to turbulent flow at high Reynolds numbers reduces the friction drag on streamlined bodies. The effective control of laminar flow, for example to extend the regime of laminar flow on the surface of airplane wings, may lead to an increased range and speed, or reduced fuel costs of an airplane. On the other hand, in processes where the mixing of the fluid properties is desirable in order to improve momentum, energy or mass transport, an acceleration of transition to the turbulent state is advantageous. Applications of the control of laminar flow were reviewed in great detail by Bushnell and Malik (1985), and more recently, by Wagner et al. (1989). The present numerical investigation employs the flat plate model of a boundary layer flow in water. The instability mechanisms leading to turbulence are reviewed first to gain insight into the relevant issues prior to the discussion of laminar flow control.

### 1.1 Background

One route of transition to turbulence begins with the occurrence of small amplitude, two-dimensional disturbance waves (Tollmien Schlichting waves). These disturbance waves propagate in the direction of the flow. The development of these disturbances, that is amplification or decay, can be closely predicted by the linear stability theory. At later stages the Tollmien Schlichting (TS) waves develop a spanwise periodic, three-dimensional deformation, and associated with this is the formation of longitudinal vortices. In the experiments of Klebanoff et al. (1962), this behavior was enhanced by placing physical geometric disturbances on the plate surface at selected spanwise intervals. A very regular peak-valley structure appeared (regions of

enhanced and reduced amplitudes) with the peaks corresponding to regions of maximum wave amplification and the valleys to regions of minimum amplification.

The growth rates at the peak positions in the Klebanoff pattern are much larger than the original TS growth rates and subsequently a localized high shear layer is formed. Then, shortly after, highly nonlinear processes lead to breakdown and to turbulent spots, which spread to form a fully turbulent boundary layer.

Unlike the above mentioned route to transition, at somewhat lower amplitude levels (between 0.2% and 1% of the free stream velocity), Saric and Thomas (1983), and Kachanov and Levchenko (1984) observed a different pattern. Instead of an aligned pattern seen in the experiments of Klebanoff et al. where peaks followed peaks, and valleys followed valleys, this alternative pattern consisted of a staggered structure, i.e. peaks followed valleys and vice versa.

The staggered structure at the lower initial forcing amplitudes leads to a strong amplification of the subharmonic mode, and also to the growth of a broad band of lower frequency disturbances. Kachanov and Levchenko (1984) did not observe the characteristic high frequency stages of the Klebanoff type transition. In addition to the above mentioned routes to turbulence, certain bypass mechanisms may occur, that is, if the external forcing results in large enough amplitudes in the initial stages, nonlinear effects may trigger breakdown to turbulent flow in a more direct manner.

In an early theoretical study on the breakdown process, Craik (1971) proposed a weakly nonlinear resonance model based on the interaction of a two-dimensional and two three-dimensional oblique modes with opposite signs. The resonance interaction would involve modes whose phase velocities match in streamwise direction. In this theory, which is based on the temporal amplification, this would typically involve three-dimensional wavenumbers  $\alpha_{3D} = 1/2 \alpha_{2D}$ . However, the relatively large distur-

bances observed in Klebanoff's experiment could not be explained by Craik's theory.

Much later the experiments by Saric and Thomas (1983), and Kachanov and Levchenko (1984) provided clear evidence of the existence of the subharmonic mode. In the smoke wire flow visualizations by Saric and Thomas two different peak-valley structures were identified. For a very low initial disturbance amplitude (.3% based on the free stream velocity) the spanwise wavenumbers matched Craik's theory well. A spanwise to streamwise wavenumber ratio of  $\gamma / \alpha = .67$  was reported. However, at slightly higher initial forcing amplitudes (.4%), a spanwise to streamwise wavenumber ratio of  $\gamma / \alpha = 1.46$  was identified, which cannot be explained with Craik's theory.

An explanation of this difference was later given by Herbert (1984). He studied the stability of the Blasius profile and a superimposed plane, time-periodic TS wave with respect to three-dimensional Squire modes. According to Herbert's calculation the growth of spanwise wave components can be explained by the fact that the phase velocities of the Squire modes (disturbance modes with zero normal disturbance amplitude) are independent of the spanwise wave angle. This growth of spanwise modes is an important feature of the boundary layer. The effective control of any three-dimensional waves in the boundary layer will have to address these important aspects.

However for important practical applications, such as flow over airplane wings, the instability mechanism that ultimately leads to transition to turbulent flow is essentially linear at first, before nonlinear interactions take over. In addition, for a disturbance background of small amplitudes this linear regime covers by far the largest distance in the entire transition process. Therefore the first control attempt of transition will have to concentrate on the early transition stages.

## 1.2 Linear Theory

In natural transition Tollmien Schlichting waves can be observed when the amplitudes of the background disturbances are very small. As long as the amplitudes of the disturbances in the boundary layer remain small one can study the stability of steady laminar boundary layers by decomposing the flow quantities as  $q = q_0(\underline{x}) + q'(\underline{x}, t)$ , where  $q_0$  is the base flow, and  $q'(\underline{x}, t)$  is a small disturbance quantity, the momentum equations can be linearized. The resulting equations can be further simplified by assuming a locally parallel flow, so that terms involving the mean normal velocity and streamwise derivatives of mean quantities can be omitted. Then, by using local velocity profiles, the stability of a boundary layer can be investigated (cf. Schlichting, 1982, p454 ff).

A solution ansatz in the form  $\phi(y) \cdot e^{i(\alpha x - \beta t)}$  leads, after some algebra, to the derivation of the Orr-Sommerfeld equation

$$(U-c)[\phi'' - \alpha^2 \phi] - U''\phi = \frac{-i}{\alpha \text{Re}_{\delta_1}} [\phi'''' - 2\alpha^2 \phi'' + \alpha^4 \phi], \quad (1.0)$$

where  $\alpha$ ,  $\beta$  are the complex wavenumber and the frequency, respectively, and  $\phi(y)$  is the complex streamfunction, which is a function only of the distance normal to the wall.

The nondimensional wavenumber  $\alpha$  and the Reynolds number  $\text{Re}_{\delta_1}$  are based on the displacement thickness, and the prime denotes differentiation with respect to  $y$ . This equation together with the boundary conditions

$$\phi = \phi' = 0 \quad ; \quad y = 0, \infty \quad (1.1)$$

forms an eigenvalue problem with the parameters  $\alpha$ ,  $c$ , and with the eigenfunction  $\phi(y)$ . For example, a real valued  $\beta$  and a complex  $\alpha = \alpha_r + i\alpha_i$  represents the spatial amplification case, where  $-\alpha_i > 0$  denotes spectrally amplified and  $-\alpha_i < 0$  spatially

damped waves. For each  $\alpha$  fixed, and  $U(y)$ ,  $U''(y)$  given from the Blasius solution, the eigenvalue  $c$  can be computed. A finite number of distinct eigenvalues exists, together with a continuous spectrum for which the eigenfunctions vary sinusoidally as  $y \rightarrow \infty$ . (Jordinson, 1971, and Grosch and Salwen, 1978). However the solution of the stability problem for the boundary layer yields only one discrete amplified mode for an unstable case. All the other discrete modes are damped.

The neutral stability curve, where  $\alpha_i = \beta_i = 0$ , for a zero pressure gradient boundary layer is shown in Figure 3. One can discern an upper and a lower branch of the neutral stability curve, which is divided by the point where the tangent to the curve is normal to the  $Re_{\delta_1}$ -axis. This point defines a critical Reynolds number  $Re_{crit}$ , because for lower  $Re_{\delta_1}$  no amplified oscillations can exist. This minimum  $Re_{crit}$  for the parallel flow assumption is approximately 520. Between the lower and upper branches of the neutral curve, the disturbances amplify exponentially, and outside of these branches the disturbances decay.

A great deal of theoretical and experimental effort has been expended on the study of single frequency disturbances. However, natural excitation by free stream disturbances produces modulated wave-trains or wave packets, which are observed to break down to turbulence in a much more dramatic manner than two-dimensional single frequency waves.

### 1.3 Wave Packets

Often natural transition from laminar to turbulent flows in a boundary layer is initiated by broad band, pulse-like disturbances or wave packets. Such wave packets can already be seen as modulated waves in the time traces at certain streamwise stations in the early experiments of Schubauer and Skramstad (1948). For such disturbances in the flat plate boundary layer, the amplified modes vary continuously with respect to one or more frequencies, and the most amplified mode is merely one among equals because the neighboring modes have relative growth rates and phase velocities close to the most amplified one. The amplified modes represent a group of waves, with their development being in time and space.

Gaster and Grant (1975), in an experiment on the development of isolated wave packets, kept the initial amplitudes of a localized wave packet small to study the linear evolution of the packet, and to avoid nonlinear distortion of the boundary layer in the early transition stages. Thus, the evolution of the packet is controlled by the amplification rate and the dispersion relation of constituent waves. The wave packet first followed the linear prediction manifested in the Gaussian envelope of the amplitudes. At locations further downstream, these envelopes became distorted, which may indicate a non-uniformity of the mean flow, or, the appearance of nonlinear interactions of the wave packet modes.

Gaster (1975) then applied a theoretical model based on the solution of the Orr-Sommerfeld equation. By a direct summation of the eigenfunctions, he tried to assemble the wave packet disturbances of the experiment. The initial conditions for the summation of the eigenfunctions were chosen to be close to that of the experiment. The agreement between experiment and theory was remarkably good, except for the development of a two peak phenomena (a distortion of the envelope) that

was observed in the experiment at locations further downstream from the excitation source.

In a direct numerical simulation with the complete Navier-Stokes equations, Fasel (1983) has calculated two-dimensional wave packets with an initially large amplitude input, to demonstrate that the distortions of the envelopes in the experiments of Gaster and Grant (1975) maybe attributed to nonlinear effects. These simulations showed a broadening of the amplitude spectrum due to wave interactions of the amplified modes in the wave packet.

Recently, Konzelmann (1991) simulated numerically the experiment of Gaster and Grant (1975) using the complete three-dimensional Navier-Stokes equations. The parameter of this computation closely matched those of the experiment and a remarkably good agreement between the numerical simulation and the experiment was found. These simulations provided strong evidence that the breakdown process was subharmonic. This, for example, would explain the appearance of the low frequency components for the oblique modes.

#### 1.4 Control

First attempts to control the laminar boundary layer concentrated on passive methods. There, the modification of the mean velocity profile, for example, using pressure gradients, wall suction, constant heating or cooling of the wall, alters the stability characteristics of the base flow. For the flat plate boundary layer in water, the effect of constant cooling is destabilizing, whereas the effect of a constant heating is stabilizing. Since the viscosity of water at ambient temperature decreases sharply with increase in temperature, heating yields a fuller velocity profile which, according to the linear stability theory, results in a more stable flow. In the water experiments of Strazisar et al. (1977), uniformly heating the boundary layer increased the

minimum critical Reynolds number and shifted the maximum amplification rates to lower frequencies. Strazisar et. al. tested several wall temperatures in their experiment and showed that the transition to turbulence could be delayed considerably.

Lowell (1974) , and Wazzan, Okamura and Smith (1968) extended the linear stability theory (see eqn. 1.0) to the non-isothermal case. They allowed for a variation of fluid viscosity with temperature, and Lowell also introduced an additional stability equation for the temperature. Both linear models predicted the disturbance behavior observed in the experiments only qualitatively.

In a numerical simulation, Bestek et al. (1987) used the full Navier-Stokes equations coupled with an energy equation and showed qualitatively good agreement to the experimental results of Strazisar (1968). Their numerical model allowed the study of a non-uniform as well as a uniform temperature distribution along the plate surface and showed the stabilizing as well as the destabilizing effect of heating and cooling, respectively, of the boundary layer in water.

Economic considerations limit the practical value of passive heating control. The large amount of heating necessary to reduce the fluid viscosity in water affects a technical operation economically because of increased operation and maintenance cost for the heating devices. Thus, more recently, the application of control of laminar flow has focussed on active methods. For this control approach the disturbance waves are directly attacked, their amplitude attenuated or enhanced (depending on the application), while the base flow stability characteristics are approximately unaltered. Thus, the amplification rates remain unchanged, but the disturbance waves begin to grow again from a much lower amplitude level. The basic principle of active control is the superposition of two disturbance waves. With proper phase and amplitude control between disturbance waves of the same frequency, reinforcement

or cancellation of the disturbance wave can be observed.

In experimental investigations several techniques were applied for an active control such as: heated wires (Corke, 1989), heater strips (Liepmann et al., 1982a,b), vibrating ribbons (Thomas 1983, Pupator and Saric 1989, and Milling 1981) and flexible walls (Wehrmann, 1965). For example, with the heater strips used in the experiments by Liepmann et. al., controlled TS waves could be produced. In these experiments it was shown that active control of Tollmien Schlichting waves in a water boundary layer with one activating and one controlling heater strip, led to a considerable increase of the transition Reynolds number in comparison with the uncontrolled case. Also Liepmann et al. were able to excite wave packets using the heater strip technique. However, their experiment exclusively addressed the control aspect of two-dimensional single frequency disturbances.

Active control of two-dimensional wave-trains was studied experimentally by Milling (1981), Thomas (1983), and Pupator and Saric (1989). In all experiments the disturbances were introduced with a vibrating ribbon and subsequently controlled by additional ribbons placed inside the boundary layer and downstream of the activator ribbon. Milling (1981) and Thomas (1983) concentrated on the control of single two-dimensional disturbances, and Pupator and Saric (1989) focussed on the control of random two-dimensional disturbances. In all experiments the amplitudes of the two-dimensional disturbances were considerably reduced, although a completely disturbance free environment could not be achieved. Eventually the three-dimensional disturbance background in the flow caused the breakdown to turbulent flow. With the low free stream turbulence wind tunnel of Pupator and Saric, the natural transition number of  $Re \approx 3.5 \cdot 10^6$ . With the control of the two-dimensional random disturbances the transition Re-number increased to  $5 \cdot 10^6$ . Apparently, the control of two-

dimensional disturbances appreciably increased the regime of laminar flow, yet for further improvement a two-dimensional control is not sufficient, because of the three-dimensional disturbance amplification.

Numerical studies on active transition control have also been performed by Laurien and Kleiser (1989) and McMurray et. al. (1983). They considered temporally growing TS waves only, and were limited in their investigation to a parallel base flow. In both investigations a wall normal disturbance component was applied on the entire plate surface. Using the wave superposition principle the disturbances were attenuated by adjusting the amplitudes and the phases. However, only partial attenuation of the two-dimensional wave was achieved and it was concluded that control would only be effective if applied at an early two-dimensional stage.

Recently three-dimensional spatially amplified disturbances in the flat plate boundary model were studied numerically by Fasel, Rist and Konzelmann (1987). Both two-dimensional and three-dimensional disturbances were introduced into an isothermal boundary layer by means of suction and blowing through a slot on the plate. The motivation for these simulations was to investigate the mechanisms of fundamental and subharmonic disturbance growth. Fasel et al. (1987) achieved remarkably good agreement with the experimental investigations of Klebanoff et al. (1962) for the fundamental case, and of Kachanov and Levchenko (1984) for the subharmonic case.

Kral (1988) extended the numerical approach of Fasel et. al (1987) to model disturbance excitations with the heater strip technique. Kral (1988) studied the cancellation of two- and three-dimensional spatially amplified disturbances on the flat plate boundary layer. However, only single frequency disturbances were considered and emphasis was placed on the control of the subharmonic and fundamental breakdown

processes. Also for passive control, the effect of uniform and non-uniform plate temperature on the growth rates of the disturbances was investigated. The passive control method effectively altered the growth rate of the two-dimensional mode which then delays the growth of the three-dimensional components.

### 1.5 Problem Statement

Active control of the laminar boundary layer with heater strips is investigated using numerical simulations based on the complete Navier-Stokes equations. From experimental observations it is evident, that disturbance waves in the boundary layer evolve spatially. Spatially propagating disturbance waves can be created with a controlled temperature variation over a heater strip as was demonstrated experimentally by Liepmann et. al. (1982a). Such temperature variations over a heater strip result in a local change of the fluid viscosity, and, when the temperature varies with time, produces a vorticity fluctuation on the wall surface and its immediate vicinity. In a boundary layer flow of water along a flat plate, a temperature variation of 20°C at ambient temperature creates a vorticity response, which corresponds to a typical disturbance present in a natural transition process.

The heater strip technique also has the advantage of not placing a physical obstruction in the flow field, unlike vibrating ribbons or heated wires placed away from the wall, inside the boundary layer. The heater strips are easily activated by an alternating current which produces temperature fluctuations of twice the current frequency.

For the present investigation a numerical method is used that is based on the vorticity-velocity formulation of the complete Navier-Stokes equations, coupled with the energy equation through a temperature dependent viscosity. The simulation are based on the so-called spatial model, thus allows for the spatial amplification of

disturbance waves in a laminar boundary layer. Finite difference approximations are used in streamwise and wall normal directions, and spectral approximations are used in spanwise direction for the three-dimensional simulations.

First, the propagation and amplification of two-dimensional wave packet disturbances are investigated, where the wave packets are created with the heater elements. From experiments we know that in natural transition a broad band of frequency components are amplified. Thus numerical simulations of wave packet disturbances, which also contain a broad band of frequency components are more relevant for investigating the control of natural transition.

A control strategy based on a numerically determined transfer function is introduced to achieve the attenuation of wave packet disturbances. The transfer function is based on the wall vorticity response of the boundary layer from a pulse temperature fluctuation over the heater strip. The applicability of the control strategy is first demonstrated for purely two-dimensional wave packet disturbances. Then the control strategy is extended for attenuating three-dimensional wave packet disturbances. The three-dimensional wave packet disturbance is assumed to be periodic in spanwise direction. Then the wave packet can be spectrally decomposed with respect to the spanwise wavenumbers, where each spanwise mode can be controlled separately.

For a practical application of the control of three-dimensional disturbance waves, the heater elements have to be divided into several spanwise segments, which can be controlled independently. Such arrays of spanwise heater elements have been successfully used in experiments by Robey (1986), to create single, oblique disturbance waves in the flat plate boundary layer, and by Nygaard (1991), to force three-dimensional disturbances in the boundary layer of a splitter plate, where the disturbances then propagated into a free shear layer. However, both experimental investi-

gations did not attempt the cancellation of disturbance waves.

In the present investigation three-dimensional control is also attempted, where spanwise wavenumber components are treated individually. Then for the control of the individual spanwise wavenumber components different control procedures can be investigated. For example, by attenuating only the dominant two-dimensional wave packet and leaving the spanwise modes uncontrolled, the effect on the three-dimensional components can be studied. Also the control of wave packet disturbances for the two- and three-dimensional wave components is attempted. The effectiveness of the control strategy, applied to each mode individually, is examined.

## 2. Governing Equations

The flow of a viscous fluid along a flat plate with nonuniform temperature is governed by the Navier-Stokes equations and the energy equation. In order to study the effect of a temperature field on the flow, the Navier-Stokes and energy equations must be coupled through temperature dependent fluid properties. The present investigations require the numerical solution of the governing equations for both two-dimensional and three-dimensional disturbance waves.

### 2.1 Equations for Two-dimensional Flow

It will be assumed that the flow is incompressible, the fluid is Newtonian, and that the specific heat capacity, the thermal conductivity and the density are independent of temperature. These assumptions are valid for water and many other liquids, as long as in the investigated control volume, large pressure and temperature differences can be avoided. However the change of viscosity with respect to temperature cannot be assumed constant for most fluids. For water at 20°C, a temperature increase of 25°C already gives rise to a 40% change in the kinematic viscosity. For the derivation of the Navier-Stokes equations it will be assumed, that the kinematic viscosity is a function of temperature. Since the temperature is expressed as a scalar field with spatial dimensions, the spatial viscosity gradients in the Navier-Stokes equations do not vanish.

The Navier-Stokes equations were derived with the nondimensional variables

$$\begin{aligned} x &= \frac{\bar{x}}{L}, & y &= \frac{\bar{y}}{L} \sqrt{\text{Re}}, & t &= \frac{\bar{t}}{L} U_\infty \\ u &= \frac{\bar{u}}{U_\infty}, & v &= \frac{\bar{v}}{U_\infty} \sqrt{\text{Re}}, & \omega &= \bar{\omega} \frac{L}{U_\infty \sqrt{\text{Re}}} \end{aligned}$$

$$\theta = \frac{T - T_\infty}{T_w - T_\infty}, \quad v = \frac{v}{v_\infty}, \quad p = \frac{\bar{p} - \bar{p}_\infty}{\rho U_\infty^2}, \quad (2.1)$$

where the  $x, y$  coordinates denote the streamwise and wall normal flow directions (Figure 2), respectively,  $u, v$  are the streamwise and wall normal velocity components,  $\omega$  the vorticity,  $\theta$  is the dimensionless temperature,  $\nu$  the kinematic viscosity,  $U_\infty$  is the free stream velocity,  $T_\infty$  is the free stream temperature,  $T_w$  is the wall temperature,  $L$  is a characteristic length, and  $v_\infty$  is the free stream viscosity. All quantities with a bar are dimensional.

Then the Navier-Stokes equations in dimensionless form can be derived with the above nondimensional variables as:

$$\begin{aligned} \frac{\partial u}{\partial t} + u \frac{\partial u}{\partial x} + v \frac{\partial u}{\partial y} = -\frac{\partial p}{\partial x} + \nu \left\{ \frac{1}{\text{Re}} \frac{\partial^2 u}{\partial x^2} + \frac{\partial^2 u}{\partial y^2} \right\} \\ + \frac{2}{\text{Re}} \frac{\partial v}{\partial x} \frac{\partial u}{\partial x} + \frac{\partial v}{\partial y} \left( \frac{\partial u}{\partial y} + \frac{1}{\text{Re}} \frac{\partial v}{\partial x} \right), \end{aligned} \quad (2.2a)$$

$$\begin{aligned} \frac{1}{\text{Re}} \left\{ \frac{\partial v}{\partial t} + u \frac{\partial v}{\partial x} + v \frac{\partial v}{\partial y} \right\} = -\frac{\partial p}{\partial y} + \frac{\nu}{\text{Re}} \left\{ \frac{1}{\text{Re}} \frac{\partial^2 v}{\partial x^2} + \frac{\partial^2 v}{\partial y^2} \right\} \\ + \frac{2}{\text{Re}} \frac{\partial v}{\partial y} \frac{\partial v}{\partial y} + \frac{1}{\text{Re}} \left\{ \frac{\partial v}{\partial x} \left( \frac{\partial u}{\partial y} + \frac{1}{\text{Re}} \frac{\partial v}{\partial x} \right) \right\}. \end{aligned} \quad (2.2b)$$

The viscosity in the above equations (2.2) is assumed to be a function of the temperature alone. Consequently, all the spatial derivatives which involve the viscosity could be replaced with the chain rule, i.e.  $\partial \nu / \partial x = (\partial \nu / \partial \theta) (\partial \theta / \partial x)$ . However for clarity in the derivation of the vorticity transport equation, the spatial viscosity derivatives are left in place.

By taking the curl of equation 2.2, the vorticity transport equation

$$\begin{aligned} \frac{\partial \omega}{\partial t} + \left( u - \frac{2}{Re} \frac{\partial v}{\partial x} \right) \frac{\partial \omega}{\partial x} + \left( v - 2 \frac{\partial u}{\partial y} \right) \frac{\partial \omega}{\partial y} - v \left( \frac{1}{Re} \frac{\partial^2 \omega}{\partial x^2} + \frac{\partial^2 \omega}{\partial y^2} \right) \\ - \frac{4}{Re} \frac{\partial u}{\partial x} \frac{\partial^2 v}{\partial x \partial y} + \left( 2 \frac{\partial u}{\partial y} - \omega \right) \left( \frac{1}{Re} \frac{\partial^2 v}{\partial x^2} - \frac{\partial^2 v}{\partial y^2} \right) = 0, \end{aligned} \quad (2.3)$$

can be derived, where the vorticity  $\omega$  is defined as

$$\omega = \frac{\partial u}{\partial y} - \frac{1}{Re} \frac{\partial v}{\partial x}. \quad (2.4)$$

To solve for the velocity components, two Poisson equations

$$\frac{1}{Re} \frac{\partial^2 u}{\partial x^2} + \frac{\partial^2 u}{\partial y^2} = \frac{\partial \omega}{\partial y}, \quad (2.5a)$$

$$\frac{1}{Re} \frac{\partial^2 v}{\partial x^2} + \frac{\partial^2 v}{\partial y^2} = -\frac{\partial \omega}{\partial x}, \quad (2.5b)$$

are used.

The energy equation, in nondimensional form with the temperature as the dependent variable, is

$$\frac{\partial \theta}{\partial t} + u \frac{\partial \theta}{\partial x} + v \frac{\partial \theta}{\partial y} - \frac{1}{Pr} \left( \frac{1}{Re} \frac{\partial^2 \theta}{\partial x^2} + \frac{\partial^2 \theta}{\partial y^2} \right) = 0. \quad (2.6)$$

The viscous dissipation term in the energy equation has been dropped, since the Eckert number,  $Ec = U_\infty^2 / (c T_\infty)$ , for incompressible flow at ambient temperature is very small.

In the above equations,  $Re = U_\infty L / \nu_\infty$  is the Reynolds number,  $Pr = \nu_\infty / \kappa_\infty$  is the Prandtl number, where  $\nu_\infty$  is the kinematic viscosity and  $\kappa_\infty$  the thermal diffusivity at free stream temperature.

For the kinematic viscosity an empirical relation of the form

$$\nu = \nu_\infty \exp \left[ \frac{T_a}{\theta \Delta T + T_\infty} - \frac{T_a}{T_b + T_a} \right] \quad (2.7)$$

is used, where  $T_a^*=506$  and  $T_b=-140$  are empirical constants estimated for water (Truckenbrodt, 1981), and  $\Delta T=T_w-T_\infty$  is the difference between the free stream temperature and a wall temperature.

### 2.1.1 Boundary Conditions

In this work, boundary conditions are employed that Fasel (1976) had successfully used for transition simulations for the flat plate boundary layer. Analogous conditions are applied for the energy equation. In the following discussion of the boundary conditions, the letters A to D refer to the four corners of the integration domain, which is shown schematically in Figure 2.

At the plate surface, A-B in Figure 2, of the integration domain, the conditions

$$\theta = \begin{cases} \theta_{wall}(x,t) & \text{if } x_1 \leq x \leq x_2 \\ 0 & \text{otherwise} \end{cases} \quad (2.8a)$$

$$u = 0 \quad , \quad v = 0 \quad (2.8b,c)$$

$$\frac{\partial \omega}{\partial x} = - \frac{\partial^2 v}{\partial y^2} \quad (2.8d)$$

are used, where the interval  $[x_1, x_2]$  is the streamwise extent of a heater strip. Thus, no slip and an impermeable wall is assumed. The relationship (2.8d) for calculating the wall vorticity was derived from 2.5b using the continuity equation together with the no slip condition.

Several choices of boundary conditions to model the heater strip are available. Following a theoretical analysis for thin-film heated elements, which can be used to measure the local wall shear stress, an approximation for the spatial temperature distribution of the heater strip can be found. Thin-film heaters are based on the Reynolds analogy of heat-transfer and skin friction. The heat supplied to the fluid is related to the local value of the skin friction, and can be found from the electrical

power supplied to the heated film. However, one part of the electrical power supplied to the heater is transferred to the substrate through heat losses. In a theoretical analysis of thin-film heating elements, Brown (1967) derived an expression relating the electrical power  $P$  input to a heated film and the wall shear stress by

$$\frac{P}{(T_w - T_\infty)} = M \tau_w^{1/3} + C \quad , \quad (2.9a)$$

with

$$M = kW \left[ \frac{\rho Pr}{1.9\mu^2} \right] L^{2/3} \quad , \quad (2.9b)$$

where  $k$  is the thermal conductivity,  $\rho$  is the fluid density,  $\mu$  is the dynamic viscosity,  $W$  and  $L$  are the spanwise width, and the streamwise length of thin-film, respectively, and  $C$  denotes conductive losses to the substrate.

In an experiment in a laminar boundary layer flow along a flat plate, Brown (1967) verified the relation (2.9) by calibrating a heated film on the plate surface. The film was controlled by a constant-temperature feedback bridge and values of  $P$  were recorded for several free stream velocities and wall shear stresses. The corresponding value of the skin friction is found from the theoretical solution of the zero-pressure gradient case. The experiments supported the validity of equation (2.9) by demonstrating a strong linearity between the electrical power input and the cubic root of the wall shear stress.

The derivation of equation (2.9) assumed a top-hat temperature distribution for the "physical" streamwise length of the heated film. In the presence of heat losses to the substrate it is unrealistic to assume a perfectly insulated film. However, Brown calculated the "effective" streamwise length of the heated film from the calibration curve by measuring the slope  $M$  and the spanwise width  $W$  and using equation (2.9b). For this procedure Brown determined the effective streamwise length of the

heated element to be twice the actual film length.

From the above analysis for thin-film heaters, the heater strip temperature at the plate surface in the interval  $[x_1, x_2]$  is approximated to

$$\theta_{wall}(x, t) = (1 + T_c(t)) \sin^2\left(\frac{\pi(x-x_1)}{x_2-x_1}\right), \quad (2.10)$$

where  $T_c(t)$  is a heater temperature disturbance signal.

For the computation of the steady state solution,  $T_c$  in (2.10) is set to zero. The special form of  $T_c$ , which introduces the wave packet disturbances in the flow field is discussed in the chapter for the numerical results.

At the inflow boundary, A-D in Figure 2, the similarity solution (Blasius solution) for the isothermal boundary layer is imposed.

$$u = u_{Blasius}, \quad v = v_{Blasius}, \quad \omega = \omega_{Blasius}, \quad \theta = 0. \quad (2.11)$$

The flow at the inflow boundary is assumed steady and isothermal. The wave packet disturbances are introduced so far downstream of the inflow boundary that no noticeable upstream effects of the disturbances are present near the inflow boundary.

At the top of the integration domain, C-D in Figure 2, the flow variables are separated to a steady and a transient part according to

$$u = U + u', \quad v = V + v', \quad (2.12)$$

$$\omega = \Omega + \omega', \quad \theta = \Theta + \theta',$$

where  $U, V, \Omega, \Theta$  are the steady components, and  $u', v', \omega'$  and  $\theta'$  denote the disturbance components. The following conditions are used:

$$U = 1, \quad \frac{\partial V}{\partial y} = 0 \quad (2.13)$$

$$\frac{\partial u'}{\partial y} = -\frac{\alpha}{\sqrt{Re}} u', \quad \frac{\partial v'}{\partial y} = -\frac{\alpha}{\sqrt{Re}} v'$$

$$\omega = 0 \quad , \quad \theta = 0 \quad .$$

A zero pressure gradient in streamwise direction is assumed, so that the streamwise base velocity remains constant at the upper boundary of the integration domain. The disturbance components are assumed to decay exponentially, where  $\alpha$  is a nondimensional wavenumber  $\alpha = \bar{\alpha} L$  of a most amplified frequency component of the wave packet.

At the outflow boundary, B-C in Figure 2, the conditions

$$\frac{\partial^2 U}{\partial x^2} = 0 \quad , \quad \frac{\partial^2 V}{\partial x^2} = 0 \quad , \quad (2.14a,b)$$

$$\frac{\partial^2 \Omega}{\partial x^2} = 0 \quad , \quad \frac{\partial^2 \Theta}{\partial x^2} = 0 \quad , \quad (2.14c,d)$$

$$\frac{\partial^2 u'}{\partial x^2} = -\alpha^2 u' \quad , \quad \frac{\partial^2 v'}{\partial x^2} = -\alpha^2 v' \quad , \quad (2.14e,f)$$

$$\frac{\partial^2 \omega'}{\partial x^2} = -\alpha^2 \omega' \quad , \quad \frac{\partial^2 \theta'}{\partial x^2} = -\alpha^2 \theta' \quad , \quad (2.14g,h)$$

are used. The conditions for the disturbance quantities allow a wave motion in the downstream direction, through the outflow boundary out of the integration domain. The wavenumber  $\alpha$  is selected from the maximum amplified disturbance component of the wave packet at the outflow boundary.

## 2.2 Equations for Three-Dimensional Flow

For the derivation of the vorticity transport equation, we start with the dimensional Navier-Stokes equations in cartesian coordinates

$$\rho \left\{ \frac{\partial \underline{u}}{\partial t} + (\underline{u} \cdot \nabla) \underline{u} \right\} = -\nabla p + \nu \nabla^2 \underline{u} + \nabla v \cdot \underline{\tau} \quad , \quad (2.15)$$

where  $\underline{\tau}$  is the rate of strain tensor

$$\underline{\tau} = \begin{bmatrix} 2 \frac{\partial u}{\partial x} & \frac{\partial u}{\partial y} + \frac{\partial v}{\partial x} & \frac{\partial u}{\partial z} + \frac{\partial w}{\partial x} \\ \frac{\partial u}{\partial y} + \frac{\partial v}{\partial x} & 2 \frac{\partial v}{\partial y} & \frac{\partial v}{\partial z} + \frac{\partial w}{\partial y} \\ \frac{\partial u}{\partial z} + \frac{\partial w}{\partial x} & \frac{\partial v}{\partial z} + \frac{\partial w}{\partial y} & 2 \frac{\partial w}{\partial z} \end{bmatrix}. \quad (2.16)$$

For the three-dimensional equations, the following set of nondimensional variables are introduced

$$x = \frac{\bar{x}}{L}, \quad y = \frac{\bar{y}}{L} \sqrt{\text{Re}}, \quad z = \frac{\bar{z}}{L}, \quad t = \frac{U_\infty}{L} \bar{t}, \quad (2.17)$$

$$u = \frac{\bar{u}}{U_\infty}, \quad v = \frac{\bar{v}}{U_\infty} \sqrt{\text{Re}}, \quad w = \frac{\bar{w}}{U_\infty},$$

$$\theta = \frac{T - T_\infty}{T_w - T_\infty}, \quad \nu = \frac{\bar{\nu}}{\nu_\infty}, \quad p = \frac{\bar{p} - \bar{p}_\infty}{\rho U_\infty^2},$$

$$\omega_x = \bar{\omega}_x \frac{L}{U_\infty \sqrt{\text{Re}}}, \quad \omega_y = \bar{\omega}_y \frac{L}{U_\infty}, \quad \omega_z = \bar{\omega}_z \frac{L}{U_\infty \sqrt{\text{Re}}}, \quad (2.17)$$

which are partially different from the two-dimensional set of the previous section. The vorticity field is defined as  $\underline{\omega} = -\nabla \times \underline{U}$ , and with the above nondimensionalization the vorticity components are

$$\omega_x = \frac{1}{\text{Re}} \frac{\partial v}{\partial z} - \frac{\partial w}{\partial y}, \quad (2.18a)$$

$$\omega_y = \frac{\partial w}{\partial x} - \frac{\partial u}{\partial z}, \quad (2.18b)$$

$$\omega_z = \frac{\partial u}{\partial y} - \frac{1}{\text{Re}} \frac{\partial v}{\partial x}. \quad (2.18c)$$

By taking the curl of the momentum equation (2.15) and exploiting the fact that for incompressible flows  $\nabla \cdot \underline{u} = 0$ ,  $\nabla \cdot \underline{\omega} = \nabla \cdot \nabla \times \underline{u} = 0$  and  $\nabla^2 \underline{u} = -\nabla \times \underline{\omega}$ , the vorticity transport equation for a fluid with temperature dependent viscosity is

$$\frac{\partial \underline{\omega}}{\partial t} - (\underline{\omega} \cdot \nabla) \underline{u} + (\underline{u} \cdot \nabla) \underline{\omega} = \nu \nabla_1^2 \underline{\omega} - \nabla_1 \nu \times (\nabla_1 \times \underline{\omega}) + \frac{1}{\text{Re}} \nabla_1 \times (\nabla \nu \cdot \underline{\tau}), \quad (2.19)$$

where  $\underline{\tau}$  is the nondimensional rate of strain tensor

$$\underline{\tau} = \begin{bmatrix} 2 \frac{\partial u}{\partial x} & \sqrt{\text{Re}} \frac{\partial u}{\partial y} + \frac{1}{\sqrt{\text{Re}}} \frac{\partial v}{\partial x} & \frac{\partial u}{\partial z} + \frac{\partial w}{\partial x} \\ \sqrt{\text{Re}} \frac{\partial u}{\partial y} + \frac{1}{\sqrt{\text{Re}}} \frac{\partial v}{\partial x} & \text{Re} 2 \frac{\partial v}{\partial y} & \frac{1}{\sqrt{\text{Re}}} \frac{\partial v}{\partial z} + \sqrt{\text{Re}} \frac{\partial w}{\partial y} \\ \frac{\partial u}{\partial z} + \frac{\partial w}{\partial x} & \frac{1}{\sqrt{\text{Re}}} \frac{\partial v}{\partial z} + \sqrt{\text{Re}} \frac{\partial w}{\partial y} & 2 \frac{\partial w}{\partial z} \end{bmatrix}. \quad (2.20)$$

The nondimensional operators  $\nabla_1$  and  $\nabla_1^2$  are defined as:

$$\nabla_1 = \frac{1}{\sqrt{\text{Re}}} \frac{\partial}{\partial x} \underline{i} + \frac{\partial}{\partial y} \underline{j} + \frac{1}{\sqrt{\text{Re}}} \frac{\partial}{\partial z} \underline{k}, \quad (2.21a)$$

$$\nabla_1^2 = \frac{1}{\text{Re}} \frac{\partial^2}{\partial x^2} + \frac{\partial^2}{\partial y^2} + \frac{1}{\text{Re}} \frac{\partial^2}{\partial z^2}. \quad (2.21b)$$

For the calculation of the velocity components  $u, v, w$  the three partial differential equations

$$\nabla_2^2 u = -\frac{\partial \omega_y}{\partial z} - \frac{\partial^2 v}{\partial x \partial y}, \quad (2.22a)$$

$$\nabla^2 v = \frac{\partial \omega_x}{\partial z} - \frac{\partial \omega_z}{\partial x}, \quad (2.22b)$$

$$\nabla_2^2 w = \frac{\partial \omega_y}{\partial x} - \frac{\partial^2 v}{\partial y \partial z}, \quad (2.22c)$$

are used, where  $\nabla_2^2$  is the two-dimensional Laplace operator defined by

$$\nabla_2^2 = \frac{\partial^2}{\partial x^2} + \frac{\partial^2}{\partial z^2}. \quad (2.23)$$

These Poisson type equations are derived using the vorticity equations (2.18) and the continuity equation  $\nabla \cdot \underline{u} = 0$ . This particular form with  $u$  and  $w$  treated differently from the  $v$  component is advantageous for the numerical method employed (Fasel et.

al. 1987). Using an implicit numerical scheme, the Poisson equations for the streamwise velocity component  $u$  and the spanwise component  $w$  can be solved directly.

Finally the thermal energy equation in nondimensional form is

$$\frac{\partial \theta}{\partial t} + \underline{u} \cdot \nabla \theta = \nabla_1^2 \theta, \quad (2.24)$$

where  $\theta$  is the nondimensional temperature, and the viscous dissipation has been dropped as in the two-dimensional equation, since the Eckert number is very small.

### 2.2.1 Boundary Conditions

The numerical simulations presented in this work are based on the assumption of a two-dimensional base flow subject to three-dimensional disturbances. These three-dimensional disturbances are assumed to be spanwise periodic. Then the boundary conditions for the steady flow are the same as the boundary conditions discussed in section (2.1.2).

At the plate surface, A-B in figure 2, the conditions

$$\theta = \begin{cases} \theta_{wall}(x,t) & \text{if } x_1 \leq x \leq x_2 \\ 0 & \text{otherwise} \end{cases} \quad (2.25a)$$

$$u = 0, \quad v = 0, \quad w = 0, \quad \omega_y = 0 \quad (2.25b)$$

$$\frac{\partial^2 \omega_x}{\partial x^2} = -\frac{\partial^2 \omega_y}{\partial x \partial y} + \frac{1}{Re} \frac{\partial}{\partial z} (\nabla^2 v), \quad (2.25c)$$

$$\frac{\partial \omega_z}{\partial x} = \frac{\partial \omega_x}{\partial z} - \frac{1}{Re} \nabla^2 v \quad (2.25d)$$

are used. At the plate surface two equations for the streamwise and the spanwise wall vorticity have to be solved. A discussion of the choice of conditions for the wall vorticity components can be found in Fasel et. al. (1987). The generation of three-dimensional waves in the boundary layer with heater strips is discussed in the next

chapter.

At the inflow boundary, A-D in Figure 2, the same conditions as for the purely two-dimensional flow are used. The three-dimensional disturbances are introduced in the flow field downstream of the inflow boundary using heater strips. Then all disturbance flow quantities are zero at the inflow boundary, and for the base flow quantities the similarity (Blasius) solution is used.

At the top of the integration domain, C-D in Figure 2, exponential decay for all disturbance components of the velocity is enforced similar to the two-dimensional case. Also the flow is assumed irrotational, so that all vorticity components vanish. The following conditions are used,

$$\frac{\partial u'}{\partial y} = -\frac{\alpha^*}{\sqrt{Re}} u' , \quad \frac{\partial v'}{\partial y} = -\frac{\alpha^*}{\sqrt{Re}} v' , \quad \frac{\partial w'}{\partial y} = -\frac{\alpha^*}{\sqrt{Re}} w' , \quad (2.26a,b,c)$$

$$\omega_x = 0 , \quad \omega_y = 0 \quad \omega_z = 0 , \quad \theta = 0 , \quad (2.26d,e,f,g)$$

where the prime quantities denote disturbance flow. The choice of  $\alpha^*$  will be discussed later in the context of the numerical method.

At the outflow boundary, B-C in Figure 2, the conditions for the disturbance components of the velocity and the vorticity are

$$\frac{\partial^2 u'}{\partial x^2} = 0 , \quad \frac{\partial^2 v'}{\partial x^2} = 0 , \quad (2.27a,b)$$

$$\frac{\partial^2 w'}{\partial x^2} = 0 , \quad \frac{\partial^2 \omega_x'}{\partial x^2} = 0 , \quad (2.27c,d)$$

$$\frac{\partial^2 \omega_y'}{\partial x^2} = 0 , \quad \frac{\partial^2 \omega_z'}{\partial x^2} = 0 , \quad (2.27e,f)$$

$$\frac{\partial^2 \theta'}{\partial x^2} = 0 . \quad (2.27g,h)$$

The outflow boundary conditions (2.27) are chosen so that no disturbance components reach the downstream boundary. A special numerical treatment, which will be discussed in the next chapter, ensures that no adverse effects are introduced through these conditions during the numerical integration.

### 3. Numerical Method

For the solution of the set of partial differential equations given in the previous chapter, two computer codes were developed, one for the solution of the two-dimensional problem, and one for the three-dimensional problem. For the numerical solution of the two-dimensional problem, a fully implicit finite-difference method of fourth-order accuracy in streamwise and wall normal direction and second order accuracy in time was developed. The basis for this was a numerical method developed by Fasel (1976) for the solution of the Navier-Stokes equations for the flat plate boundary layer, and the extension to fourth-order accuracy by Bestek (1980) for plane channel flow. The numerical method is based on the vorticity transport equation and two Poisson equations for the velocity components. Following their approach for the solution of the Navier-Stokes equations, the energy equation is incorporated in the numerical scheme. Also the additional viscosity derivative terms, which all vanish in the case of isothermal flow, have to be treated in the vorticity transport equation (2.3).

First a computer code for second order accuracy in streamwise and wall normal directions was developed based on the equations 2.3, 2.5 and 2.6, (Dittrich, 1985). For the extension to fourth-order accuracy, special attention had to be given to the spatial finite-difference approximations for the boundary points and for the grid points adjacent to the boundary.

For the three-dimensional computations, Kral (1988) developed a numerical method for non-isothermal boundary layer flows based on the method of Fasel et. al. (1987). This method uses a spectral decomposition method in spanwise direction, which is based on the set of equations introduced in chapter 2.2.

### 3.1 Calculation of Two-Dimensional Flows

For the discretization of the equations (2.3), (2.5) and (2.6) the rectangular integration domain is divided into finite intervals of length  $\Delta x$ ,  $\Delta y$  (Figure 2), and the time coordinate is discretized using the interval  $\Delta t$ . The coordinates of the grid points in the streamwise ( $x$ ), wall normal ( $y$ ) and the time ( $t$ ) directions are specified by the integers

$$\begin{aligned} x &= n \Delta x , & 0 \leq n \leq N , \\ y &= m \Delta y , & 0 \leq m \leq M , \\ t &= p \Delta t , & p = 0,1,2 \dots \end{aligned}$$

The left boundary of the integration domain is at the distance  $x_0$ , measured from the leading edge of the plate. The distance  $x_0$  is chosen so that the inflow boundary is at a position, where the disturbance waves, according to linear stability theory, pass into a region of amplification. A list of the finite-difference approximations used in the numerical method is given in Appendix B for the energy equation. The finite-difference approximations for the Navier-Stokes equations and the Poisson equations for fourth-order accuracy in streamwise and wall normal direction can be found in Bestek (1980).

The discretized equations are solved using a line iteration method with overrelaxation. At each line the vorticity transport and the Poisson equation for the wall normal velocity component are solved simultaneously. Then the Poisson equation for the streamwise velocity component and the energy equation is solved. The base flow is calculated first using a starting solution as obtained from the similarity solution of the unheated boundary layer, with  $T_c$  for the heater temperature of the boundary condition (2.10) set to zero. The nonlinear terms are upgraded at each iteration level and the iteration for the base flow solution is repeated until the difference of two consecutive iterations for all the flow variables reach the threshold  $\epsilon < 10^{-8}$ .

After the base flow has been calculated for a certain heater strip configuration, a temperature disturbance is introduced into the flow field through the boundary condition at the wall modeling the heater strips. At each time step, the integration of the discretized equations is similar to that for obtaining the steady solution. However, now at each time step the iteration continues until the threshold of  $\epsilon < 10^{-5}$  for the all flow variables is reached.

For the wave packet simulations the number of time steps to be computed is determined by the speed of propagation of the wave packet disturbances. The maximum number of time steps is chosen so that at in the computational domain the last x station of interest, the disturbances have completely passed that position.

### 3.2 Calculation of Three-Dimensional Flows

For the three-dimensional computations a spanwise periodicity of the disturbance components is assumed. Then the three-dimensional equations can be spectrally decomposed in spanwise direction by a Fourier series

$$f(x, y, z, t) = \sum_{k=-K}^{k=+K} F_k(x, y, t) e^{ik\gamma z}, \quad (3.1)$$

where  $f(x, y, z, t)$  represent all the dependent variables in the physical domain,  $F_k(x, y, t)$  are the complex spectral components and  $\gamma$  is the spanwise wavenumber.

With the above Fourier approximation the vorticity transport equation, the energy equation and the Poisson equations for the velocity components are transformed. Then all derivatives with respect to the spanwise direction are replaced by

$$\frac{\partial f(x, y, z, t)}{\partial z} = i\gamma k \sum_{k=-K}^{k=+K} F_k(x, y, t) e^{ik\gamma z}, \quad (3.2a)$$

$$\frac{\partial^2 f(x, y, z, t)}{\partial z^2} = -\gamma^2 k^2 \sum_{k=-K}^{k=+K} F_k(x, y, t) e^{ik\gamma z}. \quad (3.2b)$$

The nonlinear terms in the vorticity transport equations require a special attention. For a series truncation with a large number  $K$  each quadratic term in the equations would require an expansion proportional to  $K^2$  terms to fully account for the nonlinear interaction. Our computations shall be restricted to the study of the initial three-dimensional stages where only a small number of nonlinear interactions are relevant and therefore  $K$  can be kept small. The nonlinear terms are calculated with a purely spectral method.

Substitution of the series representation (3.1) into equations (2.19), (2.22) and (2.24) yields a new set of equations of the form

$$\frac{\partial \Omega_{xk}}{\partial t} = \underline{A}_{xk} + \underline{B}_{xk} + \underline{C}_{xk} , \quad (3.3a)$$

$$\frac{\partial \Omega_{yk}}{\partial t} = \underline{A}_{yk} + \underline{B}_{yk} + \underline{C}_{yk} , \quad (3.3b)$$

$$\frac{\partial \Omega_{zk}}{\partial t} = \underline{A}_{zk} + \underline{B}_{zk} + \underline{C}_{zk} , \quad (3.3c)$$

$$\frac{\partial^2 U_k}{\partial x^2} - \gamma^2 k^2 U_k = -i\gamma k \Omega_{yk} - \frac{\partial^2 V_k}{\partial x \partial y} , \quad (3.3d)$$

$$\nabla^2 V = i\gamma k \Omega_{zk} - \frac{\partial \Omega_{zk}}{\partial x} , \quad (3.3e)$$

$$\frac{\partial^2 W_k}{\partial x^2} - \gamma^2 k^2 W_k = -i\gamma k \frac{\partial V_k}{\partial y} + \frac{\partial \Omega_{yk}}{\partial x} , \quad (3.3f)$$

$$\frac{\partial \Theta_{zk}}{\partial t} + D_k = \frac{1}{Pr} \nabla^2 \Theta_k , \quad (3.3g)$$

and

$$\nabla^2 = \frac{1}{Re} \frac{\partial^2}{\partial x^2} + \frac{\partial^2}{\partial y^2} - \frac{\gamma^2 k^2}{Re} .$$

In the equations above all variables are spectral coefficients as defined in (3.1). The

term  $\underline{A}_k$  is a sum of all the nonlinear terms of the vorticity transport equation,  $\underline{B}_k$  accounts for the diffusion term which is multiplied by the viscosity coefficients, and  $\underline{C}_k$  combines all the additional viscosity derivative terms in the vorticity equation. The term  $D_k$  in the energy equation includes all the convective terms. With this spectral approximation (3.1), the  $\alpha^*$  required in the boundary conditions for the free-stream boundary conditions (2.26) is  $\alpha^* = (\alpha^2 + (k\gamma)^2)^{1/2}$ . A complete list of the terms  $\underline{A}_k, \underline{B}_k, \underline{C}_k$  and  $D_k$  can be found in Kral (1988).

The three-dimensional temperature disturbances  $\Theta'$  are assumed to be symmetric with respect to the  $z=0$  axis. Then the disturbance variables  $U', V', \Omega'_z$  are also symmetric to the  $z=0$  axis in the spanwise direction. Since all variables  $f(x, y, z, t)$  in (3.1) are real, then the  $U', V', \Omega'_z$  are purely real, while  $\Omega'_x, \Omega'_y$  and  $W$  are purely imaginary. For the complete solution of the system of equations (3.3) it is therefore only necessary to compute the spectral coefficients from  $k=0$  to  $k=K$ , since for a real valued function  $f$ , the spectral coefficients follow the relation  $F_{-k} = F_k^*$ , where the asterisk denotes the complex conjugate.

Once the equations are spectrally decomposed in the spanwise direction, the implicit solution is analogous to that for the two-dimensional flow which was discussed previously. However, for the three-dimensional calculations, at each grid line, during the  $x$ -direction sweep,  $K$  equations (3.3) have to be solved for each spanwise coefficient, before the procedure can advance to the next grid line. Thus, for the three-dimensional calculations the solution has to completely solve for a  $N \times M \times (K+1)$  grid, before proceeding to the next iteration level.

For the control of three-dimensional disturbances, the boundary conditions modeling the heater strips have to incorporate the spanwise variation. For the present investigations the boundary conditions for the wall temperature (2.25a) are

$$\theta_{wall, k=0} = (1 + A_{2D} T_c) \sin^2 \left[ \frac{\pi(x-x_1)}{x_2-x_1} \right], \quad (3.4a)$$

$$\theta_{wall, k=1} = A_{3D} T_c \sin^2 \left[ \frac{\pi(x-x_1)}{x_2-x_1} \right], \quad (3.4b)$$

where the heater strip location is in the interval  $[x_1, x_2]$ , and  $A_{2D}$  and  $A_{3D}$  are the amplitudes of the two- and three-dimensional disturbances, respectively. For the evaluation of a control strategy to attenuate three-dimensional wave packet disturbances, a flow perturbation was triggered using only one spanwise mode. Thus for such a control strategy to be practical one would have to assume that dominant three-dimensional modes are present in the flow field. Experimental investigations have shown that at initial three-dimensional stages of transition, preferred spanwise modes are indeed present. However, for a more advanced flow control strategy, applicable to later stages of the transition process, several spanwise modes would be required.

The outflow condition at the boundary B-C in Figure 2 poses a special problem in the computation, since it is actually not a physical boundary. In order to avoid that disturbance components reach the outflow boundary and become reflected, a similar numerical procedure was applied as discussed in Kloker, Konzelmann and Fasel (1991). At each iteration level a tapering function is imposed for the spanwise disturbance vorticity  $\omega_z$ , so that in the last 10% of the integration domain, the spanwise disturbance vorticity is forced to zero. The tapering function used for this process, is

$$\omega'_{z k} = \omega'_{z k} (1 - 10x^3 + 15x^4 - 6x^5). \quad (3.5)$$

With this condition imposed, also all the other disturbance variables are diminished within the last 10% of the integration domain. Several tests for this boundary condi-

tion have been performed. It was confirmed, that the upstream effect of this tapering function remains confined to the last 10% of the integration domain, as required.

## 4. Results

### 4.1 Computation of Two-Dimensional Flows

The first part of the numerical results considers a two-dimensional base flow with two-dimensional disturbances. In this case the set of equations is reduced to a scalar vorticity transport equation for the spanwise vorticity  $\omega_z$ .

For the two-dimensional computations, the following parameters have been used:

$$\begin{array}{lll}
 Re = 100000 , & L = .05 \text{ m} , & x_0 = 1.2169 , \\
 Re_{\beta_1}(\text{at } x_0) = 600 , & \Delta x = 8.267 \times 10^{-3} , & \Delta y = 2.1345 \times 10^{-1} , \\
 \Delta t = 1.122 \times 10^{-2} , & \alpha = 38 , & T_w = 30^{\circ}C , \\
 Re_{\beta_1}(\text{at } x_N) = 920 , & T_{\infty} = 20^{\circ}C , & Pr = 7 \\
 & Y/\Delta y = 80 , & X/\Delta x = 200 .
 \end{array}$$

Figure 3 shows the location of the integration domain in the linear stability diagram frequency parameter  $F$  versus  $Re_{\beta_1}$ . The nondimensional frequency parameter  $F$  is defined as

$$F = \frac{\bar{\beta} v_{\infty}}{U_{\infty}^2} 10^4, \quad (4.1)$$

where  $\bar{\beta}$  is the dimensional angular frequency. However, the frequency of the Navier-Stokes simulations is nondimensionalized by

$$\beta = \bar{\beta} \frac{L}{U_{\infty}} . \quad (4.2)$$

Then, the relation between these two frequencies is given by

$$\beta = \frac{Re}{10^4} F , \quad (4.3)$$

where  $Re$  is the Reynolds number based on a characteristic length  $L$ .

Based on wavenumber of the most unstable frequency of a wave packet disturbance for the  $Re_{\delta_1}$  range, covered in this computation, the streamwise stepsize  $\Delta x$  was calculated from

$$\Delta x = \frac{2 \pi}{\alpha N_{wave}} , \quad (4.4)$$

with  $N_{wave} = 20$  for sufficient streamwise resolution of the disturbance components. Therefore, the integration domain spans approximately ten wavelengths in the streamwise direction. The height of the integration domain  $Y$  was calculated from the displacement thickness at the inflow boundary so that  $Y = 9 \delta_1$ .

For all simulations, two heater strips were used on the plate surface. The first heater strip is strictly used to create the initial wave packet disturbances. The second heater strip, placed further downstream on the flat plate, is used to control the disturbances. For the control aspects discussed in this work, the creation of the initial wave packet in the flow field could have also been achieved by other methods, (for example suction-blowing through wall slots). However, aspects of the initial creation of wave packet disturbances with heaters could also have an effect on the control implementation.

#### 4.1.1 Wave Packet Disturbances

In a first attempt to create wave packet disturbances, the first heater strip was activated by

$$\theta_{wall} = T_c(t) \sin^2 \left( \frac{\pi(x-x_1)}{x_2-x_1} \right) \quad x_1 \leq x \leq x_2 ,$$

$$T_c = \begin{cases} \sin\left(\frac{\pi t}{TP}\right) & 0 \leq t \leq TP \\ 0 & t > TP \end{cases} , \quad (4.5)$$

where  $TP$  is the duration of the temperature forcing of the heater strip.

Figure 4 shows the vorticity disturbance signal at the wall over the whole integration domain at several time steps after the forcing is completed. The heater strip is located between  $20 \leq x/\Delta x \leq 30$ . A wave packet disturbance can be identified, which travels in streamwise direction. Furthermore, besides this Tollmien Schlichting wave mechanism, a second effect is clearly identifiable. A strong vorticity defect at an early time in the vicinity of the heater strip indicates a local departure from the initially isothermal mean flow. The forcing signal (4.5) introduces a local heat spot, which is due to the unsteady heating. This heat spot convects slowly in downstream direction, and diffuses in the wall normal direction. Eventually, the spot disappears, and the isothermal condition reappears over the heater strip.

For the prospective control, the effect of this unsteady heating phenomena is disadvantageous for two reasons. First, the local non-stationarity appears in the vorticity signal as a very low frequency band which would have to be filtered out by a high pass filter to identify the proper TS mechanism. Second, the unsteady heating can locally affect the stability characteristics of the mean flow.

To minimize the effect of such an unsteady component the heater strips are operated over a steady temperature component. Then, a temporal disturbance component is superimposed so that the total mean heat input is minimized. The heating procedure for the heater strips is therefore modified to incorporate a steady heater temperature by using

$$\theta_{wall}(x,t) = (1+T_c(t)) \sin^2\left(\frac{\pi(x-x_1)}{x_2-x_1}\right), \quad (4.6)$$

in the interval  $(x_1 \leq x \leq x_2)$ .

The forcing temperature  $T_c(t)$  is taken to be

$$T_c(t) = \begin{cases} 24t^5 - 45t^4 + 20t^3 & \text{if } 0 \leq t \leq TP/2 \\ 24(2-t)^5 - 45(2-t)^4 + 20(2-t)^3 & \text{if } TP/2 \leq t \leq TP \\ 0 & \text{if } t \geq TP \end{cases} \quad (4.7)$$

The modulus of the forcing temperature versus  $F$  is shown on the left hand side of Figure 3. This particular choice ensures that the spectrum has a broad amplitude distribution over the range of typical frequencies of the boundary layer and was derived so that

$$\int_0^{TP} T_c(t) dt = 0 \quad (4.8)$$

The effect of a steady temperature distribution on the steady flow profiles for two heater strips is shown in Figure 5. A thermal wake behind the two heater strips now appears and reaches far downstream. The thermal wake lies within the boundary layer since for  $Pr=7$  the ratio of the thermal to the fluid boundary layer is approximately one half. However, the magnitude of the temperature in the thermal wake is small compared to the temperature at the heater strip. Therefore, the isothermal contours in Figure 5 are chosen at a lower temperature range to visualize the small thermal wake. The temperature gradients at stations further downstream, although noticeable, are small. The line contours in Figure 5 denote the constant streamwise velocity. Over the heater strip a slight indentation of the streamwise velocity is apparent, however, the change of the velocity profiles downstream of the heater strips is very small.

Results of a computation with the revised heating procedure (4.7) are shown in Figure 6. The heater strip location is between  $30 \leq x/\Delta x \leq 40$ . The wave packet disturbance propagates in the downstream direction, and the local effect of the unsteady heating is greatly reduced. Only at time  $t/\Delta t = 80$  can a small non-stationary heat spot be identified.

A more comprehensive look at the evolution of the wave packet disturbance is given in Figure 7. The disturbance components are plotted in perspective representation for five time instances,  $t/\Delta t=40, 80, 120, 160, 200$ , (the forcing ended at  $t/\Delta t=40$ ). The streamwise disturbance velocity component  $u'$ , at approximately  $y/\delta = 0.4$  ( $\delta$  is the local boundary layer thickness), shows the typical group of disturbance extrema in the vicinity of the wall, and a smaller, second group of disturbance extrema further out, where  $y/\delta \approx 1.2$ . The wall normal velocity component  $v'$  in comparison has only one group of disturbance extrema. The vorticity disturbance shows two groups of disturbance extrema, with the larger one at the wall surface. At the time  $t/\Delta t = 40$ , for the  $u'$  velocity and for the vorticity signal  $\omega'_z$  a spike close to the heater strip is visible. At the same time, the disturbance temperature  $\theta'$  shows two temperature spikes, which are then strongly reduced and eventually disappear over the next four time levels. Then the temperature wave packet emerges at a very low amplitude level which propagates in streamwise direction.

With the revised temperature forcing procedure, a slight deviation from a stationary base flow is still present. However, the TS wave mechanism dominates immediately after the end of the forcing.

From a complete simulation one can analyze the wave packet disturbances by decomposing the signals using a fast Fourier transform (FFT). The details of using such a FFT on non-periodic signals are explained in Appendix A.

For example, the wall vorticity disturbance signal from the computed data at several streamwise positions were Fourier analyzed. Figure 8 shows the amplitude- and phase-spectra of the wall vorticity when only the first heater was activated. The amplitude- and phase-spectra were computed at several streamwise positions  $x/\Delta x = 50, 80, 110, 140, 170$ . In the lower frequency range, for  $F \leq .8$ , and for frequencies

above  $F = 2.0$ , each individual frequency component becomes damped, since the magnitude of their amplitudes for increasing streamwise positions are reduced. In the intermediate frequency region ( $.8 \leq F \leq 2.0$ ) the amplitudes of the frequency components of the wave packet disturbance increase. The most amplified frequency component shifts to lower frequencies from  $F = 2.0$  at  $x/\Delta x = 50$  to  $F = 1.4$  at  $x/\Delta x = 170$ , and the band of amplified frequency components narrows considerably. The phase-spectrum confirms the convective instability mechanism through the rapid change in phases of the frequency components for increasing streamwise distance from the heater strip. At a wall normal distance of  $y/\Delta y = 20$  ( $y/\delta = 1.2$ ), the amplitude- and phase-spectra from analyzing the wall normal velocity component is shown in Figure 9. The amplitude- and phase-spectra, which are analyzed at a wall normal distance outside the boundary layer  $y/\Delta y = 20$ , agree with the results of the wall vorticity analysis.

In Figures 8 and 9, no single point of neutral stability of the frequency components can be identified. Instead, several points of neutral amplification exist, which can be defined by the intersection of the amplitude spectra for two consecutive streamwise positions. These neutral amplification points are shifted to lower frequency components for increasing downstream positions. The non-parallel boundary layer continuously alters its stability characteristics as can be seen from the streamwise dependence of the maximum amplification rate, and from the streamwise dependence of the neutral points of the frequency components in the spectra.

From the phase-spectrum  $\phi$  one can extract information on the dispersive nature of the wave packet evolution. The wavenumber  $\alpha$  of each frequency component can be found by

$$\alpha = - \frac{\partial \phi}{\partial x} \quad (4.9)$$

The phase velocities then follow from

$$c_{phase} = \frac{\beta}{\alpha} . \quad (4.10)$$

The computed dispersion relation  $\alpha = \alpha(\beta)$  of the wall vorticity signal at the position  $x/\Delta x = 140$ ,  $Re_{\delta_1} = 835$  is shown in Figure 10. The range of the curve is limited by the band of detectable frequencies in the wave packet spectrum. For the range of frequencies that constitute the wave packet disturbance, the dispersion relation is not exactly a straight line. However, the departure from a straight line is small.

In Figure 11, a comparison is made of the phase velocities and the amplification rates obtained from the Navier-Stokes computations at a position  $x/\Delta x = 140$  with those of the linear stability theory. The amplification rate  $\alpha_i$ , which denotes the imaginary part of the complex wavenumber, is calculated from

$$\alpha_i = \frac{\partial}{\partial x} \ln A , \quad (4.11)$$

where  $A$  are the amplitudes of the frequency components. The phase velocities and the amplification rates in Figure 11 were determined by analyzing the wall vorticity signal of the Navier-Stokes equations. For the range of frequencies present in the wave packet, the phase velocities of the linear theory and of the computations agree very well. The rate of amplification in Figure 11b are identical for almost all frequency components, which can be detected in the wave packet. However, at the maximum rate of amplification of the linear theory is slightly under the value found from the Navier-Stokes computation.

In Figures 12 and 13, a comparison of the amplification rates of the Navier-Stokes computation at the location of the second maximum of the vorticity and of the maximum of the wall normal velocity with the linear theory is presented. The

amplification rates of the wall normal velocity component exceeds the linear theory slightly, and also lie above the prediction from the wall vorticity analysis. However, the Navier-Stokes solution of the vorticity at the second maximum shows a strong underprediction of the amplification rates compared to the linear stability theory.

For all flow quantities that were analyzed at three different locations in the flow field, the phase velocities are in very good agreement with the linear theory (Figures 11a, 12a, 13a). However, the rate of amplification can vary considerably depending on the criteria used.

The amplification rates of the linear spatial theory have been calculated with the Orr-Sommerfeld equation (1.0) using the computed Navier-Stokes velocity profile as the base flow. This profile includes the small deviation from the unheated Blasius profile because of the presence of the thermal wake. Although this effect at first seemed negligible, it causes a difference of almost 15% in the amplification rates of the most amplified components.

The predicament is choosing the proper flow component at a certain location with which to compare the amplification rates with linear stability theory. An additional source of disparity between these results is the assumption of a locally parallel base flow in the linear theory. Nonparallel effects are strongest close to the wall, and the growth rates strongly depend on the criteria used (Fasel and Konzelmann, 1990). As for the computation of wave packet disturbances with a broad band of frequencies, the analysis of the amplification rates show the same trend as the findings of Fasel and Konzelmann.

#### 4.1.2 Passive Heated Segments

The comparison of the computed wave packet disturbances with the linear stability theory showed a significant deviation in the amplification rates when the

Blasius profile instead of the Navier-Stokes profile was used in the linear stability calculations. This effect can be attributed to the thermal wake downstream of the heater strip.

To further investigate the effect of passive heating segments on the stability of wave packet disturbances, a heated segment was used as a boundary condition as shown in Figure 14. The wall temperature distribution is shown on the lower part of Figure 14a, where the heated segment starts at  $x/\Delta x = 70$  and continues to the end of the integration domain. From the Fourier analysis of the wave packet signal of the wall vorticity, several frequency components were chosen and their normalized streamwise amplification was plotted (Figure 14a).

For the computation with the heated segment, all the frequency components are damped as soon as they have passed the temperature ramp (Figure 14a). This agrees favorably with the passive control computations of Bestek et. al (1987). Heating of the boundary layer in water stabilizes the flow since the viscosity is reduced and the velocity profiles become fuller. However, during the passage of the temperature ramp, where  $d\theta/dx|_{wall} > 0$ , the frequency components from analyzing the wall vorticity shoot up to a higher level. Then they all become damped shortly behind the temperature ramp, where  $d\theta/dx|_{wall} = 0$ .

In Figure 14b a similar computation has been repeated, however without the heated segment. In this case, three frequency regions of amplification of wave components can be identified. First, the lower frequency range consists of modes whose amplitudes initially decrease in streamwise direction until a minimum is reached, from which point on the modes are amplified (see e.g.  $F=.93$ ). These frequencies pass through the lower branch of the neutral stability loop. At higher frequencies, certain modes are first amplified as they propagate downstream, and then become damped

(see e.g.  $F=1.89$ ), which means that they passed through the upper branch of the neutral loop. Frequency components smaller than  $F=.55$  are damped over the entire computational domain, but their damping rate is progressively reduced in streamwise direction.

To further study the effect of the temperature ramp, a simulation with a passive heater strip was investigated. Figure 15 shows a comparison of the streamwise amplification of four frequency components from the wave packet disturbance with and without a passive heater strip. The heater strip is between  $70 \leq x/\Delta x \leq 90$ . The frequency components from the wall vorticity (Figure 15 a) show the selective amplification as described above. Furthermore, over the first half of the passive heater strip, the amplitude of each frequency component increases approximately by 10%. Then, in the second part, the amplitude of each frequency component drops below the value of the unheated case.

A comparison of the same frequency components by analyzing the wall normal velocity component away from the wall ( $y/\Delta y = 10$ , Figure 15b) does not show the local frequency "hump" of the wall vorticity. However, both analyses show a stabilizing trend downstream of the heater strip that continues until the end of the integration domain. It appears that the additional heating from the passive heater strip reinforces the thermal wake. The effect of this reinforcement reduces the rate of amplification of the most amplified mode by approximately 27% (Figure 16). The distance where the wall vorticity signal was recorded for the computation of the amplification rate is two and a half heater lengths downstream of the passive heater. As seen in Figure 16, the dome-shaped amplification curve for all frequency components at the position  $x/\Delta x = 140$  is within the one computed without the passive heater. The additional passive heater therefore leads to an overall less unstable boun-

dary layer due to the thermal wake.

Figure 17 shows the streamwise velocity profile of the base flow and the base flow vorticity at a position  $x/\Delta x=100$  close to the passive heater strip. Also shown in this figure are the differences of the quantities between the case with the passive heater and the case without the passive heater. A fuller velocity profile throughout the boundary layer can be observed for the heated case. However, the differences in the velocity profiles are very small. Also, an inflection point in the streamwise velocity in the vicinity of the wall can be identified, where  $\partial\omega/\partial y = 0$ . This inflection point can only be attributed to the thermal wake, which makes the fluid hotter within a region inside the boundary layer. Since the momentum and energy equations are coupled, the viscosity in the thermal wake is reduced, which contributes to a fuller velocity profile.

In Figure 18, the steady streamwise pressure gradient at the wall surface for two passive heater strips is presented. The pressure gradient at  $y = 0$  is calculated from

$$\frac{dp}{dx} = \nu \frac{d^2u}{dy^2} - \left(\frac{d\nu}{d\theta}\right)\left(\frac{d\theta}{dy}\right)\left(\frac{du}{dy}\right). \quad (4.12)$$

In the absence of the heaters, the pressure gradient  $dp/dx$  vanishes, since no external pressure gradient is imposed on the flow field. In the vicinity of the heater however, the sudden temperature rise leads to a negative  $d\theta/dy$  locally, so that the wall pressure rises. Note that  $d\nu/d\theta$  for a small temperature difference is approximately a negative constant. In the second half of the heater, the sudden drop in temperature then leads to a region of higher fluid temperature near the wall, and the temperature gradient  $d\theta/dy$  changes its sign.

For the local analysis of the wall vorticity signal, the "hump" in the frequency components in Figure 15 could be explained by the local rise and drop of the pres-

sure gradient. In the first half a positive, adverse wall pressure gradient leads to the strong growth of the frequency components, and in the second half the stronger negative, favorable pressure gradient reduces the amplitudes of the frequency components to a level, which is lower compared to the unheated case. Away from the wall heater, for positions downstream of the heater strip, this effect is diminished. However, the growth rates of the frequency components downstream of the heater strip are slightly reduced, as previously explained in connection with Figure 16, since the thermal wake changes the velocity profiles of the base flow through the temperature dependence of the kinematic viscosity.

#### 4.1.3 Transfer Function Concept

Boundary layer transition is a very complex phenomenon and many aspects are not yet understood. However, in the early stage of the transition, where small disturbance waves become amplified, nonlinear effects can be considered small. Although the mechanism by which the heater strip creates disturbances in the boundary layer may be nonlinear, the amplitudes of the heat input were such that the amplitudes of the disturbance response were very small initially, so that the amplification process can be considered linear. Here a relationship between an input disturbance (the heater temperature), and an output fluctuation (the wall vorticity) is sought. The transfer function  $H(F)$ , which is defined through the input-output relationship, can be found from

$$H(F) = \frac{\hat{O}_{x_1}(F)}{\hat{I}_{x_0}(F)} \quad (4.13)$$

where  $\hat{O}_{x_1}(F)$  and  $\hat{I}_{x_0}(F)$  are the complex amplitudes of the wall vorticity signal and the temperature input, respectively. Once the transfer function is determined, it can be used to predict the linear response of the boundary layer flow to any heat input

fluctuation.

Figure 19 shows a schematic representation of the transfer function technique applied between two stations  $x_1$  and  $x_0$ . On the left side of the Figure 19, the input temperature signal from the heater strip is shown together with the modulus of its transform. The input temperature signal is superimposed at the center location of the heater strip at  $x_0$  according to (2.8). The right hand side of Figure 19 shows schematically the vorticity response and the modulus of its transform at the station  $x_1$ . The numerical approximation of this transfer function assumes a relatively flat input spectrum over all the relevant boundary layer modes. A discussion of the definition and validity of the transfer function is given in Appendix A.

Figure 20 shows the modulus of the transfer function for three different heater strip widths. The three widths are chosen relative to the wavelength of the most amplified mode of the wave packet in the region of the heaters. The heater lengths  $N = 10, 20, 30$  correspond to approximately  $1/2, 1$  and  $1 \frac{1}{2}$  wavelengths of the most amplified frequency component. In all three cases, the same input temperature disturbance was used, and the response signal was recorded at the same position  $x/\Delta x = 70$ . The strongest vorticity response was found for  $N=10$ . The heater strip with  $N=30$  shows a trough in the region of  $F=1.9$ . Close to this frequency component, the phases were undergoing a shift of  $\pi$ , so that partial cancellation of neighboring modes traveling with approximately the same phase velocities occurred. The appearance of such troughs in the transfer function is disadvantageous for the control strategy. Thus, a heater strip length of  $N=10$  was chosen for the numerical investigation of this control concept.

#### 4.1.4 Boundary Layer Control of Two-Dimensional Wave Packets

Using the numerical transfer function discussed previously a relation is established between the wall vorticity response at a certain position downstream of the heater and the forcing input temperature at the heater. The transfer function is based on a linear model. Gaster (1984) extended the transfer function model to allow for quadratic interaction of frequency components. For the high amplitude forcing in the experiments, using suction and blowing through a hole in flat plate, the quadratic interaction term accounted for approximately 5% of the total response. Therefore, in the control attempt introduced here, the initial forcing temperatures are chosen to be small enough, so that the amplitudes of the resulting disturbances are below the threshold for the nonlinear effects to be important. As a result, once the effect of a pulse temperature disturbance is known through the transfer function, it follows that the effect of other disturbance forms is known as well.

For the control of wave packet disturbances in the boundary layer two heater strips were assumed on the plate surface. The strategy for the attenuation of the disturbances in the boundary layer is as follows: In a first computation a wave packet disturbance is created in the flow field using only the upstream heater strip. From this computation the amplitude- and phase-spectra of the wave packet disturbance are found from the wall vorticity signals at all grid points downstream of the first heater. This computation provides information for a flow when no control is applied. From a second computation, where only the downstream heater strip is activated and the first heater strip is left passive, the amplitude- and phase-spectra of the vorticity response are determined. This second computation provides the necessary information for numerical calculations of the transfer function as explained in the previous section. Then, for the attenuation of wave packet disturbances, a third computation is

performed with both heater strips activated. The first heater strip creates a wave packet disturbance with the same temperature input signal as in the first computation. However, the second heater strip acts now as a controller whose temperature input has to be determined so that the disturbances are attenuated downstream of the controller. The control temperature is found by the relation

$$\hat{I}_{x_0}(F) = \hat{O}_{x_1}(F) / \hat{H}(F), \quad (4.14)$$

where  $\hat{O}_{x_1}(F)$  denotes the complex vorticity amplitudes of the first computation, and  $\hat{H}(F)$  is the transfer function from the second computation. In the frequency domain, the phases of  $\hat{O}_{x_1}(F)$  of each frequency component are shifted by  $\pi$ , yielding the desired phases of the control temperature input. Then the inverse Fourier transform of the complex temperature amplitudes (4.14) yields the temperature input for the controller strip in the time domain.

In order to establish the numerical transfer function, the streamwise distance  $x_1 - x_0$  of the sensor location from the center of the controller strip was varied. For a sensor position too close to the controller strip, the transfer function spectrum is influenced by the locally high vorticity spikes, which are created directly at the strip surface. If the sensor is moved too far downstream, the characteristic distribution of the amplitude spectrum has narrowed considerably and the transfer function  $H$  has lost information at the lower and the upper frequency components due to the very low amplitude level in the spectrum. Figure 21 shows the modulus of the transfer function at several positions downstream of the controller strip. Downstream from the position  $x/\Delta x = 88$ , the moduli of the transfer functions nearly coincide within the frequency region  $.7 \leq F \leq 2.0$ , where the curves are almost horizontal. At frequencies  $F \geq 2$ , the moduli branch out quickly due to the strong damping of the frequency components for large  $F$ . After several tests, the transfer function at the station

$x/\Delta x = 92$  was picked for the control strategy. Figure 22 shows the temperature control signal for the disturbance with the characteristic time delay and the typical wave packet shape.

For a computation with two heater strips the control strategies which were introduced above have been applied. The first heater created a wave packet disturbance using the forcing signal  $T_c$  of the relation (4.6), while the second heater strip used the control temperature shown in Figure 22. Figure 23 shows the amplitude and phase spectra obtained from the wall vorticity signal at several streamwise positions for the case where control was applied. The first amplitude spectrum was determined at station  $x/\Delta x = 50$  which is before the controller strip and may be used as reference to compare with the downstream spectra. The second amplitude spectrum at  $x/\Delta x = 80$  is exactly at the end of the controller strip and shows a strong increase in amplitude. However, this increase is due to the locally strong vorticity at the heater surface which creates the antiphase wave packet. Further downstream at the positions  $x/\Delta x = 110, 140,$  and  $170$ , the amplitudes are reduced by more than a factor of ten as compared with the uncontrolled case. The wave packet signal of the wall normal velocity component (Figure 24) at  $y/\Delta y = 20$  (outside the boundary layer) shows the same attenuation trend of the wave packet. Thus the control of the wave packet disturbances is not just a wall effect. The most unstable disturbances in the wave packet were attenuated by about 97% of their uncontrolled levels.

An alternative approach to the above control strategy could be based on an additional sensor placed upstream of the controller strip. Then the control system exhibits a time delay, which could be found by relating the wall vorticity at the upstream sensor to the wall vorticity at the downstream sensor. In addition to the above described strategy based on (4.13), a time shift operator similar to (4.13) but

based on the wall vorticity at the upstream sensor as the input quantity, would be used. This would account for the time delay of the disturbances between the upstream and the downstream sensor. Thus, for a realistic control strategy, the disturbances are picked up by the upstream sensor. Then with this signal the required input for the actuator (controller) is calculated (using the technique just discussed) and the actuator heater strip is triggered accordingly. Therefore, for this control strategy, the downstream sensor is only needed once (before the actual control of transition) to establish the transfer function (between the actuator and the downstream sensor) and the required time delay (between the upstream sensor and the downstream sensor). During the actual control of wave packet disturbances, the downstream sensor may be used to check the efficiency of the control technique, that is of the wave cancellation.

The crucial component of this control strategy is the control element based on (4.14) between the wall temperature at the actuator and the wall vorticity at the downstream sensor station. Therefore, in the present work emphasis has been placed on exactly this part of the control strategy.

#### 4.2 Computation of Three-Dimensional Flows

In the later stages of the transition process the instability waves become three-dimensional, and in the experiments preferred spanwise structures can be identified. Therefore, the three-dimensional computations described here assume that the disturbance flow is periodic in the spanwise direction. With a spectral decomposition in the spanwise direction, the equations (3.3) have to be solved for the  $K$  terms of the series representation of (3.1). For the computations of three-dimensional wave packet disturbances, as discussed in the following sections, the maximum spanwise wavenumber is  $K=2$ . The three-dimensional wave packets are created by forcing the

two-dimensional mode ( $k=0$ ) and the first three-dimensional spanwise mode ( $k=1$ ). The wave packet computations here can be viewed as a model to simulate the early stages of transition up to the point when the disturbances become three-dimensional, and where dominant three-dimensional modes exist.

For the three-dimensional computations, the following parameters were used:

$$\begin{aligned} \text{Re} &= 100000, & \Delta x &= 5.0265 \times 10^{-3}, & T_w &= 44^\circ\text{C}, & K &= 2, \\ L &= .05 \text{ m}, & \Delta y &= 2.8461 \times 10^{-1}, & \gamma &= 20, & Y/\Delta y &= 81, \\ x_0 &= 1.2169, & \Delta t &= 3.74 \times 10^{-3}, & T_\infty &= 24^\circ\text{C}, & X/\Delta x &= 901, \\ \text{Re}_{\delta_1}(\text{at } x_0) &= 600, & \alpha &= 25, & \text{Pr} &= 6.3, & \text{Re}_{\delta_1}(\text{at } x_N) &= 1304. \end{aligned}$$

The height of the integration domain  $Y$  was chosen so that at the inflow boundary  $Y = 12\delta_1$ . This results in a boundary layer thickness at the outflow boundary of approximately  $1/2 Y$ .

#### 4.2.1 Linear Spatial Stability Theory

For the selection of the spanwise wavenumber  $\gamma$  of the three-dimensional computations, the linear stability theory was used to give an overview of the linear amplification of pairs of oblique modes, their phase velocities and the spanwise to streamwise wavenumber ratios for several frequencies.

For linear spatial stability theory the wavenumber in equation (1.0) is complex  $\alpha = \alpha_r + \alpha_i$  and the circular frequency  $\beta$  is real. Equation (1.0) is based on the the assumption of a two-dimensional disturbance wave. The three-dimensional derivation of (1.0) follows from assuming three-dimensional waves of the form  $\phi(y) \exp(\alpha_3 x + \gamma_3 z - \beta_3 t)$ , and assuming a parallel, two-dimensional base flow  $\underline{U}_{base} = (u_{base}(y), 0, 0)$ . With the aid of the Squire's transformation (Drazin and Reid, 1981), a three-dimensional, oblique disturbance wave can then be found from equa-

tion (1.0) through

$$\alpha_2 = (\alpha_3^2 + \gamma^2)^{1/2}, \quad \alpha_2 \text{Re}_2 = \alpha_3 \text{Re}_3, \quad \frac{\beta_3}{\alpha_3} = \frac{\beta_2}{\alpha_2}, \quad (4.15a,b,c)$$

where the subscripts 2 and 3 refer to the two-dimensional and the three-dimensional modes, respectively, and where  $\text{Re}_3$  is the equivalent three-dimensional Reynolds number. The phase velocity  $c$  of equation (1.0) must then be replaced by  $c = \beta_{3D}/\alpha_{3D}$ , which is the three-dimensional component in the streamwise direction.

Since we study pairs of oblique waves, which propagate with a wave angle  $\tan^{-1}(\gamma / \alpha)$  to the streamwise direction of equal and opposite sign, the amplification rate in spanwise direction  $\gamma_i$  is assumed to be zero. Then, by specifying the spanwise wavenumber  $\gamma$ , equation (1.0) can be used to calculate the eigenvalues of the pairs of oblique modes.

Figure 25 shows the rate of amplification, the phase velocity and the ratio of the spanwise to streamwise wavenumber, which are obtained from the linear stability theory. The eigenvalues are shown for two streamwise positions  $\text{Re}_{\delta_1} = 800, 1200$  and for pairs of oblique modes with  $\gamma = 10, 20, 30, 40$ , and the two-dimensional mode with  $\gamma = 0$ .

The rate of amplification for the oblique modes decreases with increasing wavenumber for both Reynolds numbers. The maximum amplification shifts to lower frequencies for increasing Reynolds numbers. For both Reynolds numbers the highest rate of amplification is found to belong to a frequency component of the two-dimensional mode ( $\gamma = 0$ ). However, at  $\text{Re}_{\delta_1} = 1200$  for frequencies below  $F = .5$ , the oblique mode with  $\gamma = 10$  shows a locally higher amplification rate than the two-dimensional mode. Although the *maximum* amplification of a frequency is connected with the two-dimensional mode ( $\gamma = 0$ ), at some other frequency a three-dimensional

wave can still be more amplified than a two-dimensional one. Although generally more stable than two-dimensional waves, the three-dimensional waves with a small wavenumber  $\gamma$  can have similar growth rates as the two-dimensional waves.

The streamwise phase velocities are calculated from the relation (4.10) for each frequency and oblique wavenumber  $\gamma$ . For increasing  $\gamma$ , the phase velocities in Figure 25b become higher. Towards the lower frequencies, the phase velocities decrease for the two-dimensional mode. However, for the higher spanwise wavenumbers  $\gamma \geq 20$ , the phase velocities, after first decreasing, start to increase.

Also, Figure 25c shows that the ratio of spanwise to streamwise wavenumber  $\gamma / \alpha$  does not change from the position at  $Re_{\delta_1} = 800$  to  $Re_{\delta_1} = 1200$ . At the first Reynolds number, the wavenumber  $\gamma = 20$  at the frequency  $F = 1.2$  has a ratio of  $\gamma / \alpha = .67$ . At this frequency the two-dimensional mode has a maximum amplification (Figure 25a). At the Reynolds number  $Re_{\delta_1} = 1200$ , where the most amplified modes have shifted to the lower frequencies, the ratio changes to  $\gamma / \alpha = 1.26$  at the frequency  $F = 0.6$ .

For the forcing of the pair of two oblique modes with a wave packet disturbance, the wavenumber  $\gamma = 20$  was selected for the computations. A similar ratio of spanwise to streamwise wavenumber was also reported in the transition experiments of Saric and Thomas (1983) for single frequency components at amplitude levels of .3% to .4% based on free stream velocity. With our wave packet simulations based on initially low amplitude forcing of a wide band of frequency components, we intend to further investigate the role of TS modes in the transition process.

#### 4.2.2 Three-Dimensional Wave Packet Disturbances

Figure 26 shows the instantaneous wall temperature at  $t/\Delta t = 70$  for the two heater strips. The first heater strip was activated with a physical amplitude of the

forcing temperature for the two-dimensional and the three-dimensional mode of  $A_{2D} = A_{3D} = 20^{\circ}\text{C}$ . The forcing period is  $TP = 120$  and the second heater strip is passive. The temperature signal was recomposed by summing the series (3.1), and the spanwise extent of the integration domain was chosen to comprise two spanwise wavelengths. The strong three-dimensional forcing of the wall temperature is visible in the two temperature peaks which are one spanwise wavelength  $\lambda_z$  apart.

The disturbance signal of the spanwise wall vorticity at several instances in time is shown in Figure 27 for the two-dimensional  $\omega_z_{k=0}$  and the first three-dimensional spanwise mode  $\omega_z_{k=1}$ . At the first timestep  $t/\Delta t = 180$  (the end of the forcing is at  $t/\Delta t = 120$ ), the trailing side of the wave packet illustrates the non-stationarity of the base flow due to the unsteady heating, which is an effect discussed earlier in conjunction with the computations for purely two-dimensional flow. The three-dimensional wave packet propagates in the downstream direction and spreads due to dispersion. The wall normal velocity components  $v_{k=0}$  and  $v_{k=1}$  at a wall normal location  $y/\Delta y = 40$  outside the boundary layer (Figure 28) also confirm a traveling wave packet. At the time level  $t/\Delta t = 180$ , the unsteady heating effect is not visible since the thermal wake remains confined inside the boundary layer.

The spectrally decomposed streamwise velocity components  $u_{k=0}$  and  $u_{k=1}$  are displayed in Figure 29 in the vertical (x-y) plane at  $z=0$ . Shortly after the end of the wave packet excitation at timestep 130 (the duration of the excitation is until timestep 120), the streamwise disturbance velocity contours indicate a wave packet for both the two-dimensional ( $k=0$ ), and the three-dimensional ( $k=1$ ) component. In this early stage the spatial selection of the unstable frequencies is not yet fully completed.

At the later timestep 1200 (Figure 30), the wave packet has spread considerably. The three-dimensional component has spread over less cycles than the two-

dimensional one. This indicates that the difference of phase velocities between individual frequency components for the three-dimensional mode is less than the difference of phase velocities for the two-dimensional mode. Also, a third group of disturbance extrema in the velocity contours of the three-dimensional mode can be identified in the immediate vicinity of the wall.

For the spanwise vorticity  $\omega_z$  contours in Figure 31, the two- and the three-dimensional modes appear more distinct than for the streamwise velocity at the same time level ( $t/\Delta t=1200$ ). The three-dimensional spanwise vorticity mode has a group of disturbance extrema at the wall surface. Away from the wall, a second group of disturbance extrema of the vorticity along a  $45^\circ$  angle to the x-axis can be distinguished. The magnitude of the disturbance extrema away from the wall is larger than that of the group of extrema on the plate surface. In contrast, the two-dimensional spanwise vorticity mode has a group of disturbance extrema at the wall surface, whose magnitude is larger than a second group of extrema which is located at  $y/\Delta y=15$ .

The amplitude- and phase-spectra of the spanwise wall vorticity  $\omega_z$  for the two-dimensional and the three-dimensional mode are given in Figure 32. The spectra are recorded at several streamwise positions  $x/\Delta x = 90, 100, 110, 120, 130$  downstream of the first strip. At the station closest to the activator strip, the spectra for both the  $k=0$  and  $k=1$  component are still very broad, and are similar to the temperature input spectrum. However, further downstream the shape of the spectra illustrates the selection mechanism of the boundary layer. The very high and very low frequency components are strongly damped and the characteristic dome-shaped spectrum appears, where the intermediate frequency components are most amplified.

The amplitude spectrum of the  $k=1$  component shows a sharp minimum at a frequency of approximately  $F = .75$ . The phase-spectrum in the neighborhood of this

frequency undergoes a sudden phase change of  $\pi$ , so that modes in the vicinity of this trough cancel each other. The region of amplification for the  $k=1$  spectrum is shifted to lower frequency components compared to the  $k=0$  spectrum. Also, the amplification rates are reduced.

The amplitude spectra of the wall normal velocity component at the same streamwise position and  $y/\Delta y = 40$  (Figure 33) exhibit a similar behavior as for the spanwise vorticity. Furthermore, the three-dimensional component does not indicate the sharp trough in the vicinity of  $F = .75$ . From the position  $x/\Delta x = 110$  on, the amplitude spectra of Figures 32 and 33 are of the characteristic dome-shape of wave packets in the boundary layer. This position is a distance of two heater lengths away from the center of the heater strip in downstream direction.

The streamwise development of the amplitude spectra over a larger distance is illustrated in Figures 34 and 35 for the spanwise wall vorticity and the wall normal velocity component. The positions are at  $x/\Delta x = 180, 260, 340, 420, 500$ . For the spanwise vorticity, the two-dimensional mode amplifies and selects its frequency components according to linear theory. The three-dimensional mode, however, shifts to lower frequency components without increasing amplification. Instead, at the lower frequency range  $F \leq .5$ , frequency components with an initially very low amplitude become amplified. The three-dimensional spanwise vorticity has its first group of disturbance extrema at  $y/\Delta y = 10$ , close to the wall. At the wall surface itself, only a smaller group of extrema is present (Figure 31). By analyzing the spanwise vorticity signal at the position  $y/\Delta y=10$  (Fig. 34c) with maximum disturbance amplitude, the three-dimensional mode shows an increasing rate of amplification of the lower frequency components. As already pointed out by the strictly two-dimensional computations, the rate of amplification can be determined at any wall

normal position for any flow quantities. Although there is no unique amplification rate using the direct numerical simulation to compare with the linear parallel theory, comparisons are usually made from disturbance quantities at their maximum amplitude location. From our computational results we find the best agreement with the parallel theory also for the location with the maximum disturbance amplitude.

The amplitude spectra for the wall normal velocity component in Figure 35 is calculated at  $y/\Delta y = 40$  outside the boundary layer at the disturbance maxima. The amplitude spectra indicate the same stability characteristics as for the spanwise vorticity. The three-dimensional spanwise mode exhibits the shift to lower frequency components together with an increase in amplification.

The amplitude spectra of all the analyzed flow components show a strong growth of the lower frequency components for the three-dimensional mode. The growth rate of these lower frequency components is much higher than the linear growth rates. In contrast, the two-dimensional amplitude spectrum, as for all the analyzed flow components, do not indicate the growth of these lower frequency harmonics.

In Figure 36 a comparison of the experimental amplitude spectra with the computed spectra of the linear spatial stability theory from Gaster and Grant (1975b) is presented. The spectra to the left of Figure 36 are the experimentally determined distributions of the two-dimensional mode and a three-dimensional mode for the streamwise velocity component, which were measured at a wall distance of  $y/\delta = 1.1$  outside the boundary layer. To the right of Figure 36 the computed spectra of the linear stability theory are shown.

From these figures one can clearly identify a broadening of the amplitude spectra for three three-dimensional modes towards the lower frequency components,

which is not present in the linear spectra. From the first appearance of the low frequency "humps" at an early station, the low frequency components eventually take over the whole spectra, so that at the last station the most amplified frequency components are at a lower frequency range than the linear theory could predict.

Also, and even more surprising, the two-dimensional mode does not exhibit the low frequency interaction mechanism of the three-dimensional mode. The two-dimensional spectrum follows closely the linear prediction up to the last station.

Our numerical computations qualitatively indicate the same interaction mechanism for the three-dimensional mode as in the experimental investigation of Gaster and Grant. However, a comparison of our numerical simulation with the experiments can only be qualitative for several reasons. First, the experimental study covered a much larger streamwise region. Second, the wave packet disturbance in the experiment was created through a single hole in the plate surface, such that an isolated three-dimensional wave packet was created rather than a two-dimensional wave packet with a spanwise variation.

In our computations, during the forcing of the wave packet with the two-dimensional and one three-dimensional mode, a second spanwise mode with the wavenumber  $\gamma = 40$  is created also. This second spanwise mode results from a non-linear interaction of the first spanwise mode with itself during the temperature forcing over the heater strip. However, the amplitudes of all frequency components of this second mode wave packet were small compared to the two-dimensional and first three-dimensional modes. All frequency components of this second mode are damped within a short distance from the heater strip. For the wavenumber  $\gamma = 40$  of the second spanwise mode, the linear spatial theory predicts damping. The rate of damping is further increased for larger Re numbers.

The amplification of the lower frequency components for the three-dimensional spanwise mode indicates the presence of a subharmonic amplification mechanism. The amplification of subharmonic frequencies was found experimentally to exist for periodic disturbances in the early three-dimensional stages of the breakdown process (Saric and Thomas (1983), and Kachanov and Levchenko (1984)). Corke (1989) confirmed in an experimental investigation for single frequency disturbances at very low initial amplitudes, that the spectral broadening of the power spectra first appeared in the subharmonic region. There the breakdown process was absent of higher order instability mechanisms, such as proposed in the fundamental breakdown theories.

In Figure 37, a comparison of the phase velocities is made between the two-dimensional mode and the three-dimensional spanwise mode at  $x/\Delta x = 480$  ( $Re_{\delta_1} = 1021$ ) for the wall normal velocity at  $y/\Delta y = 40$ . Above the frequency  $F = .7$  the three-dimensional phase velocities agree with the linear theory. However, below  $F = .5$  the phase velocities are approximately  $.36 U_{\infty}$ . In the low frequency range, where the strong growth of the amplitudes of the three-dimensional modes appeared, the phase velocities deviate from the value of the linear stability theory and level to approximately the constant value. The phase velocities of the two-dimensional mode agree closely with the linear theory.

To summarize the generation process of three-dimensional wave packet disturbances using heater strips, all the flow variables have been recomposed for two spanwise wavelengths and are displayed in the horizontal (x-z) plane in Figures 38 through 43. The grey-shaded contours were taken at the time level  $t/\Delta t = 70$ , the period of excitation being  $TP = 120$ . Superimposed are contours of the wall temperature disturbance, where the zero contour frames the physical dimension of the heater

strip.

The streamwise and wall normal velocity components at their disturbance extrema show the wave packet disturbance aligned with the temperature forcing at the same spanwise position (Figures 38 and 39). During the excitation, there is an upstream effect in the velocity components in addition to the propagation in downstream direction. In comparison, the spanwise wall vorticity (Figure 43) remains more confined to the temperature disturbance during the excitation, although the wave packet has already moved slightly in the downstream direction. The spanwise vorticity disturbance extrema, as for the streamwise and wall normal velocity are aligned with the temperature disturbance extrema. The strong coherence between the spanwise vorticity component and the wall temperature confirms their choice for the estimation of the transfer function.

A different picture is displayed for the purely three-dimensional variables  $w'$ ,  $w'_x$ ,  $w'_y$  (Figures 40 to 42). There, the disturbance extrema are centered between the wall temperature extrema, and these disturbances vanish where the local spanwise temperature gradient is zero. During the forcing of the wave packets, the streamwise wall vorticity  $\omega_x$  reaches far upstream. Instantaneously, a three-dimensional vorticity field with a large  $\omega_x$  component is created in the boundary layer.

The relation of the streamwise vorticity  $\omega_x$  and the spanwise vorticity  $\omega_z$  at a later time  $t/\Delta t = 1200$  is shown in Figure 44. The grey-shaded contours indicate the streamwise vorticity at the wall surface. The overlaid contours denote the spanwise wall vorticity. In regions where the spanwise vorticity gradients are small, the streamwise wall vorticity disappears. On the other hand, where the spanwise vorticity gradients are large, the streamwise vorticity has its disturbance maximum. The stream-

wise vorticity disturbance is concentrated along the streamwise direction between the the peak and valley positions as marked by the spanwise wall vorticity.

#### 4.2.3 Boundary Layer Control of Three-Dimensional Disturbances Waves

For the control of three-dimensional wave packet disturbances the same transfer function strategy as for the two-dimensional case (see 4.1.3) is used. Since the three-dimensional equations are already decomposed in the spanwise direction, an additional transfer function relating the three-dimensional spanwise vorticity to the three-dimensional temperature forcing can be introduced analogously to (4.13):

$$H(F)_{k=1} = \frac{\hat{O}_{k=1, x_1}(F)}{\hat{I}_{k=1, x_0}(F)} \quad (4.16)$$

Once the effect of a three-dimensional temperature input is found using (4.16), then a controller signal can be created for the attenuation or the reinforcement of the disturbance components. The procedure to find the control temperature for disturbance attenuation is similar to the procedure which was discussed in section (4.1.4.) in connection with the purely two-dimensional disturbance computations. However, now each spanwise component has to be treated individually.

The moduli of the transfer function for the two-dimensional and the three-dimensional mode at several streamwise positions are given in Figure 45. The two-dimensional mode exhibits the same behavior as in the purely two-dimensional computations. The moduli have a constant amplitude ratio within the band of linearly amplified frequencies. For frequency components above  $F = 1.8$ , the moduli of the transfer function change rapidly with respect to the streamwise direction.

The moduli of the three-dimensional transfer function, however, show a pronounced trough in the vicinity of the frequency  $F=0.75$ . This effect could already be expected from the amplitude spectra of Figure 32. The rapid phase change near the

frequency component  $F = .7$  leads to partial cancellation in the vicinity of this frequency, since the phase velocities of the neighboring modes of the wall vorticity response are very close to each other.

#### 4.2.3.1 Control of the Two-Dimensional and Three-Dimensional Spanwise Modes

For the attenuation of the two- and three-dimensional wave packet disturbances a transfer function was used, which was selected at the streamwise position  $x/\Delta x = 230$ . The controller strip was placed between the streamwise position  $130 \leq x/\Delta \leq 145$ . The  $x$ -station for the transfer function is approximately two disturbance wavelengths (of the most amplified frequency in the wave packet) downstream from the center of the controller strip.

Figures 46 to 49 show the amplitude spectra for the control of the two- and three-dimensional disturbance components of the spanwise wall vorticity  $\omega'_z$  and the wall normal velocity component  $v'$  at several streamwise positions. The amplitude spectra at the position  $x/\Delta x = 120$  is just upstream of the controller strip and may serve as a reference amplitude.

For the two-dimensional mode, a 90% reduction of the most amplified frequency component was achieved. The three-dimensional spanwise mode control showed an approximately 80% reduction for the spanwise vorticity. The control based on the transfer function for the three-dimensional spanwise vorticity is not quite as successful as the control for the two-dimensional, spanwise mode. The three-dimensional vorticity has its primary disturbance maximum away from the wall. A more successful estimation of the transfer function of the three-dimensional mode might be found away from the wall or using the streamwise vorticity.

#### 4.2.3.2 Control of the Two-Dimensional Mode

Finally, control of only the two-dimensional mode has been attempted. By suppressing the two-dimensional mode in the wave packet it was hoped to gain insight on the development of the subharmonic frequency modes which are present in the three-dimensional disturbance development of the uncontrolled flow.

Figure 50 shows the spanwise vorticity  $\omega'_z$  in the horizontal plane at the plate surface for the attenuation of the two-dimensional mode only (grey-shaded contours) at the time 1200. The spanwise vorticity of the uncontrolled flow is overlaid as line contours. The suppression of the two-dimensional mode advances the spanwise vorticity at the valley location. At the peak locations the maxima still coincide. However, the effect of trying to cancel only the two-dimensional mode on the lower frequency interactions can be interpreted better from the amplitude spectra.

In Figure 51, the amplitude- and phase-spectra of the three-dimensional mode of the vorticity at  $y/\Delta y=10$  and the wall normal velocity at  $y/\Delta y=40$  are shown for several streamwise positions. Both flow components are analyzed at their amplitude maxima in wall normal direction. The two-dimensional mode of both flow quantities was attenuated similarly to the "two-mode" control case. The attenuation of only the two-dimensional mode leaves the linear amplification mechanism of the three-dimensional mode intact. However, the strong amplification of the low frequency components of the three-dimensional mode, which were present in the uncontrolled case, are not identifiable now in the amplitude spectrum. The attenuation of only the two-dimensional, spanwise mode of the wave packet disturbance effectively delayed the onset of the nonlinear, subharmonic type interactions.

## 5. Conclusions

A numerical investigation of the control of the transition from laminar to turbulent flow in a flat plate boundary layer flow was undertaken. The numerical method is based on the complete Navier-Stokes equations and allows for the spatial amplification of disturbance waves in a non-parallel boundary layer. For the numerical method finite-differences are used in the streamwise and wall normal directions for the two- and three-dimensional computations, and a spectral Fourier approximation is used in the spanwise direction for the three-dimensional computations. Emphasis is placed on the simulation of two- and three-dimensional wave packet disturbances since they more realistically model the natural transition process than single frequency disturbances. In the numerical simulation flush mounted heater strips on the plate surface were modeled to generate disturbance waves.

We investigated the mechanism by which Tollmien Schlichting (TS) waves are created in the boundary layer through a local viscosity variation. The time dependent heat transfer during the thermal forcing with the heaters locally alters the viscosity, which then imposes a temporal fluctuation on the streamwise velocity profile. Strong vorticity gradients over the heater strip appear instantaneously, thereby generating the TS waves.

During the temperature forcing, in addition to the TS mechanism, a net amount of heat is introduced in the flow field. At the end of the forcing, a region of locally high temperature (heat spot) appears in the vicinity of the heater strip, which is convected in the streamwise direction at a speed much slower than the group velocity of the TS wave packets. The heat spot rapidly diffuses in wall normal direction and almost vanishes at a downstream distance of approximately two heater strip lengths. The effect of this non-stationarity appears in the Fourier analyzed signals as a low

frequency component, which adversely influences our control strategy.

A steady temperature component over the heater strip reduces the effect of this non-stationarity in the sensor signal. However, this introduces a thermal wake in the boundary layer which reaches far downstream, and although its maximum temperature differences are small, it was found that the small changes in the mean velocity profile noticeably altered the local stability characteristics of the flow. This was also verified with linear spatial stability calculations using the base profiles obtained from the Navier-Stokes solutions.

A linear transfer function technique based on the vorticity response at the wall surface and the temperature input at the heater strips was developed. The heating mechanism that creates the TS wave packets over the heater strip is nonlinear due to the inseparability of the momentum and energy equation. However, for low amplitude forcing the vorticity response downstream from the heater strip, the nonlinear effects can be assumed small. The control model based on the transfer function assumes prior knowledge of the disturbances in the flow field. For the study of the applicability of wave packet attenuation in the boundary layer, the uncontrolled disturbance field was first determined with an independent computation. Then, by analyzing the wave packet disturbances for a computation with no control applied, a direct comparison can be made with computations, when control is applied.

A study on varying the heater strip width revealed that for a width of typically one half the wavelength of the dominant unstable frequency component, the vorticity response was maximized. A study on the effect of varying the distance of the sensor location to the actuator location showed that the cancellation of the disturbances was optimized for a distance of approximately two disturbance wavelength of the main frequency component in the wave packet. For a distance closer to the disturbance

actuator the presence of the above mentioned non-fluctuating heat spot adversely affects the control efficiency. Also, for distances further from the actuator the transfer function loses information on the higher frequency range due to the strong spectral filtering of the boundary layer.

Numerical simulations of the control of the boundary layer transition applying the transfer function technique showed that two-dimensional and three-dimensional wave packet disturbances can be drastically attenuated.

For a simulation with no control applied, nonlinear interactions of frequency components of the wave packet first appeared in the lower frequency range of the three-dimensional spanwise mode. The growth rates of the lower frequency components of the three-dimensional mode exceeded the linear growth rates of the TS frequency components. The two-dimensional spanwise mode, however, did not show the low frequency interactions of the three-dimensional mode.

Experimental investigations by Gaster and Grant (1975) also showed the low frequency interaction mechanism in the subharmonic region for the three-dimensional spanwise mode of a wave packet disturbance. This suggests that a resonance mechanism for the three-dimensional disturbances promotes the amplification of a large band of frequency components. However, neither in the present numerical simulations nor in the experiments by Gaster and Grant could a specific higher order interaction mechanism be identified that can be explained by one of the fundamental breakdown theories.

To verify the role of the two-dimensional, spanwise modes of the wave packet on the amplification mechanism in the subharmonic frequency range, a numerical simulation with only the control of the two-dimensional part of the wave packet was investigated. For in this case, no nonlinear amplification of the lower frequency com-

ponents of the three-dimensional modes was present. Although the attenuation of only the two-dimensional mode leaves the linear amplification of the three-dimensional mode intact, the amplitude of the two-dimensional mode influences the nonlinear amplification of the three-dimensional mode considerably.

Future investigations of the control of the wave packet disturbances should concentrate on several points. The effect of the amplification of the three-dimensional mode on the attenuated two-dimensional mode should give further insight on the importance of three-dimensional mode control concepts. For the investigation of the later stages of the breakdown process to turbulent flow, nonlinear interaction necessitates the incorporation of many more spanwise modes. We believed that the transfer function concept can be extended to also include quadratic wave interactions which would become important for the later stages of the transition from laminar to turbulent flow. Also, this transfer function technique is applicable to the control of random two- and three-dimensional disturbances.

## Figures

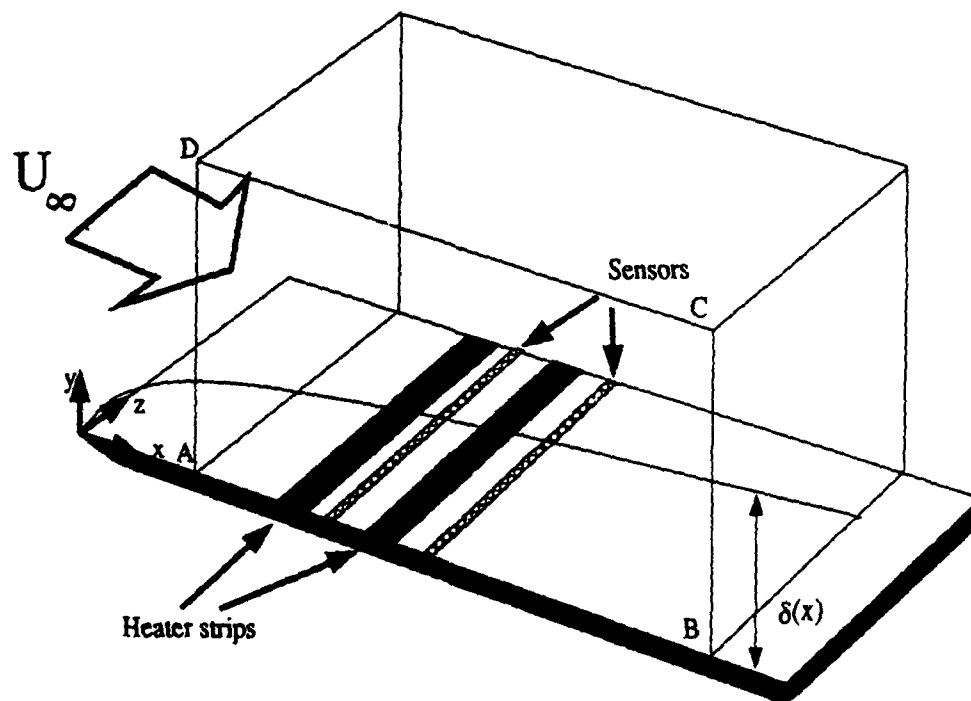


Fig. 1: Computational domain with flat plate model.

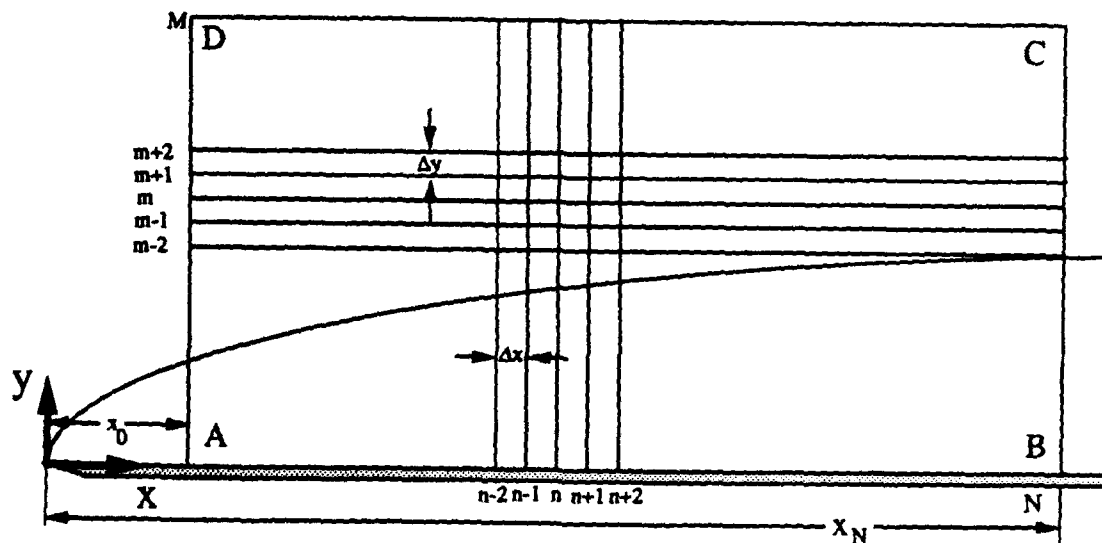


Fig. 2: Computational domain in the x-y plane.

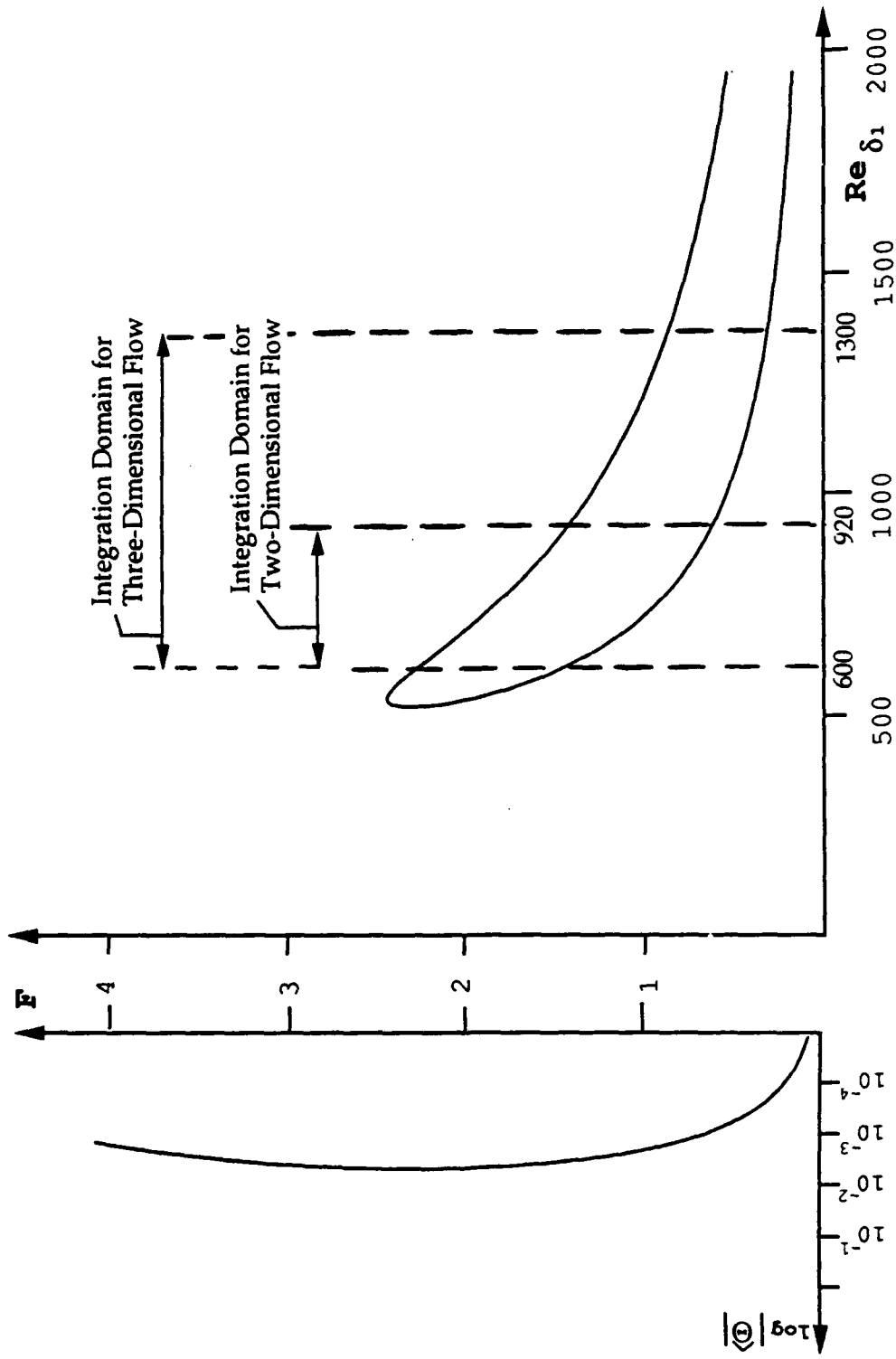


Fig. 3 : Linear stability diagram and the modulus of the input spectrum of the first heater strip.

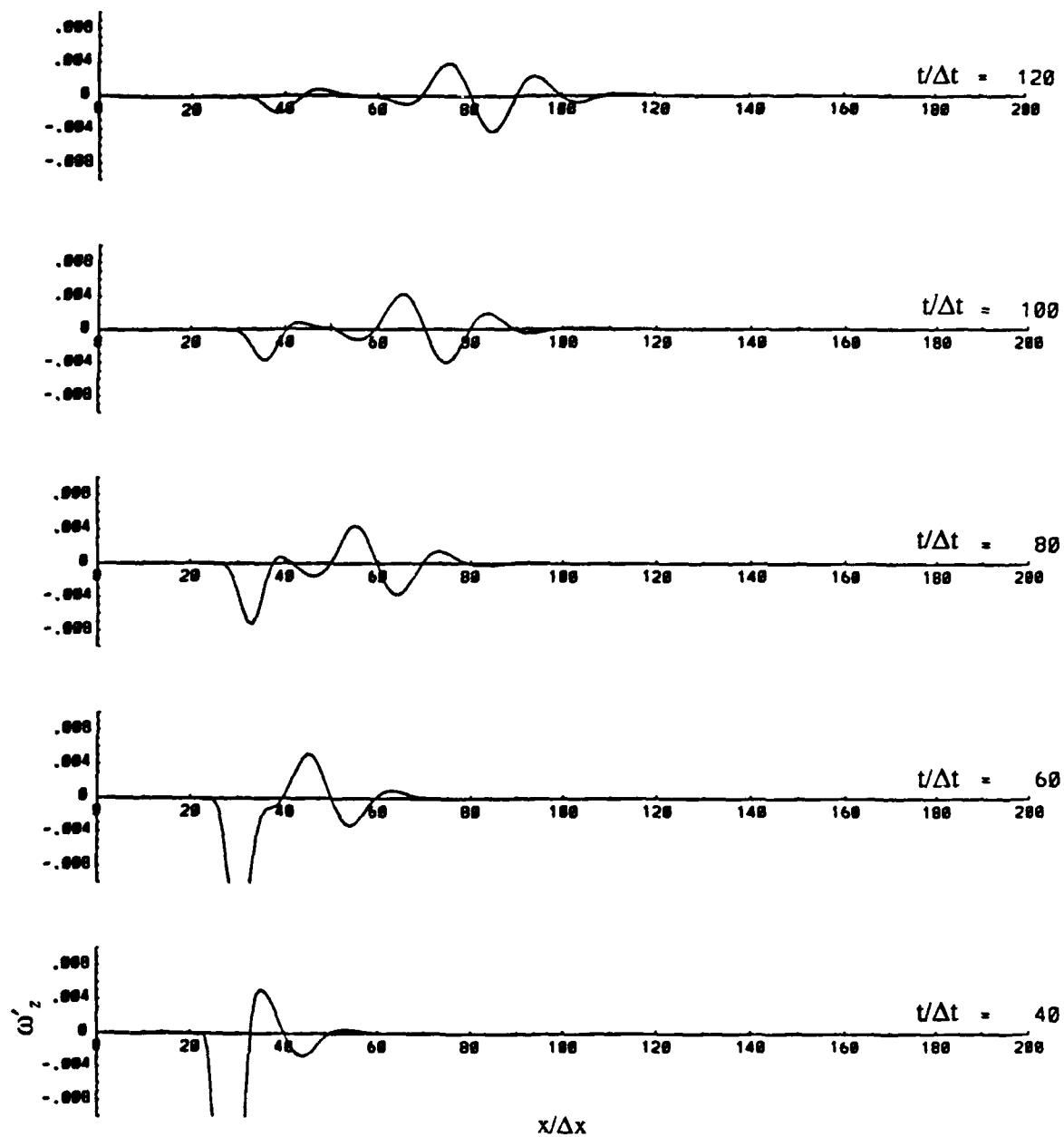


Fig. 4: Disturbance signal of wall vorticity at several timesteps. The heater strip location is at  $20 \leq x/\Delta x \leq 30$  and the forcing is turned off at  $t/\Delta t = 40$  (Case with zero mean temperature over heater strip).

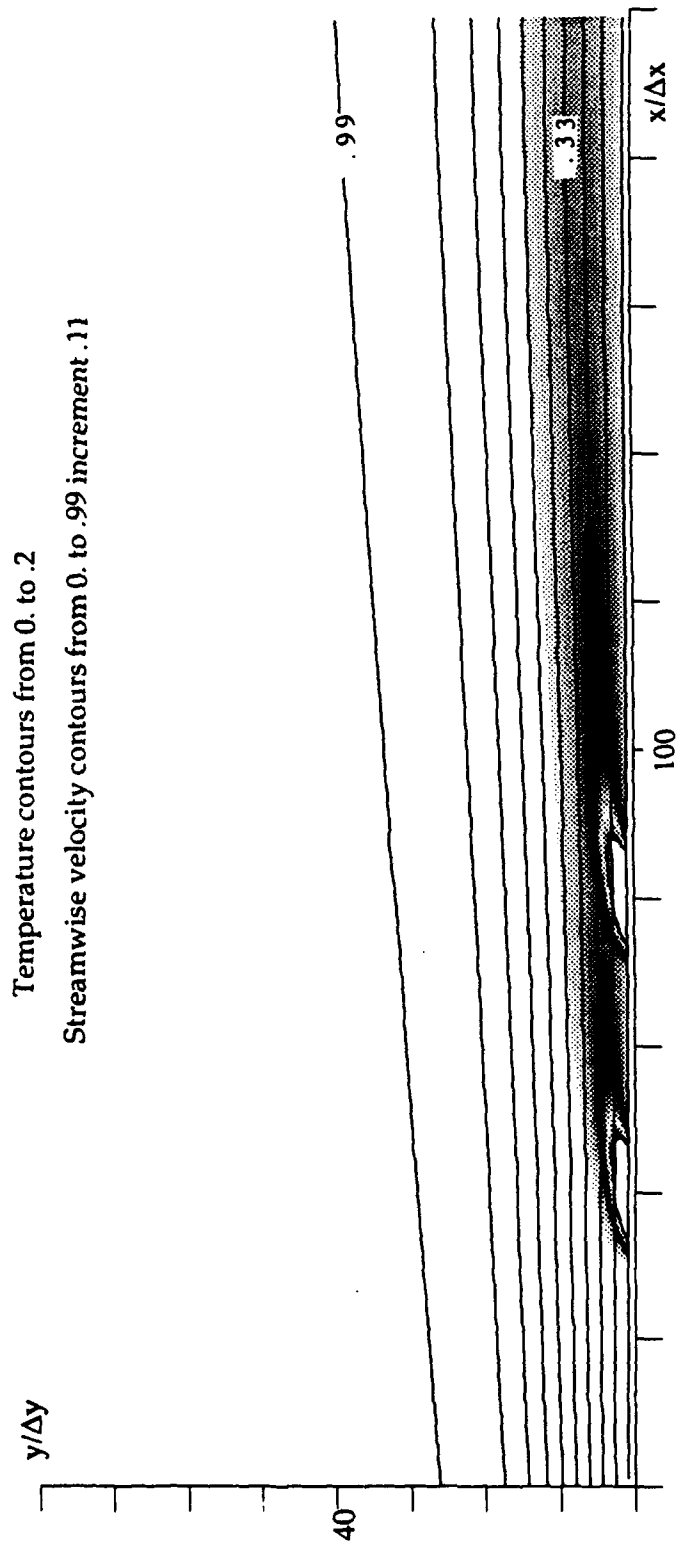


Fig. 5: Temperature contours (grey-shaded) and lines of constant streamwise velocity

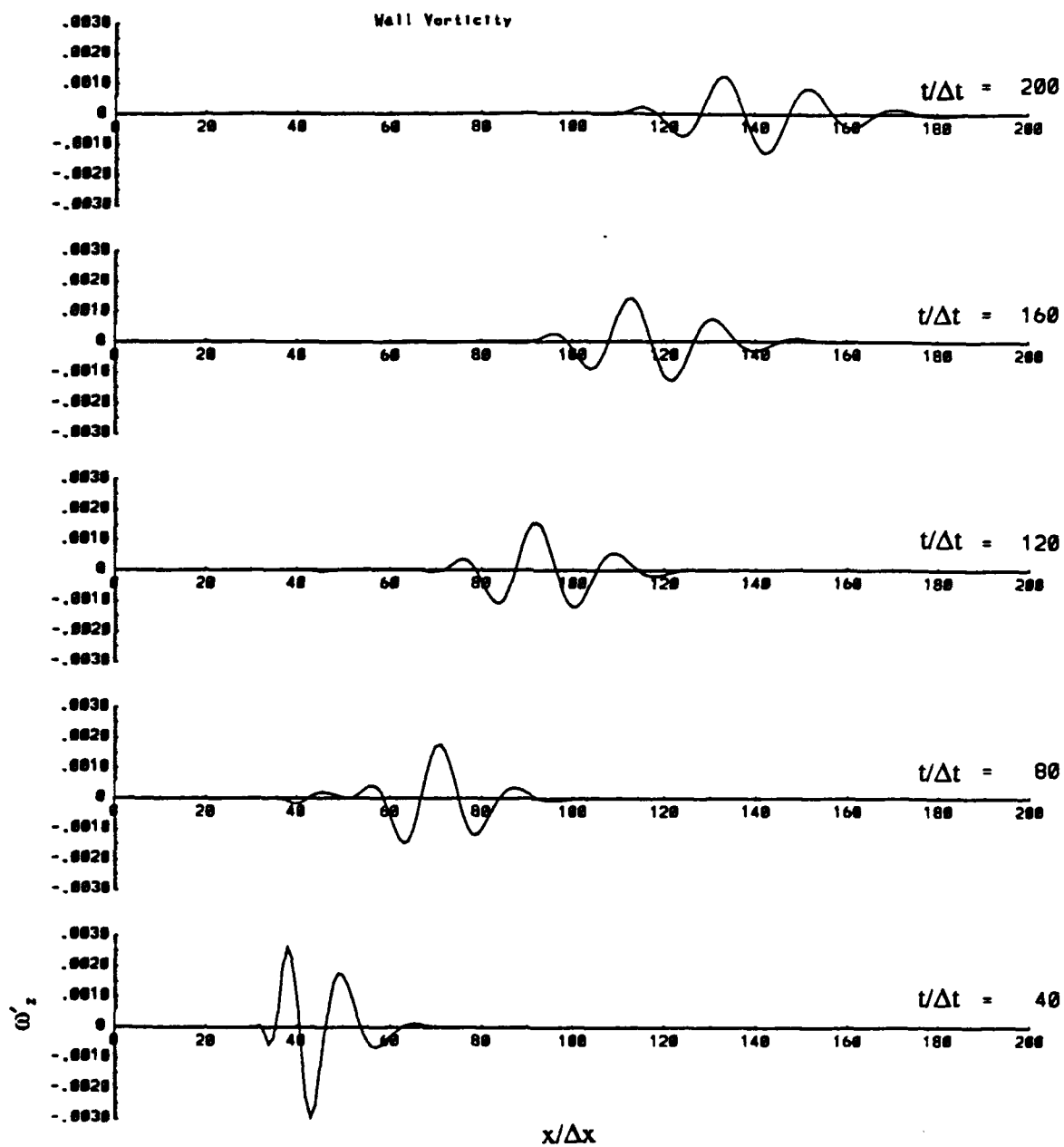


Fig. 6: Disturbance signal of wall vorticity domain at several timesteps with the temperature forcing turned off at  $t/\Delta t = 40$ . The heater strip location is at  $30 \leq x/\Delta x \leq 40$  (Case with steady mean temperature over heater strip).

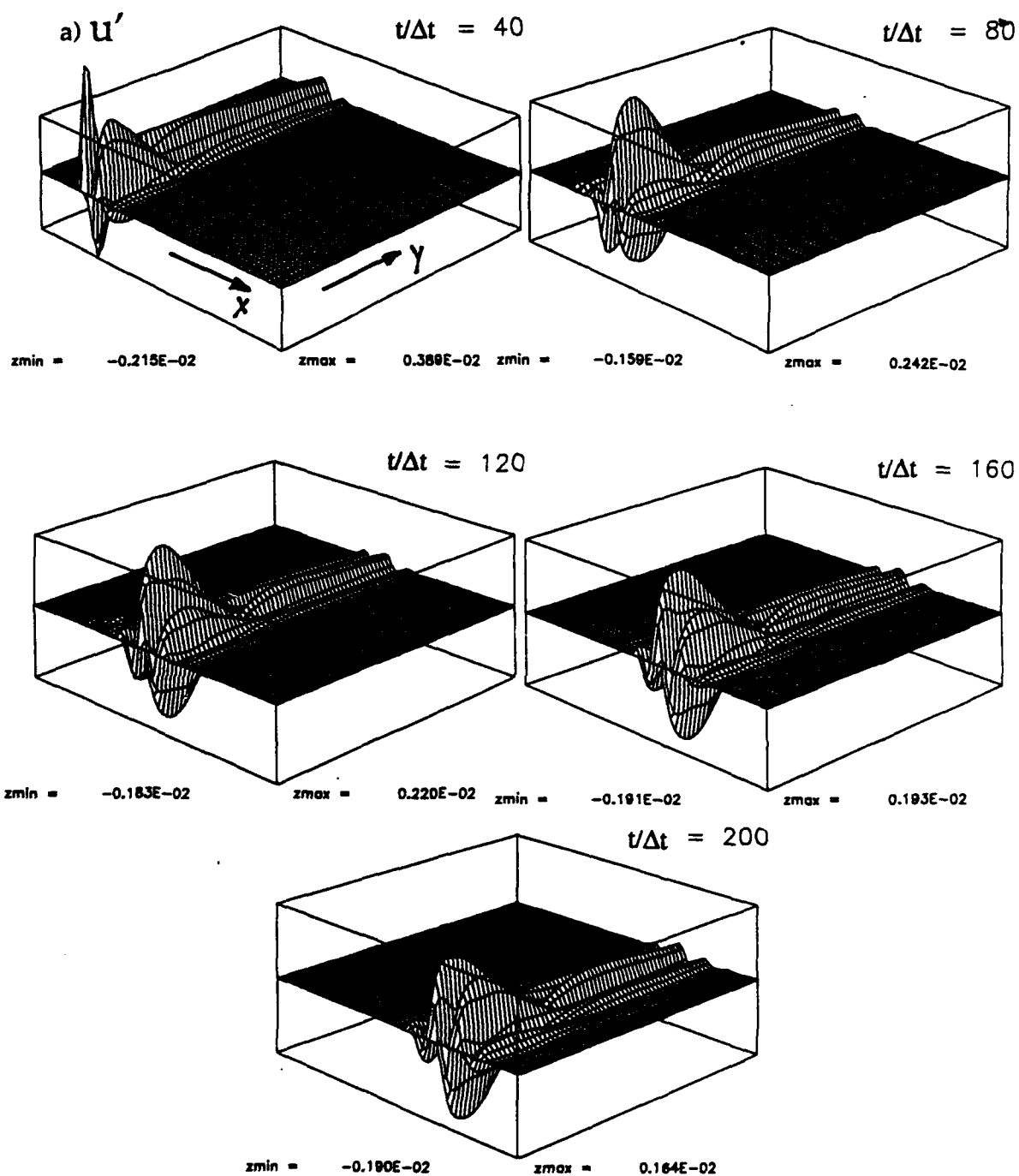


Fig. 7: Perspective representation of the disturbance signal for a)  $u'$  the streamwise velocity component, b)  $v'$  the wall normal velocity component, c)  $\omega'$  the vorticity and d)  $\theta'$  the temperature at five time levels.

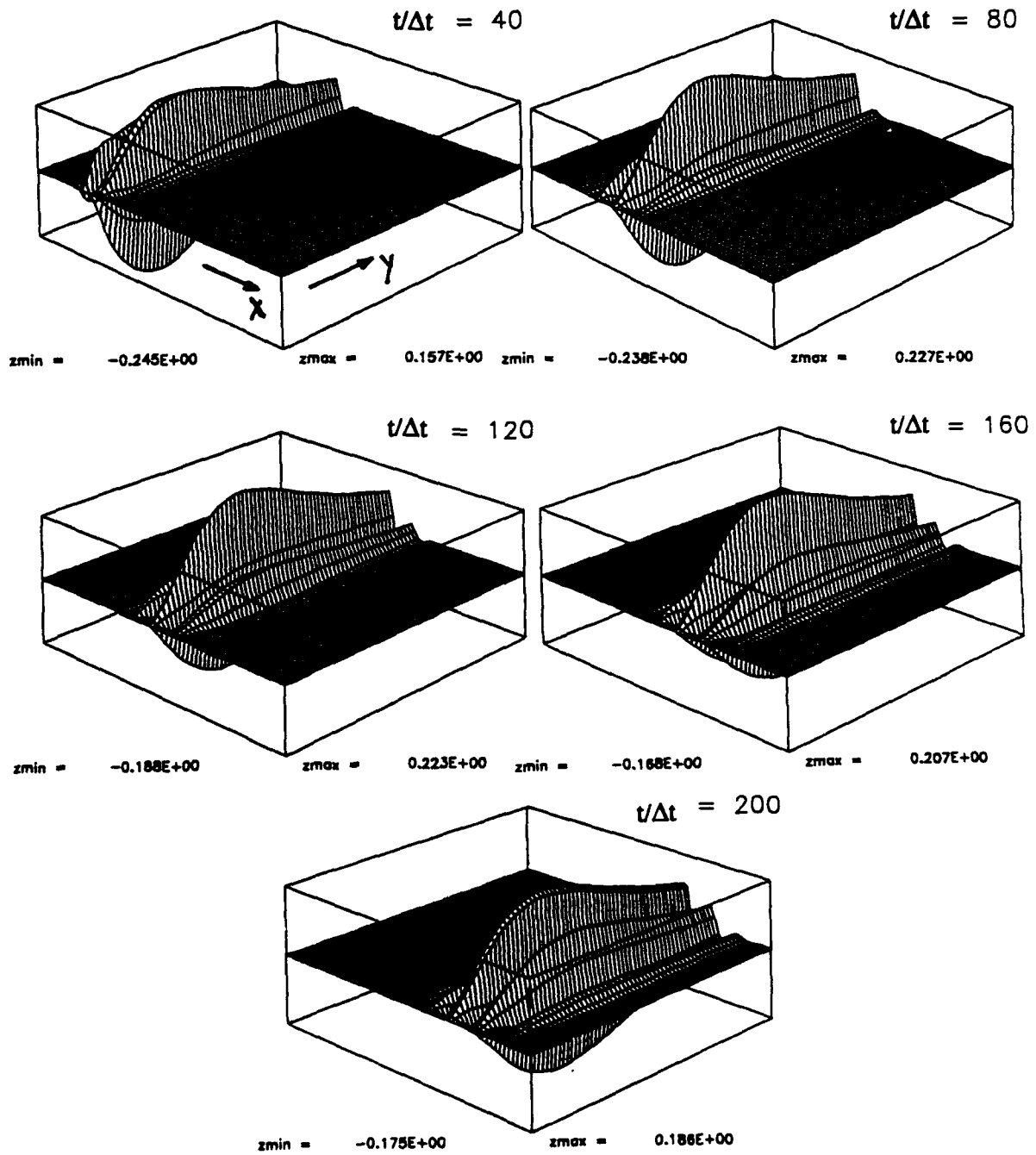
b)  $V'$ 

Fig 7b: continued.

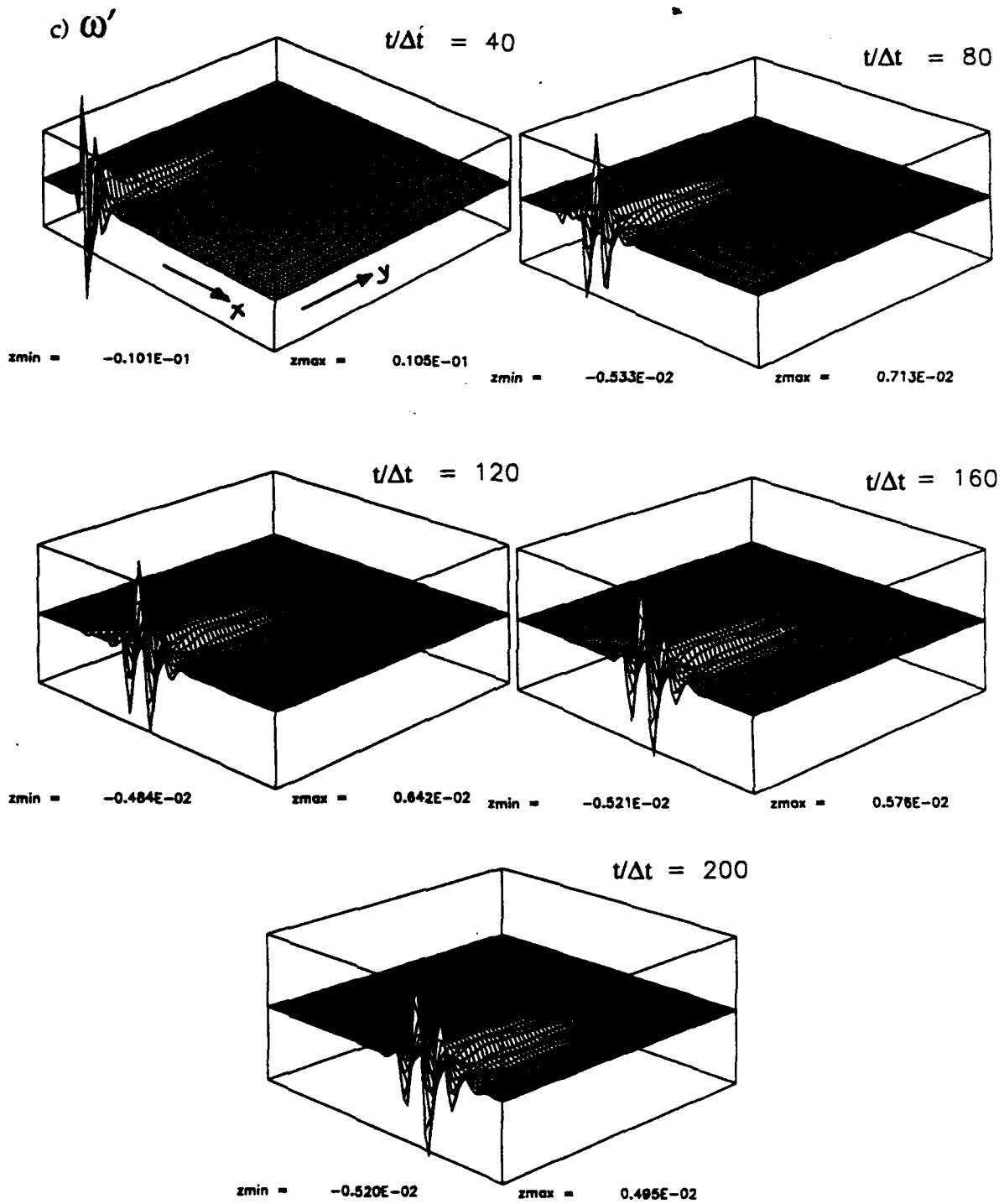


Fig. 7c: continued.

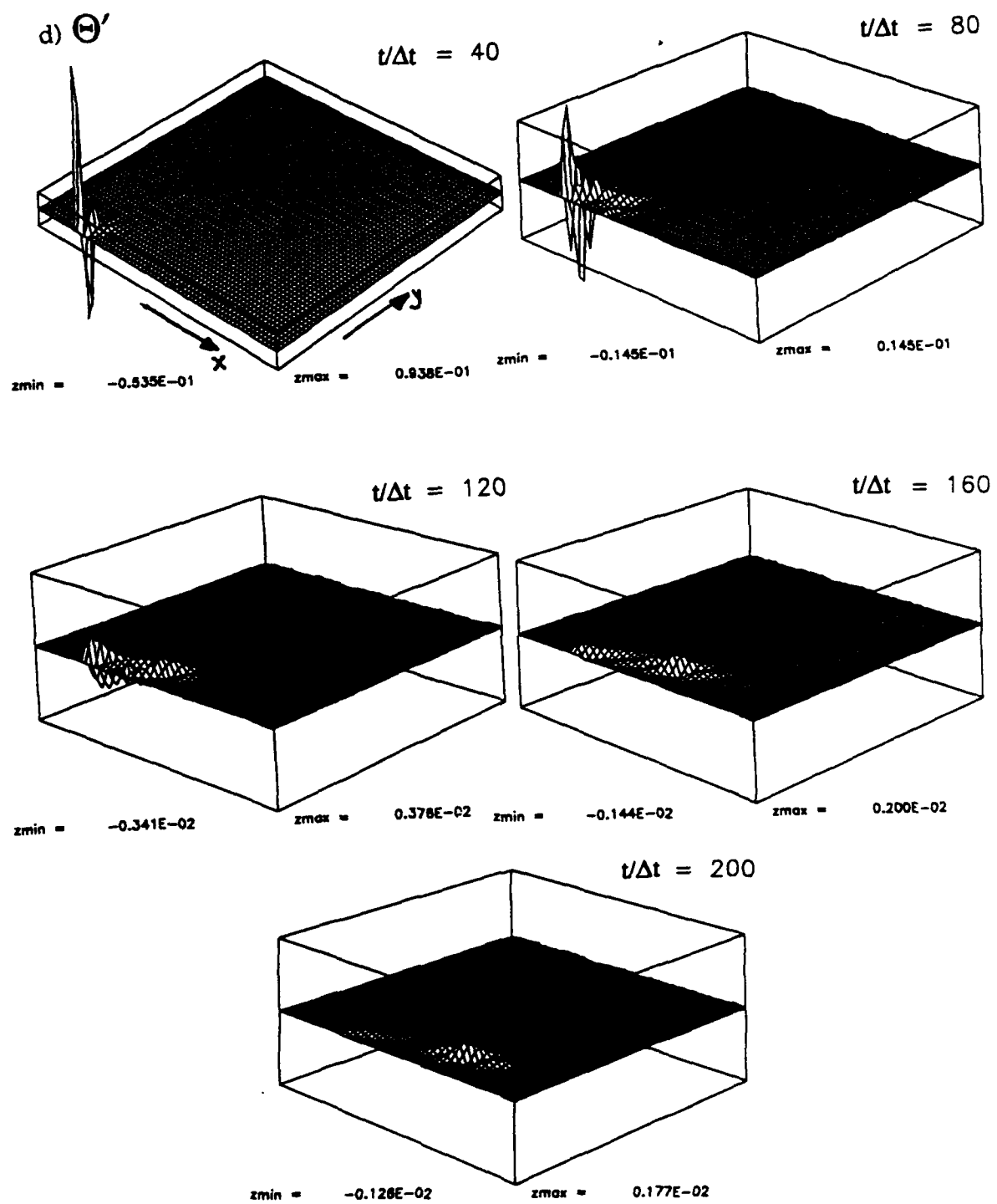


Fig. 7d: continued.

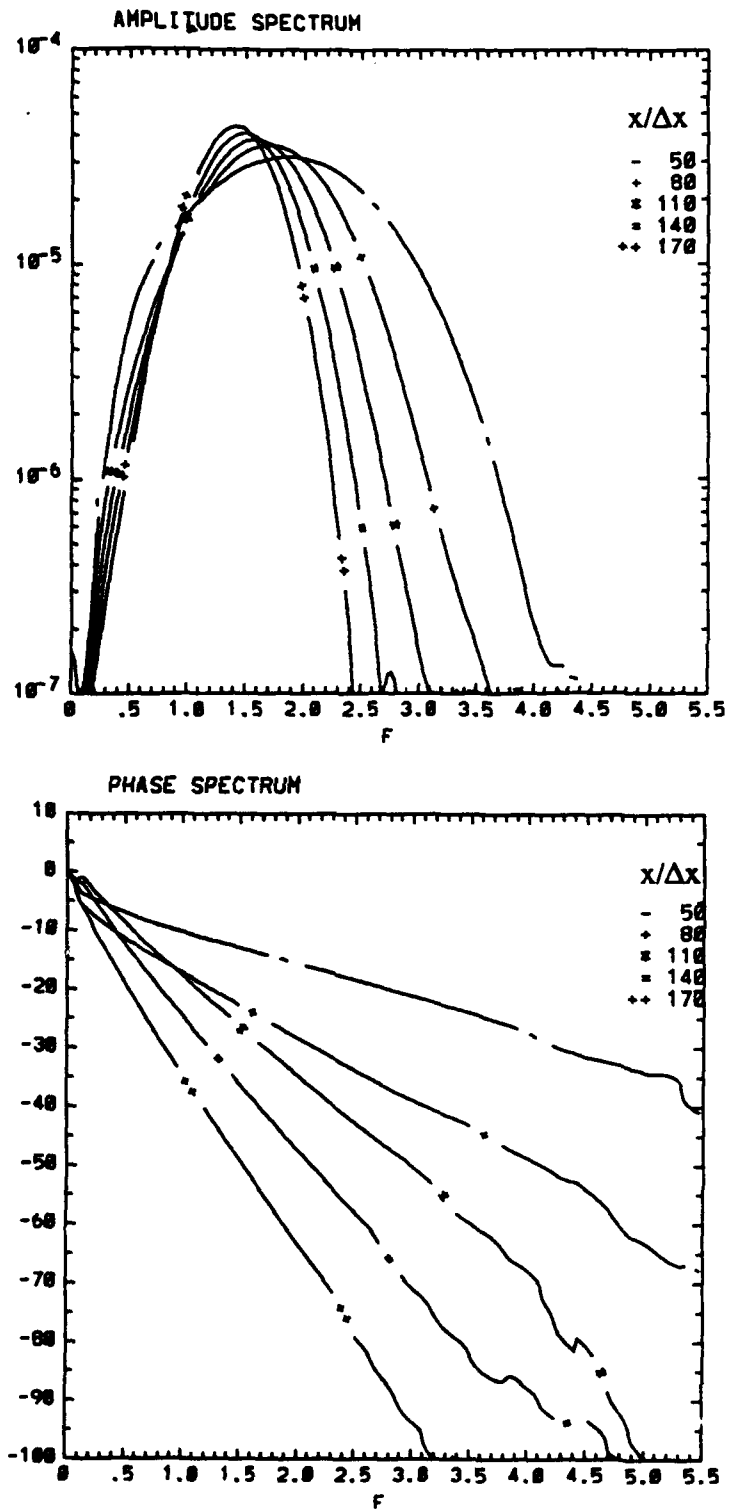


Fig. 8: Amplitude- and Phase- spectra of the wall vorticity signal at several streamwise positions for the case with no control applied.

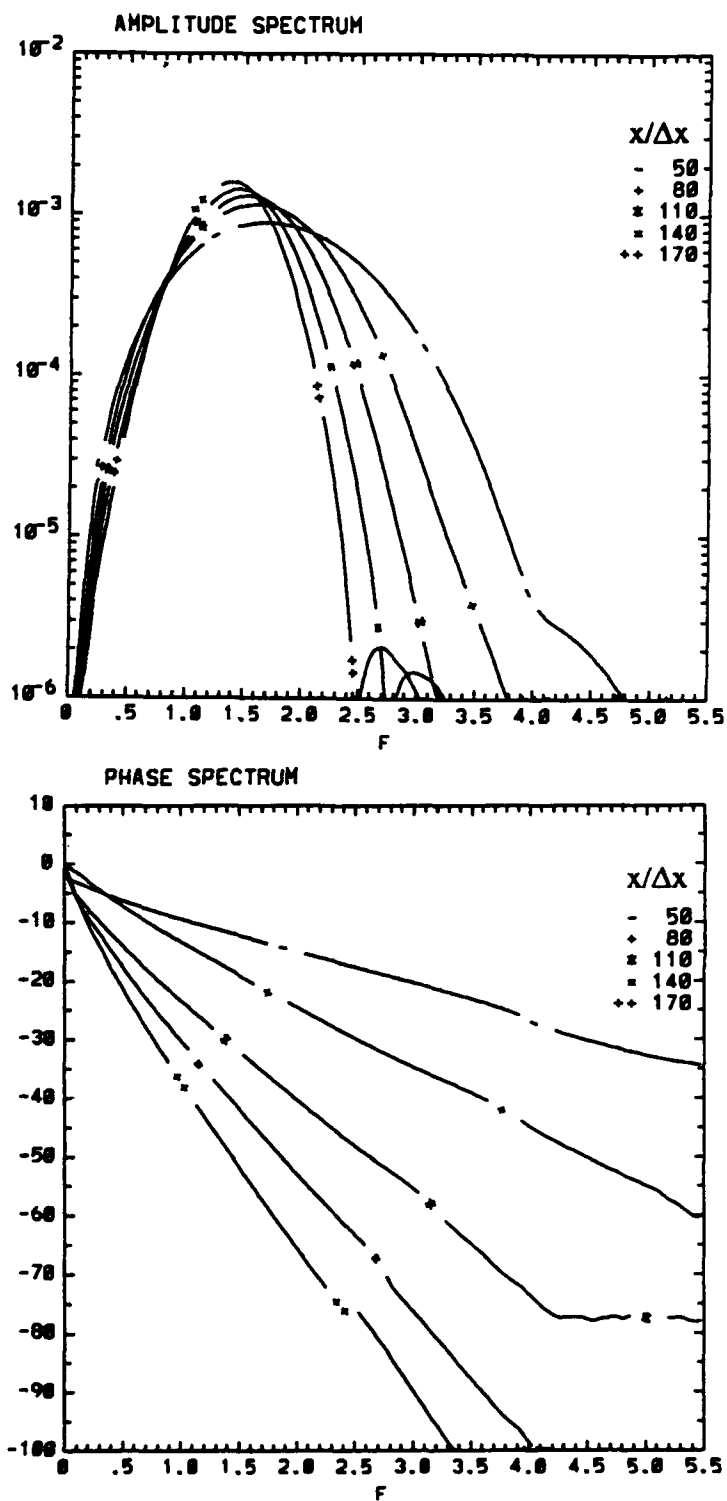


Fig. 9: Amplitude- and Phase- spectra of the wall normal velocity signal at  $y/\Delta y = 20$  at several streamwise positions for the case with no control applied.

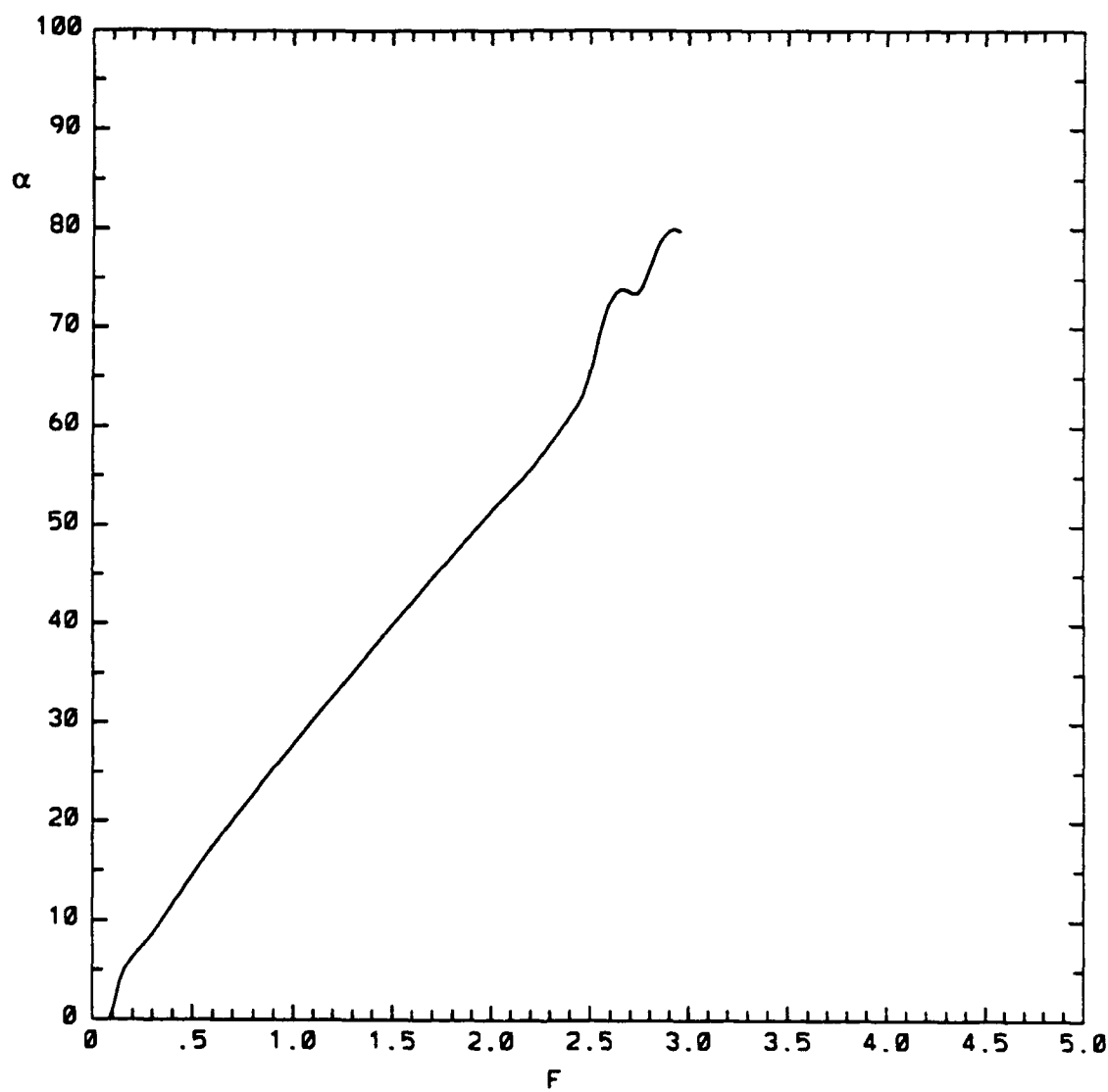
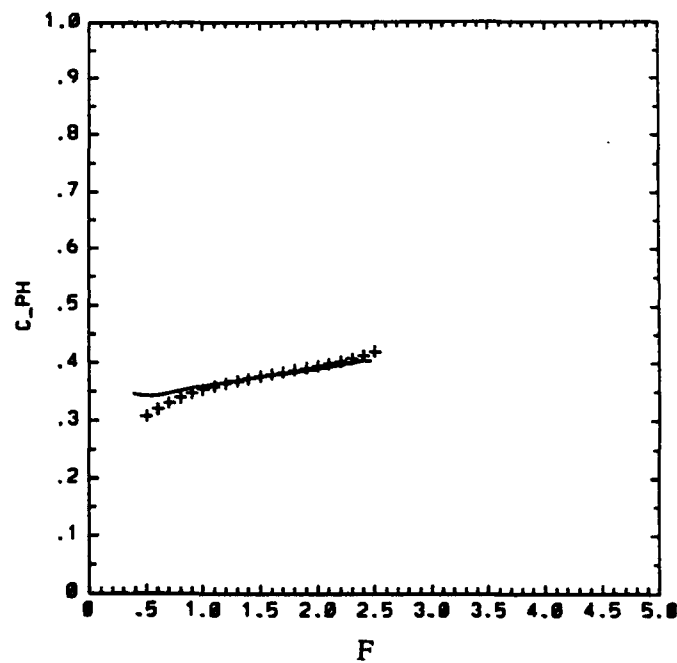


Fig. 10: Dispersion relation of the wall vorticity signal from a Navier-Stokes simulation at the streamwise position  $x/\Delta x = 140$ , ( $Re_{\delta_1} = 835$ ).

a)



b)

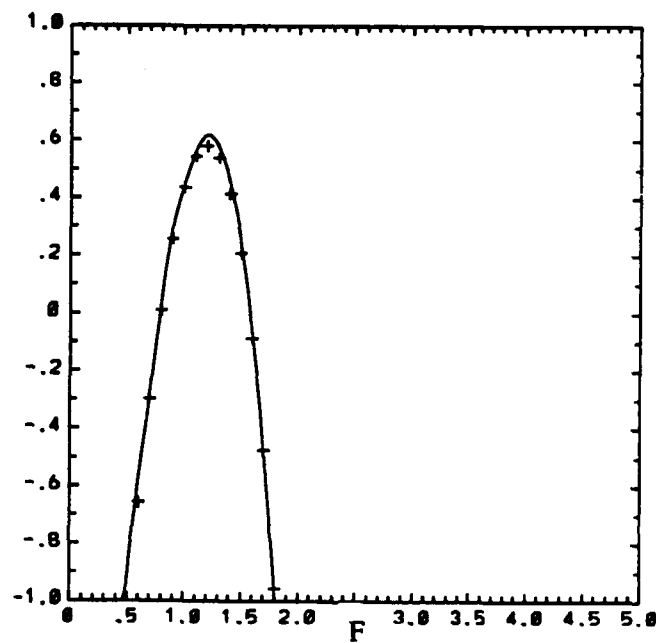
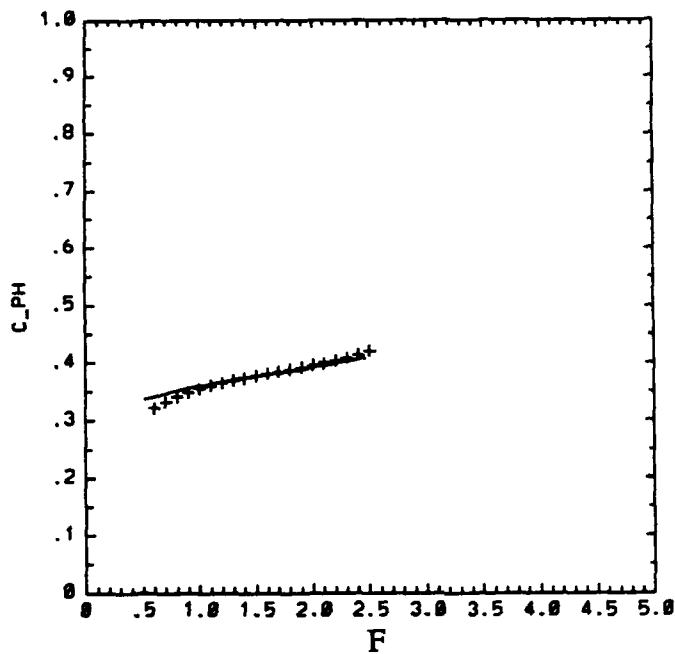
 $-\alpha_i$ 

Fig. 11: Comparison of a) the phase velocity  $c_{ph}$  and b) the rate of amplification  $\alpha_i$  of the Navier-Stokes calculation (solid line) with the linear spatial stability theory ('+' symbols) at the streamwise position,  $x/\Delta x = 140$ , ( $Re_{\delta_1} = 835$ ), by analyzing the wall vorticity signal of the Navier-Stokes simulation.

a)



b)

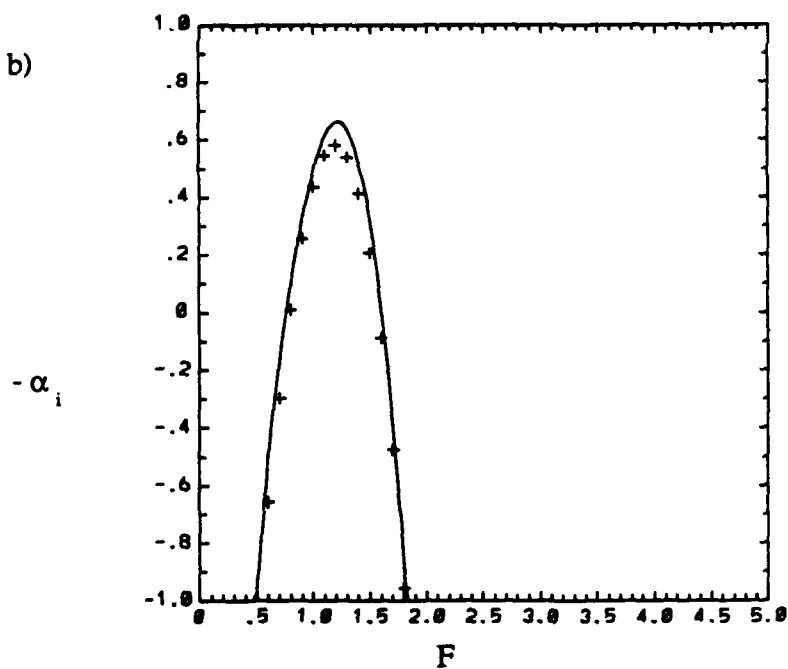


Fig. 12: Comparison of a) the phase velocity  $c_{ph}$  and b) the rate of amplification  $\alpha_i$  of the Navier-Stokes calculation (solid line) with the linear spatial stability theory ('+' symbols) at the streamwise position  $x/\Delta x = 140$ , ( $Re_{\delta_1} = 835$ ), by analyzing the wall normal velocity signal at  $y/\Delta y = 30$  of the Navier-Stokes simulation.

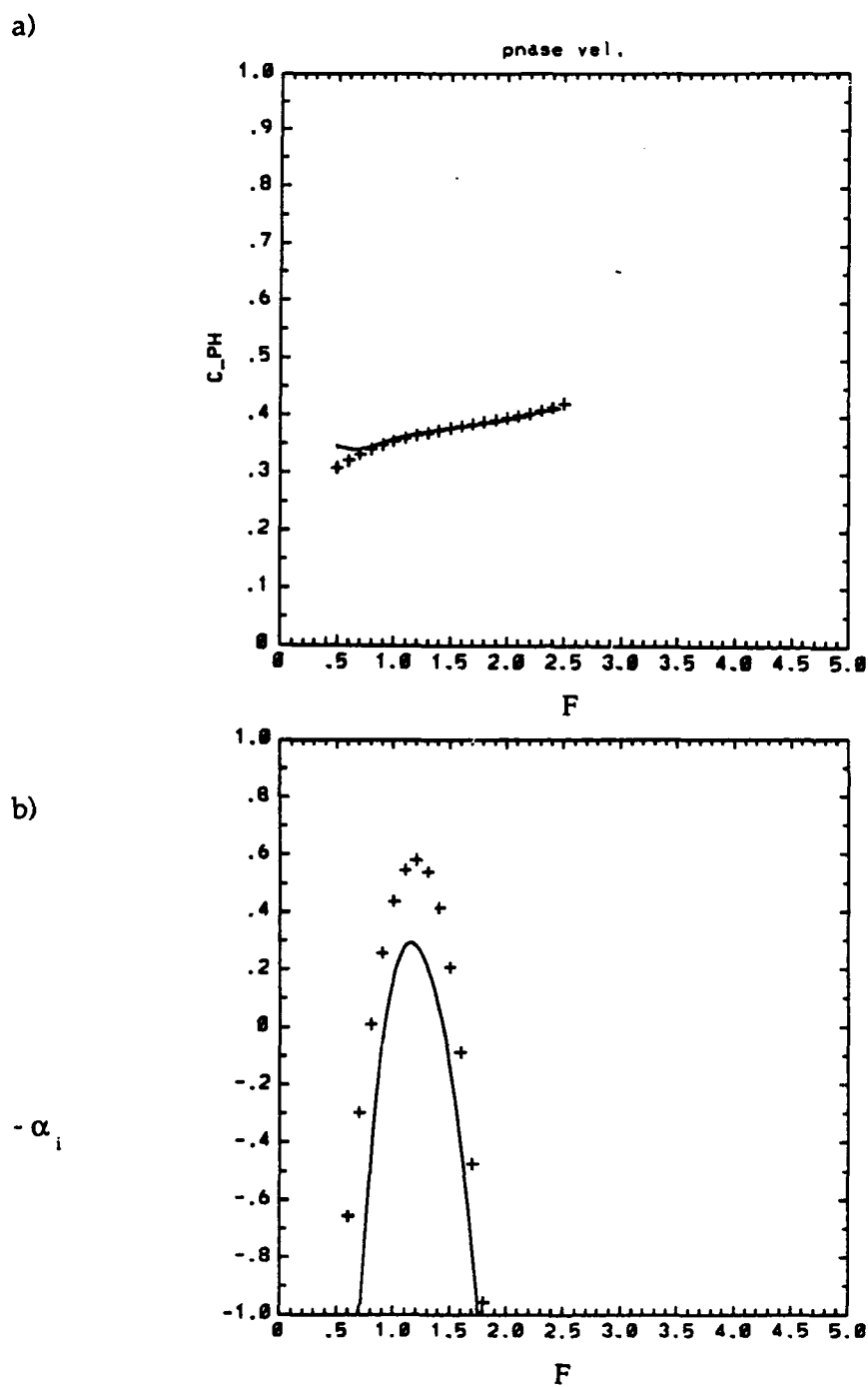


Fig. 13: Comparison of a) the phase velocity  $c_{ph}$  and b) the rate of amplification  $\alpha_i$  of the Navier-Stokes calculation (solid line) with the linear spatial stability theory ('+' symbols) at the streamwise position  $x/\Delta x = 140$ , ( $Re_{\delta 1} = 835$ ), by analyzing the vorticity signal at  $y/\Delta y = 20$  of the Navier-Stokes simulation.

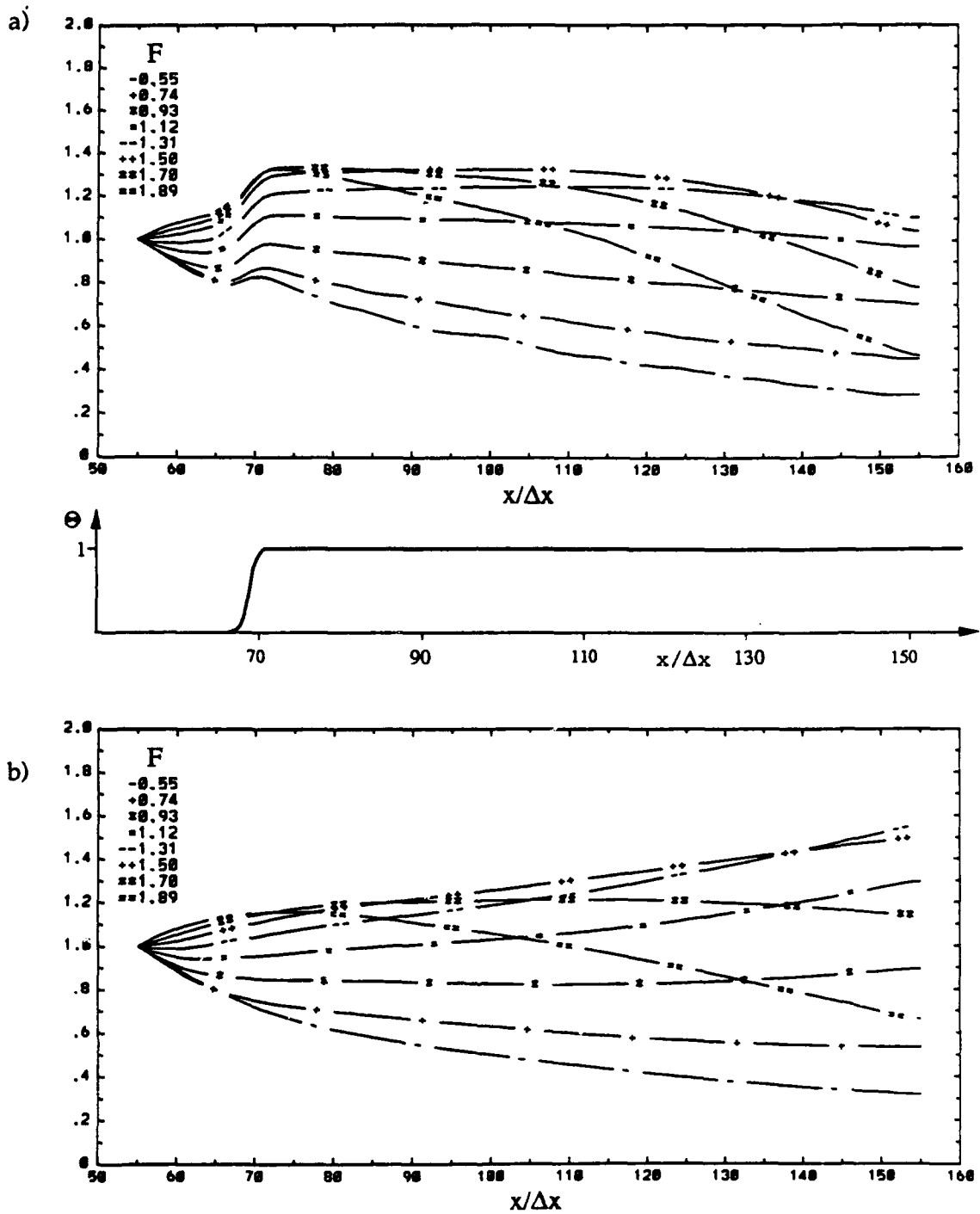


Fig. 14: Streamwise amplification of the wall vorticity for several frequency components of the wave packet disturbance with a) the presence of a heated segment on the plate surface (steady wall temperature distribution shown below figure) and b) without the heated segment.

a)

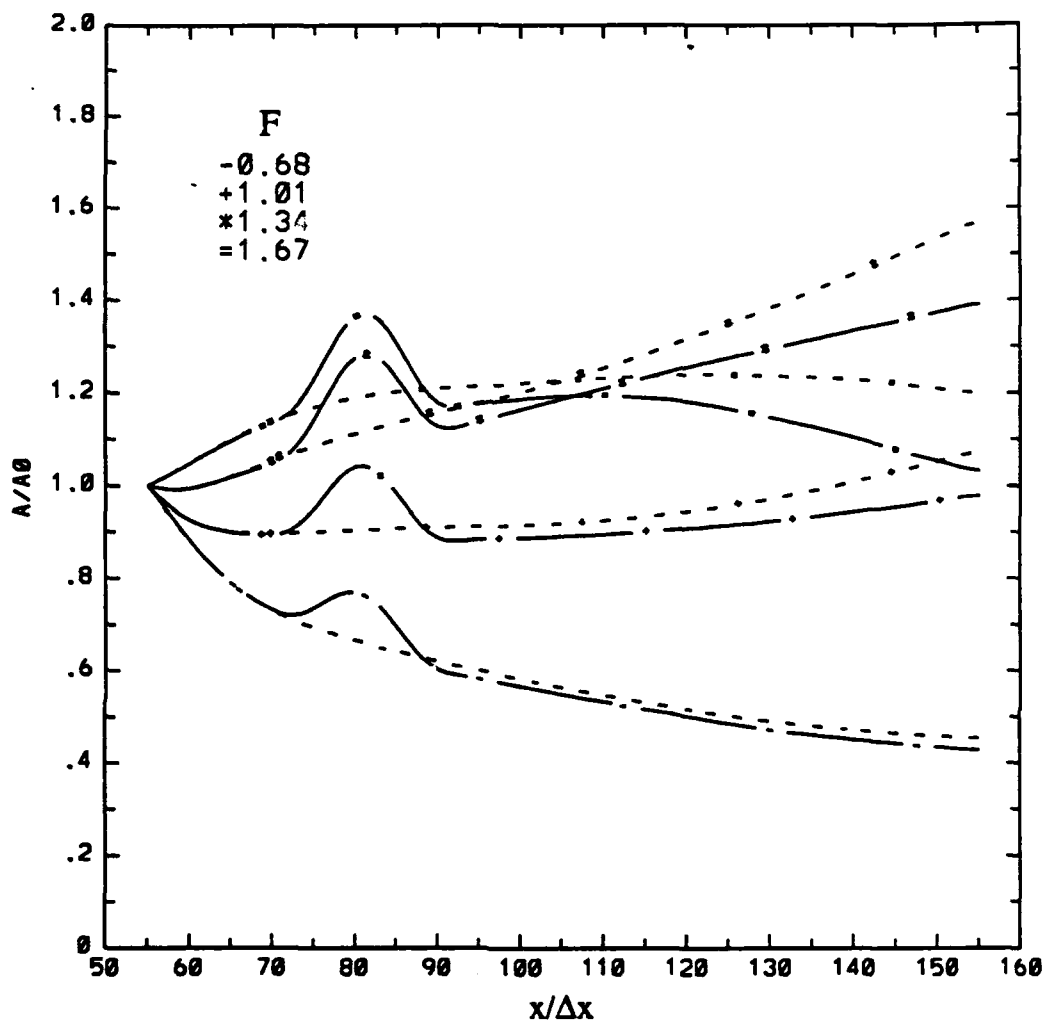


Fig. 15: Comparison of the streamwise amplification of four frequency components of the wave packet disturbance with a steady (passive) heater temperature between  $70 \leq x/\Delta x \leq 90$  (solid line) and without a heater strip (dashed line) for a) the wall vorticity, b) the wall normal velocity component  $y/\Delta y=10$ .

b)

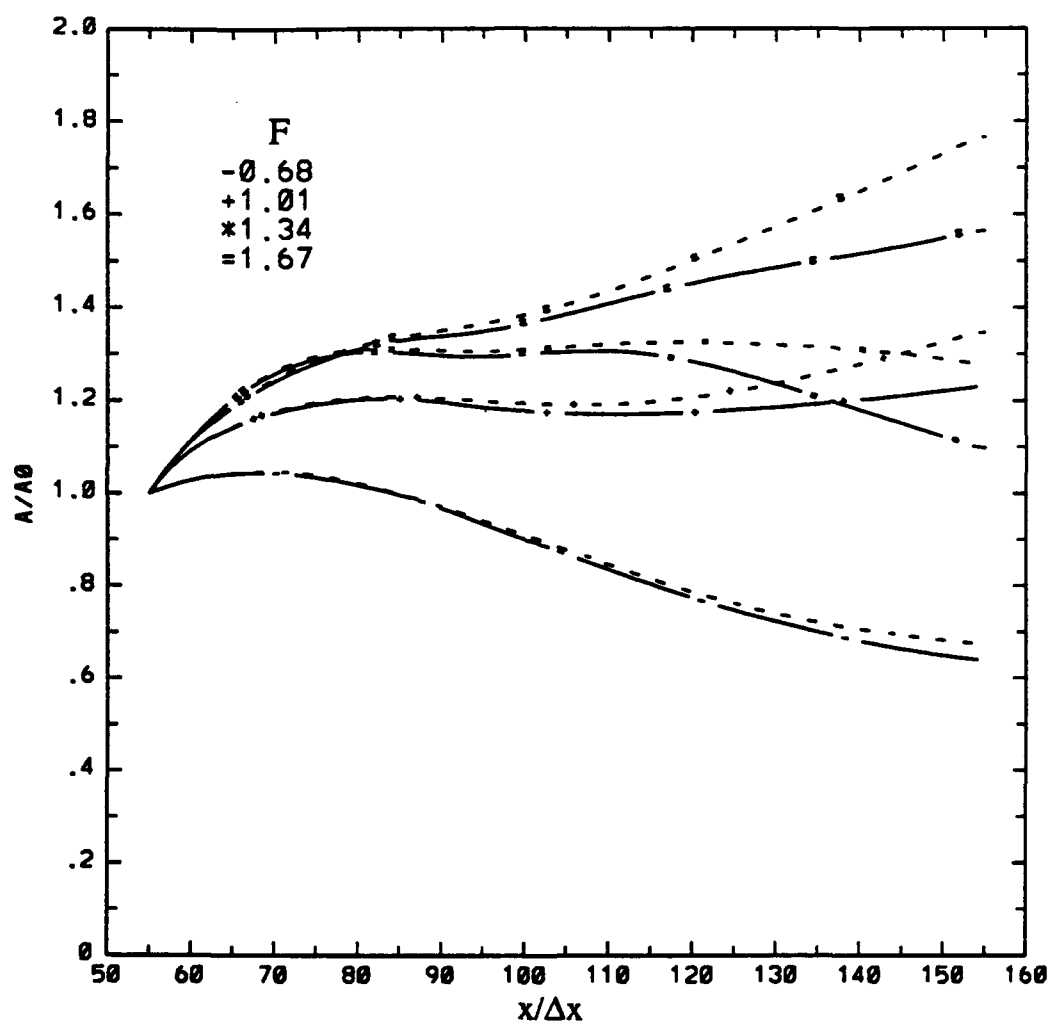


Fig. 15b: continued.

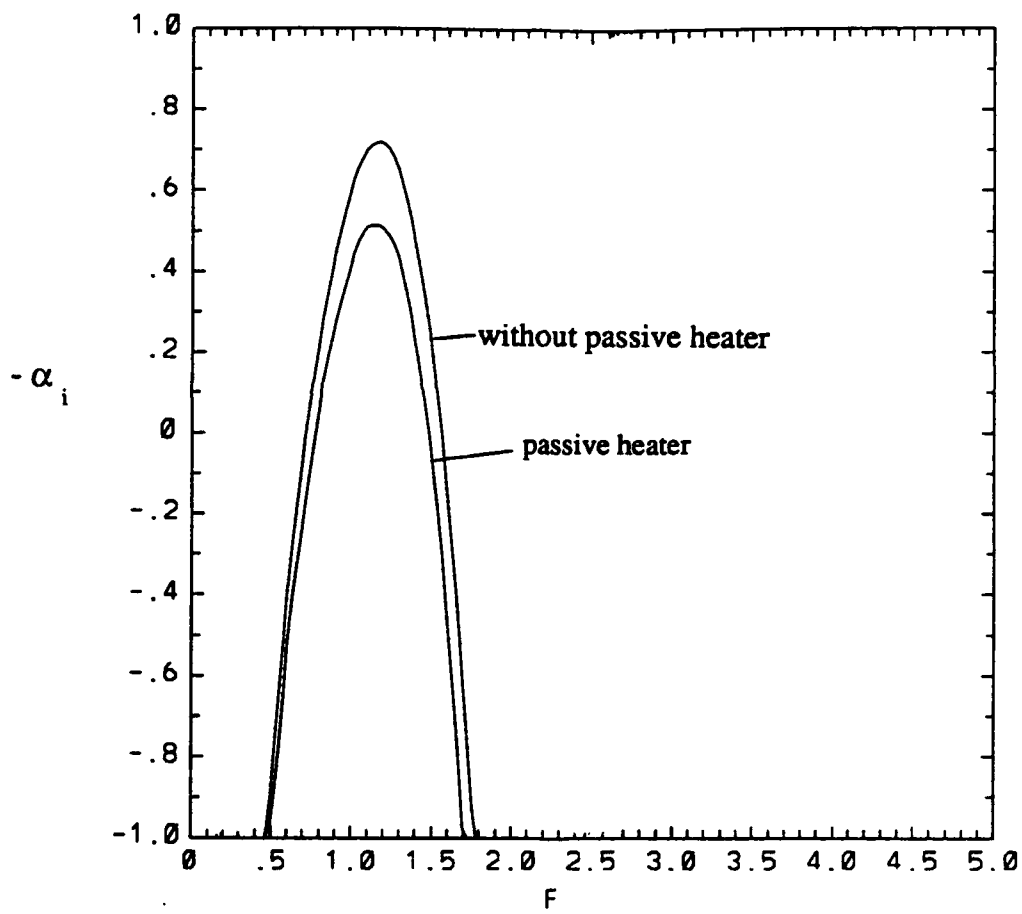


Fig. 16: Comparison of the rate of amplification  $-\alpha_i$  of the wall vorticity signal at  $x/\Delta x=140$  for the case with the passive heater (at  $70 \leq x/\Delta x \leq 90$ ) and without the passive heater present.

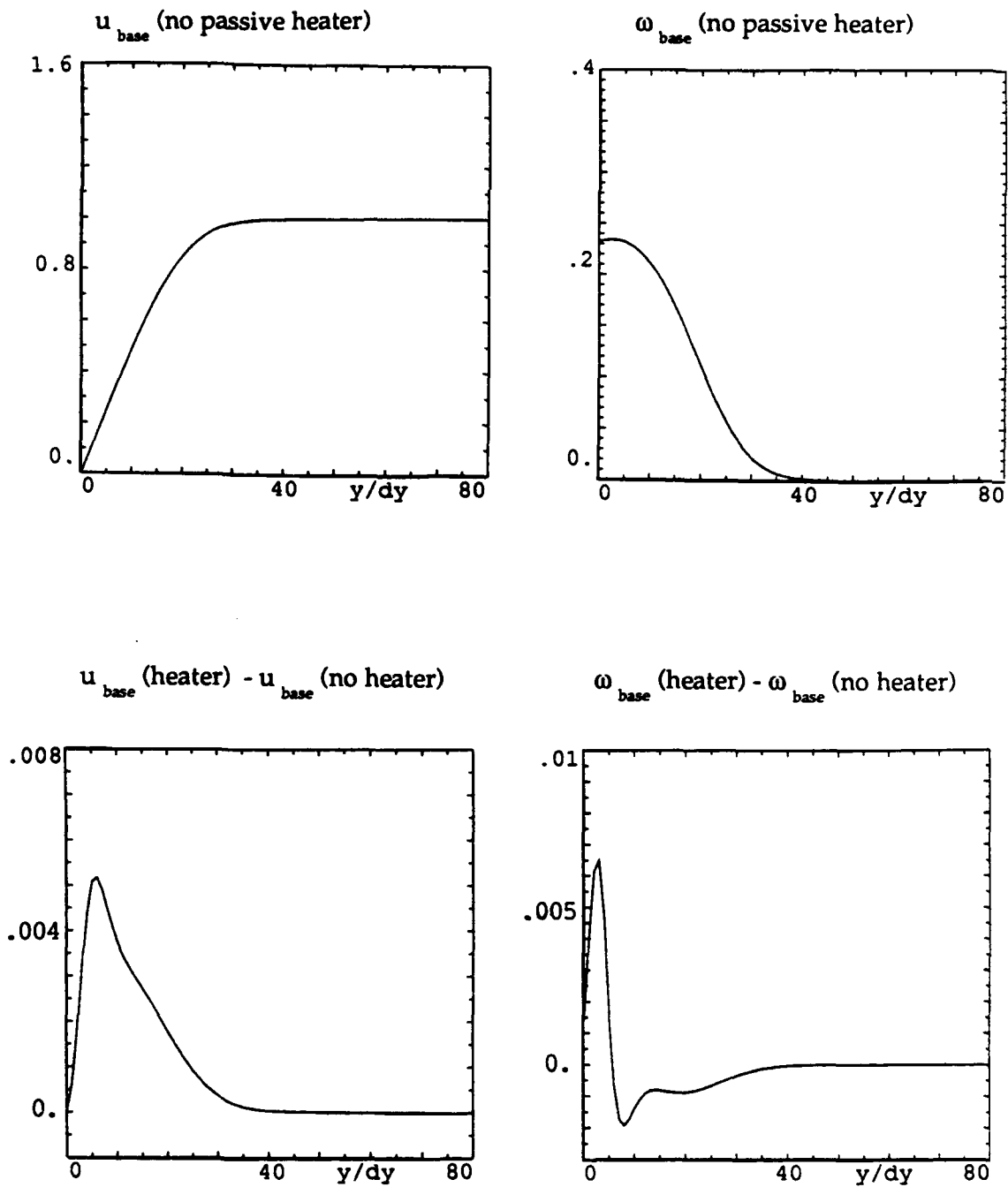


Fig. 17: Steady streamwise velocity  $u_{\text{base}}$  and vorticity  $\omega_{\text{base}}$  profiles at position  $x/\Delta x = 100$ ,  $Re_{\delta_1} = 772$  for the case without the passive heater and the difference of  $u_{\text{base}}$  and  $\omega_{\text{base}}$  for the case with the heater and the case without the passive heater.

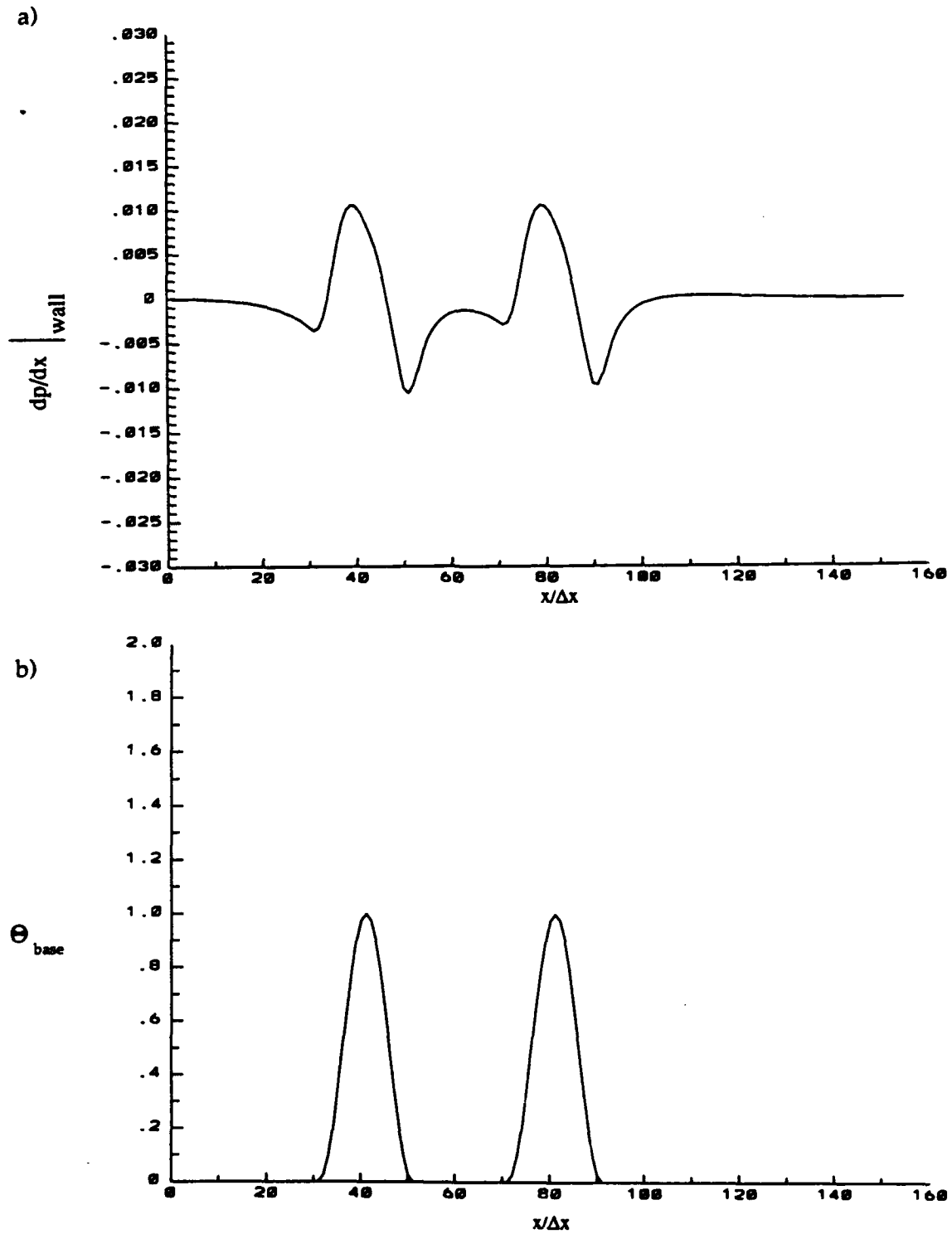


Fig. 18: The a) Steady pressure gradient in streamwise direction  $\frac{dp}{dx} = \nu \left( \frac{d^2 u}{dy^2} \right) - \left( \frac{dv}{d\theta} \right) \left( \frac{d\theta}{dy} \right) \left( \frac{du}{dy} \right)$  at the wall surface ( $y=0$ ) and b) the steady wall temperature for two heaters.

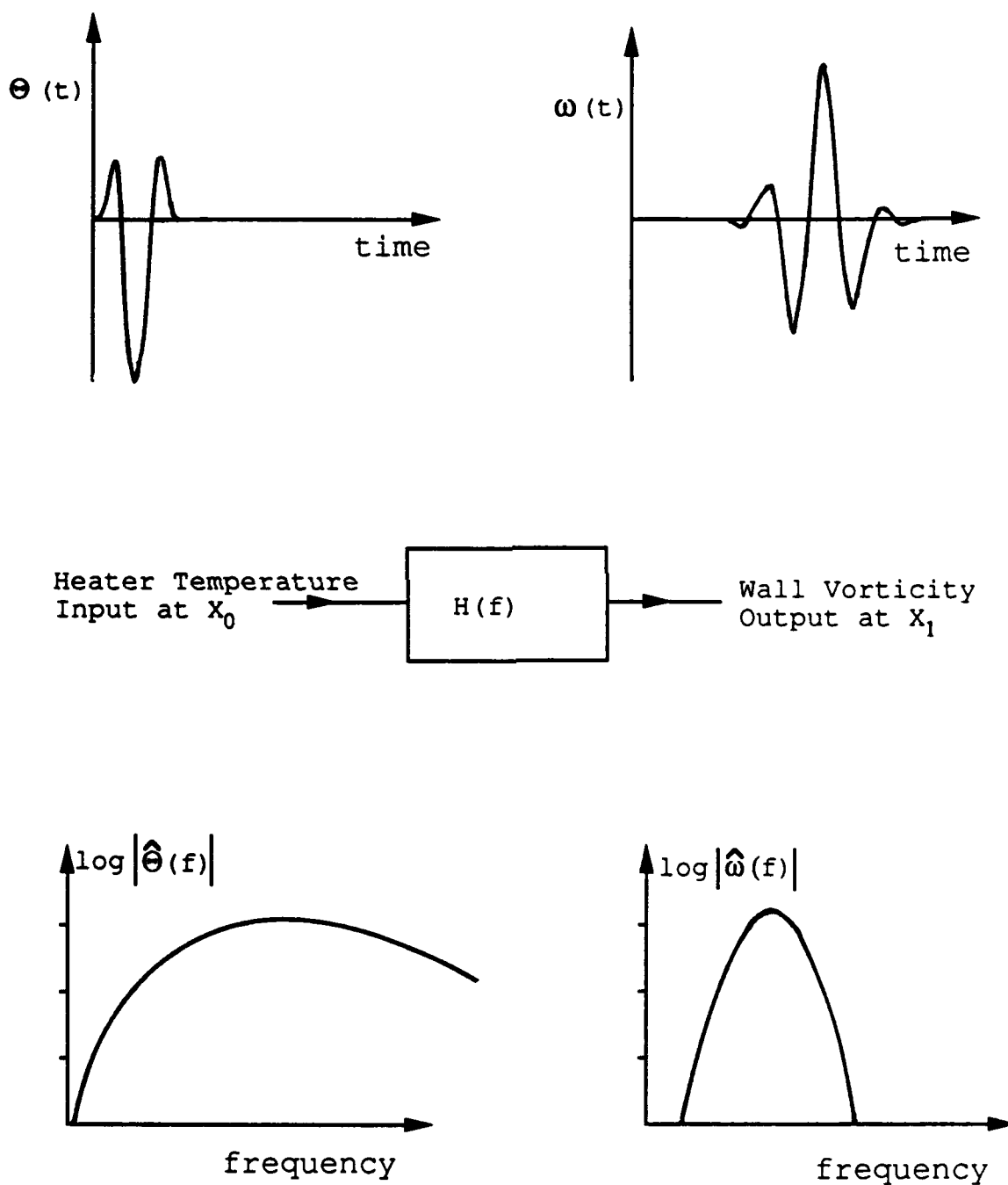


Fig. 19: Schematic representation of the transfer function technique relating the temperature input at location  $x_0$  to a wall vorticity response at  $x_1$ .

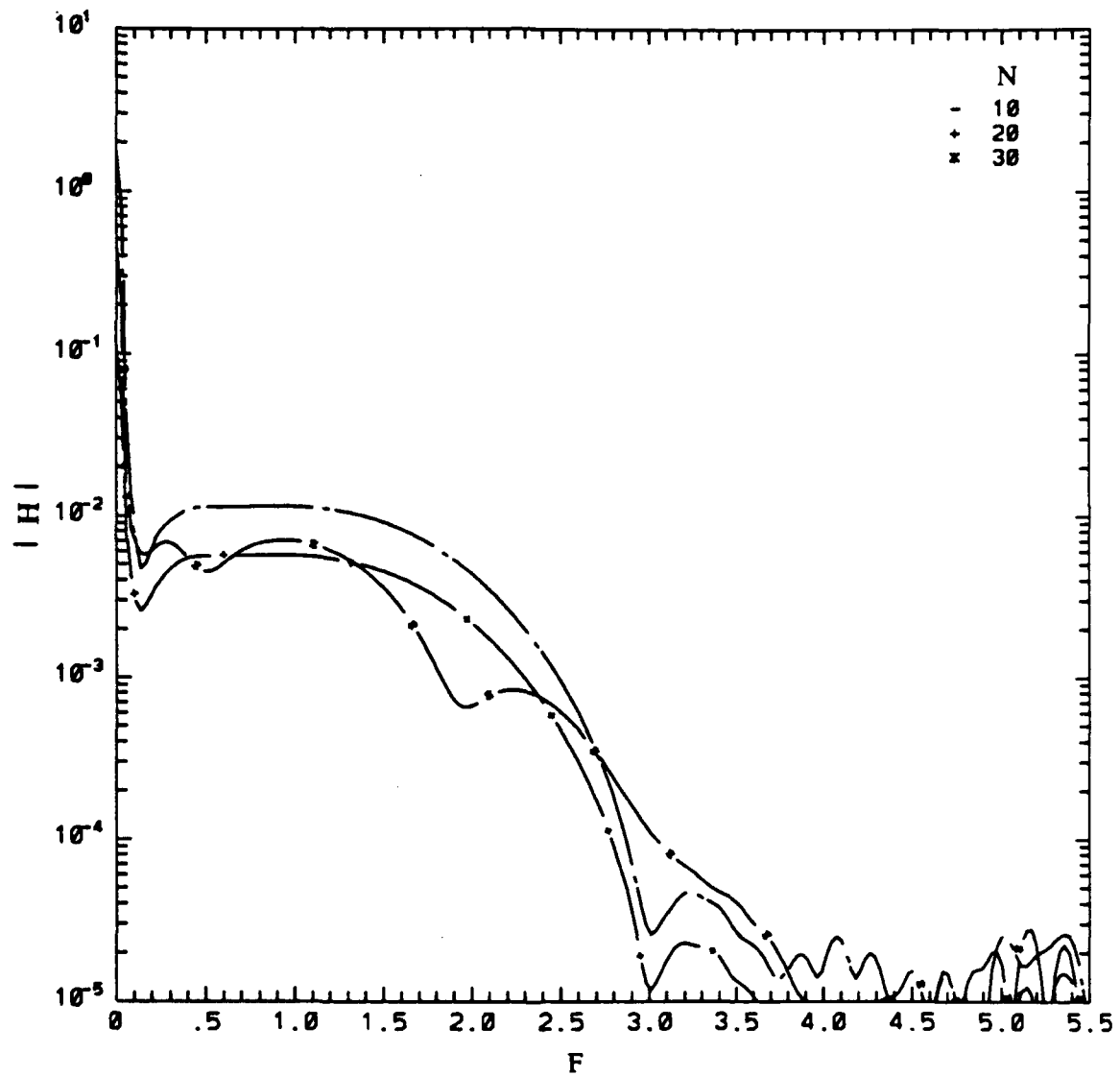


Fig. 20: Modulus of the transfer function at the streamwise position  $x/\Delta x = 70$  for three different heater strip lengths  $N = 10$  ( $30 \leq x/\Delta x \leq 40$ ),  $N = 20$  ( $30 \leq x/\Delta x \leq 50$ ) and  $N = 30$  ( $30 \leq x/\Delta x \leq 60$ ).

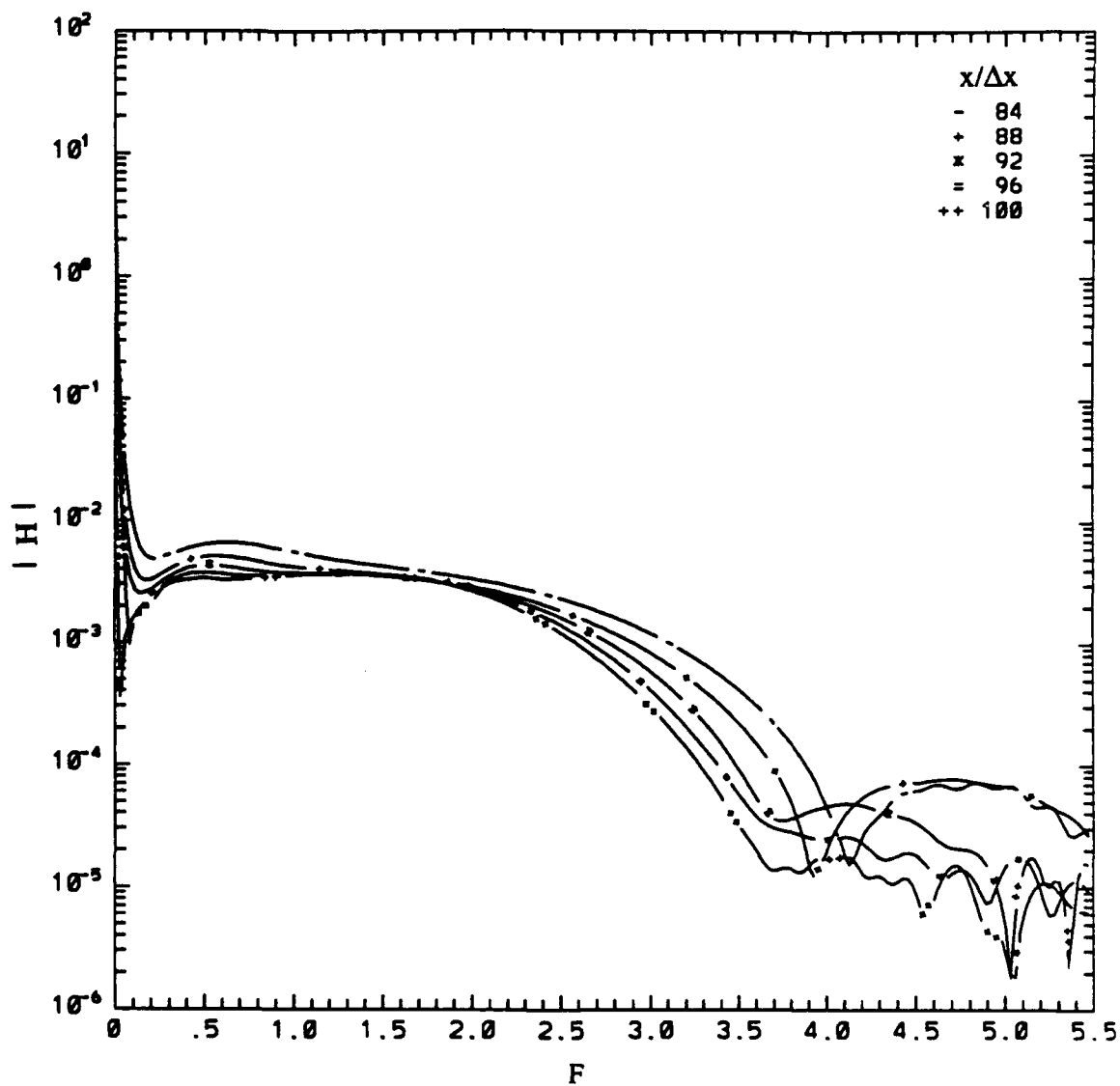


Fig. 21: Modulus of transfer function at several streamwise positions for the heater strip width  $70 \leq x/\Delta x \leq 80$ .

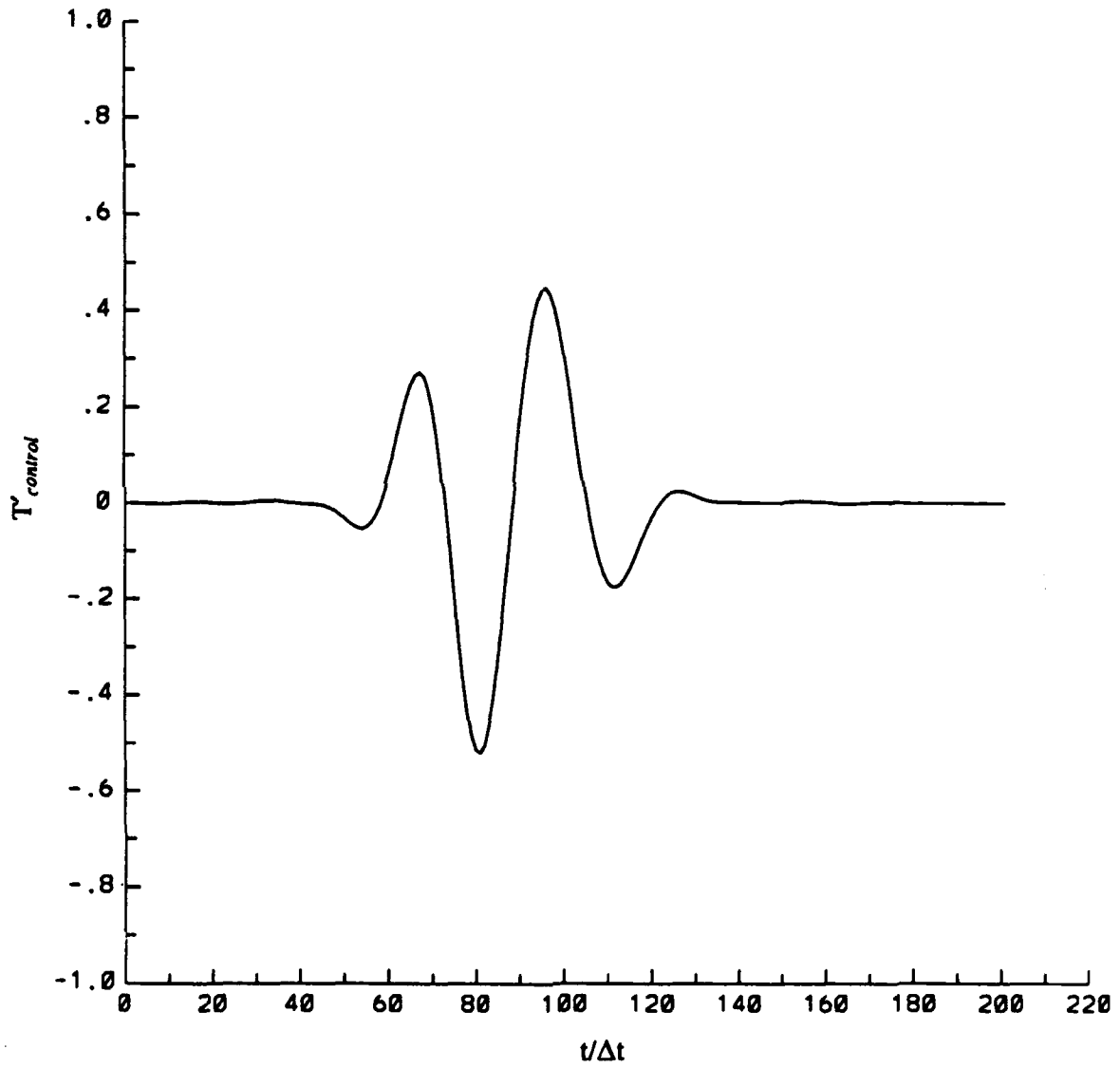


Fig. 22: Temperature control signal  $T_{control}$  for the controller strip.

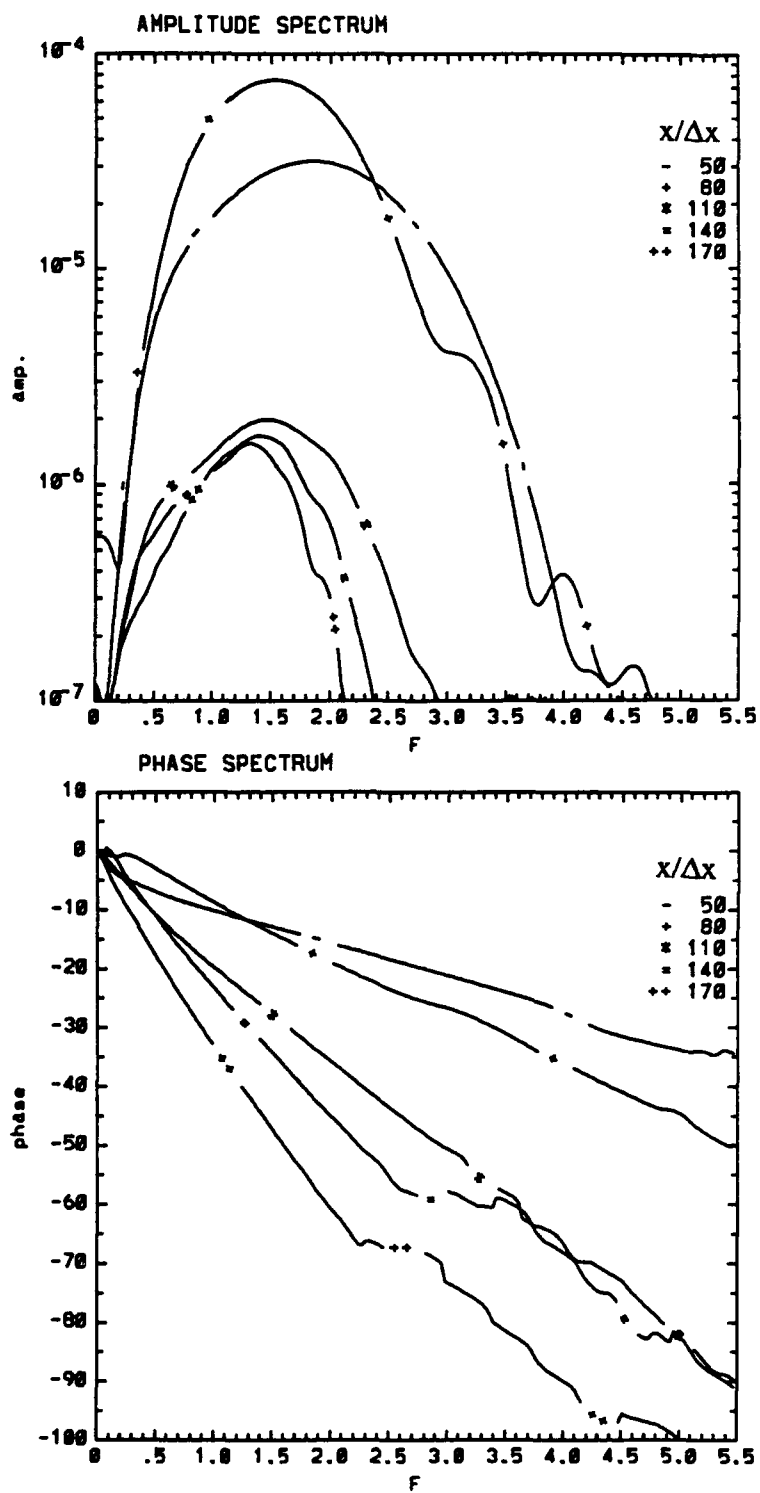


Fig. 23: Amplitude- and Phase- spectra of the wall vorticity signal at several streamwise positions, with control applied.

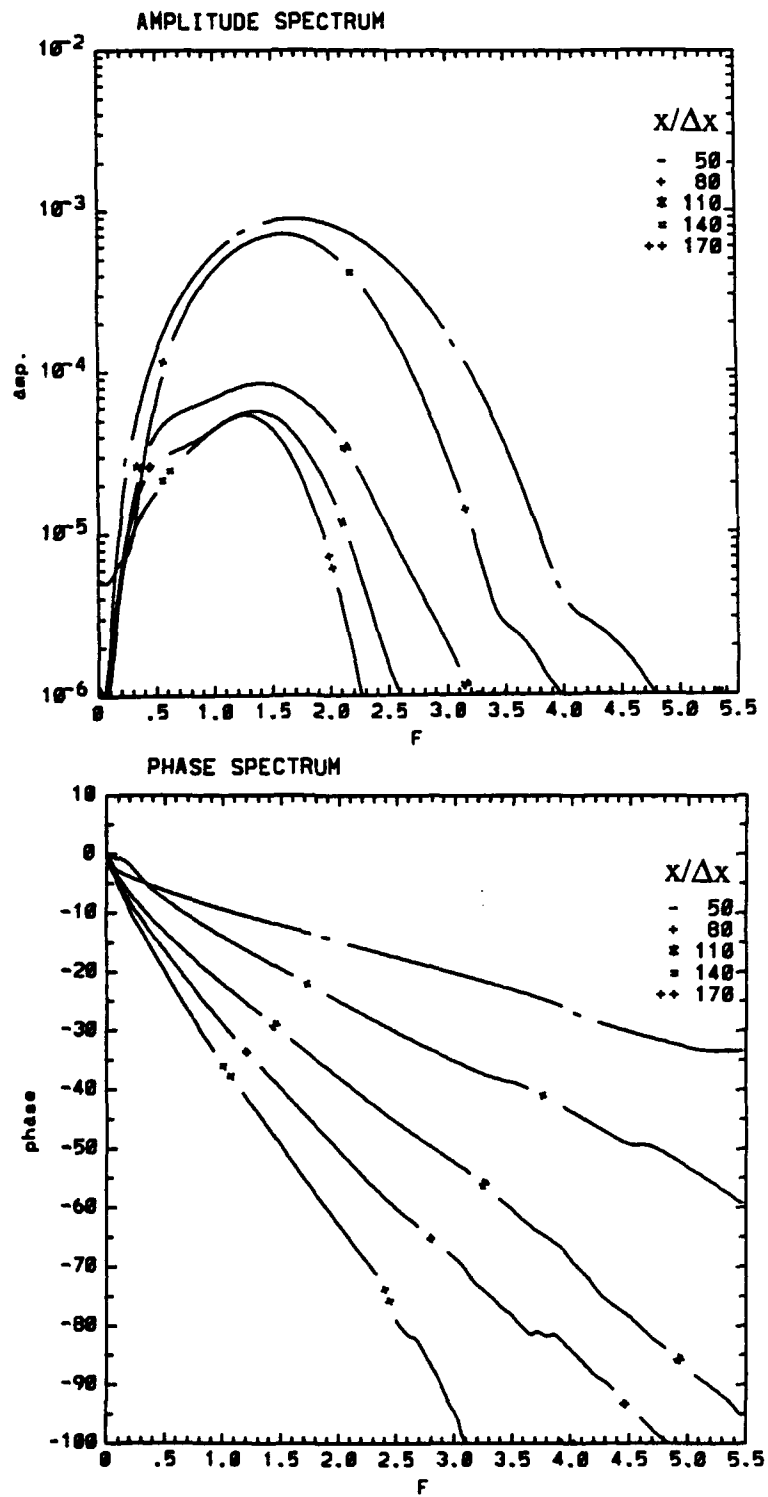


Fig. 24: Amplitude- and Phase-spectra of the wall normal velocity signal at  $y/\Delta y = 20$  at several streamwise positions, with control applied.

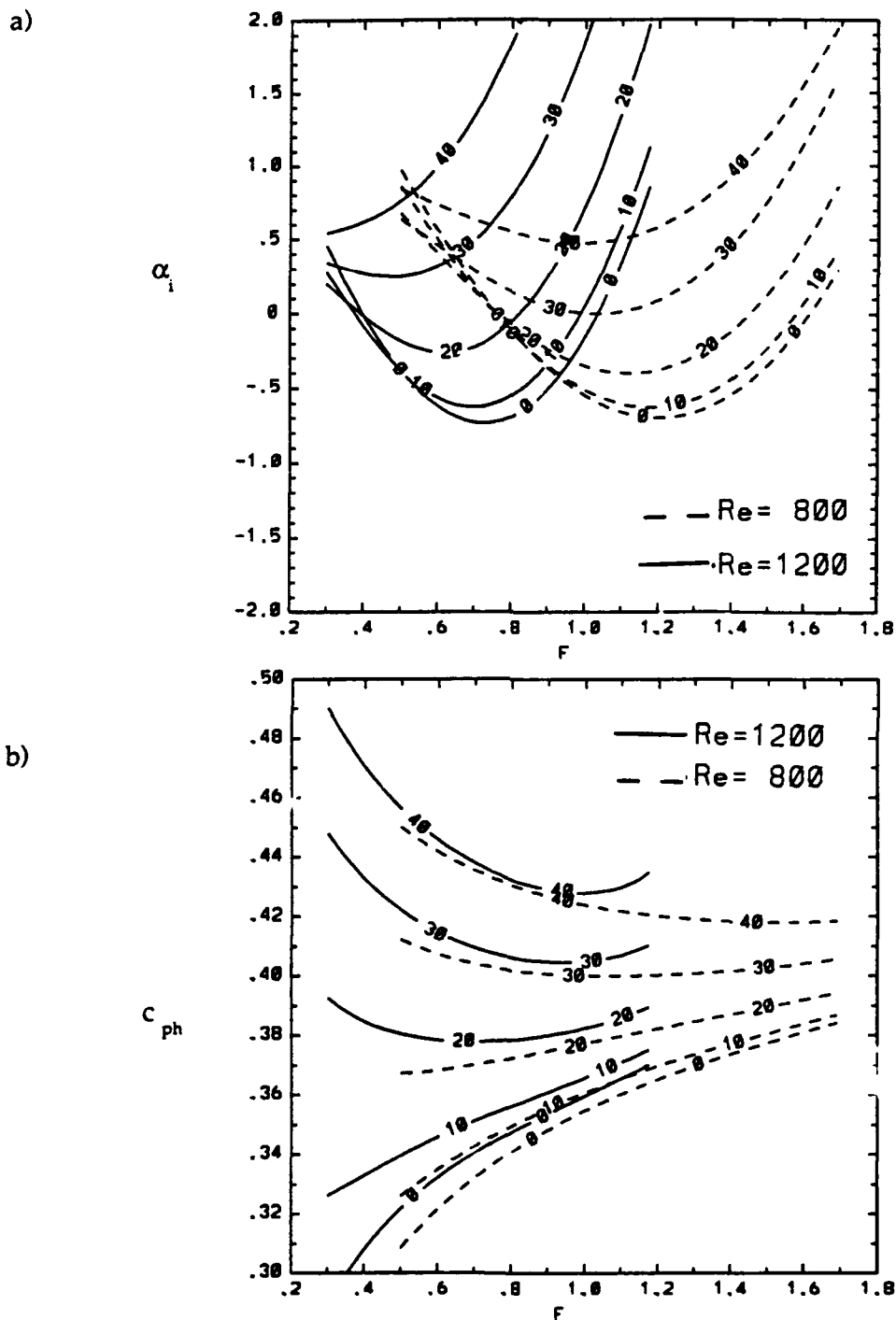


Fig. 25: The rate of amplification, the phase velocity and the ratio of the spanwise to streamwise wave number from the linear spatial stability theory at two streamwise positions  $Re_{\delta_1} = 800, 1200$ , for  $\gamma = 0$ , and four oblique modes  $\gamma = 10, 20, 30, 40$ .

c)

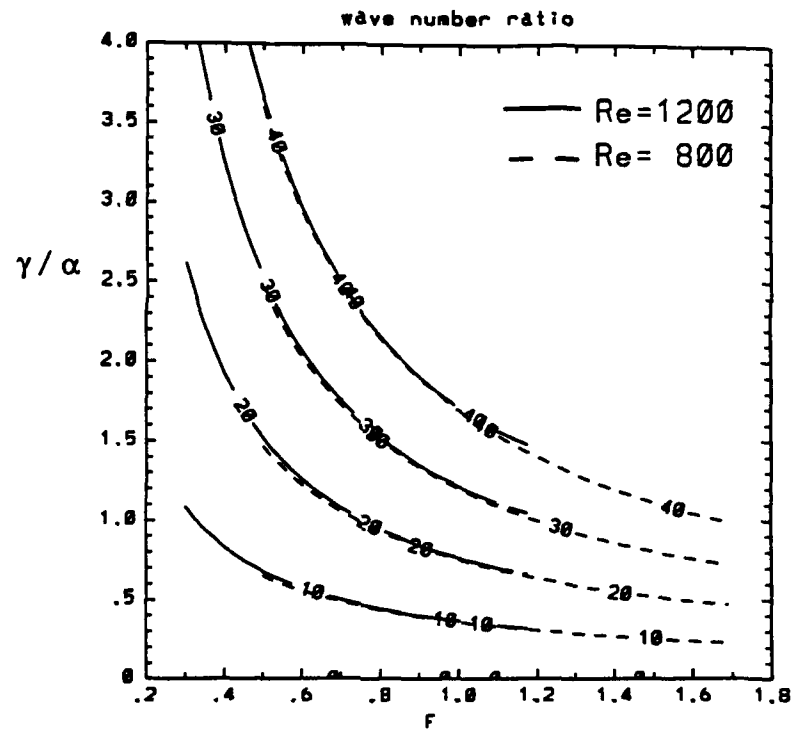


Fig. 25: continued.

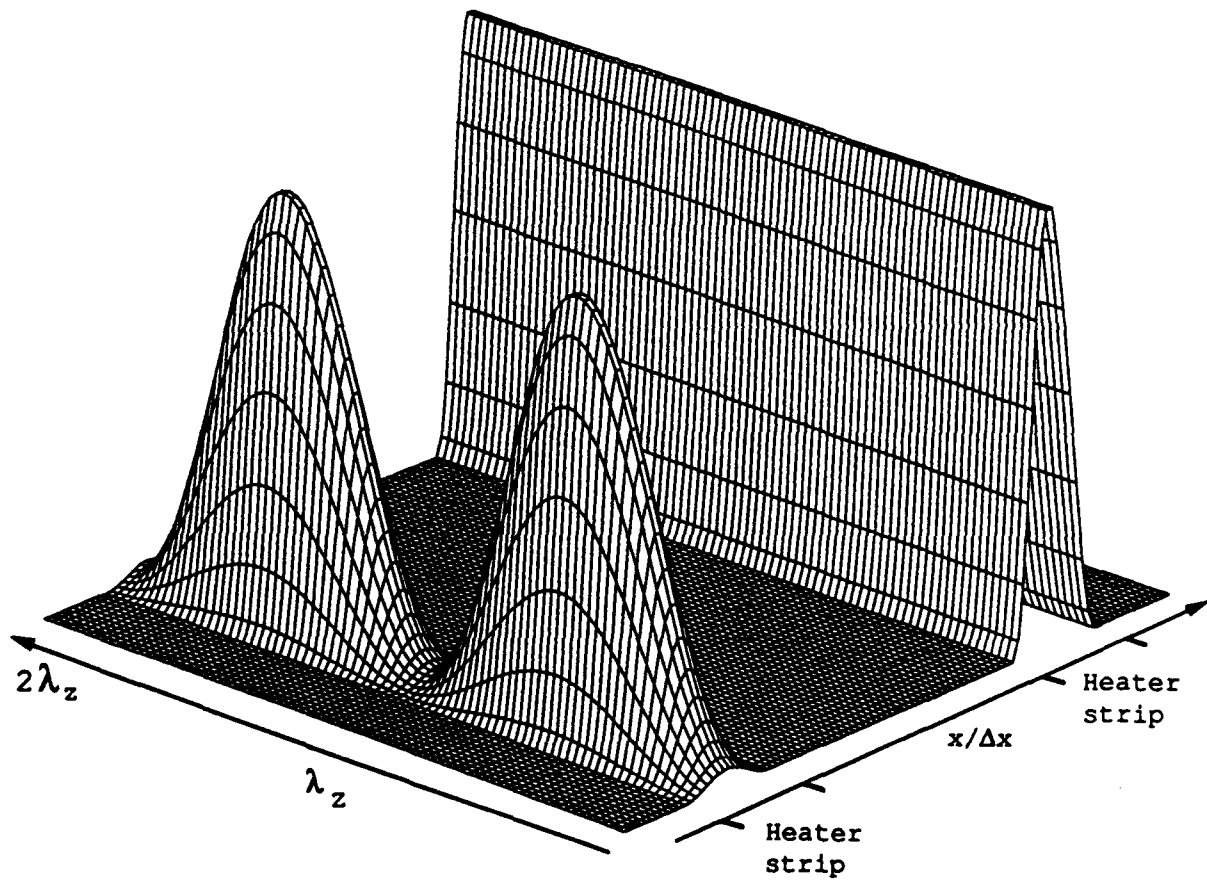


Fig. 26: Instantaneous wall temperature at  $t/\Delta t = 70$  with spanwise forcing of the first heater strip and a passive second heater.

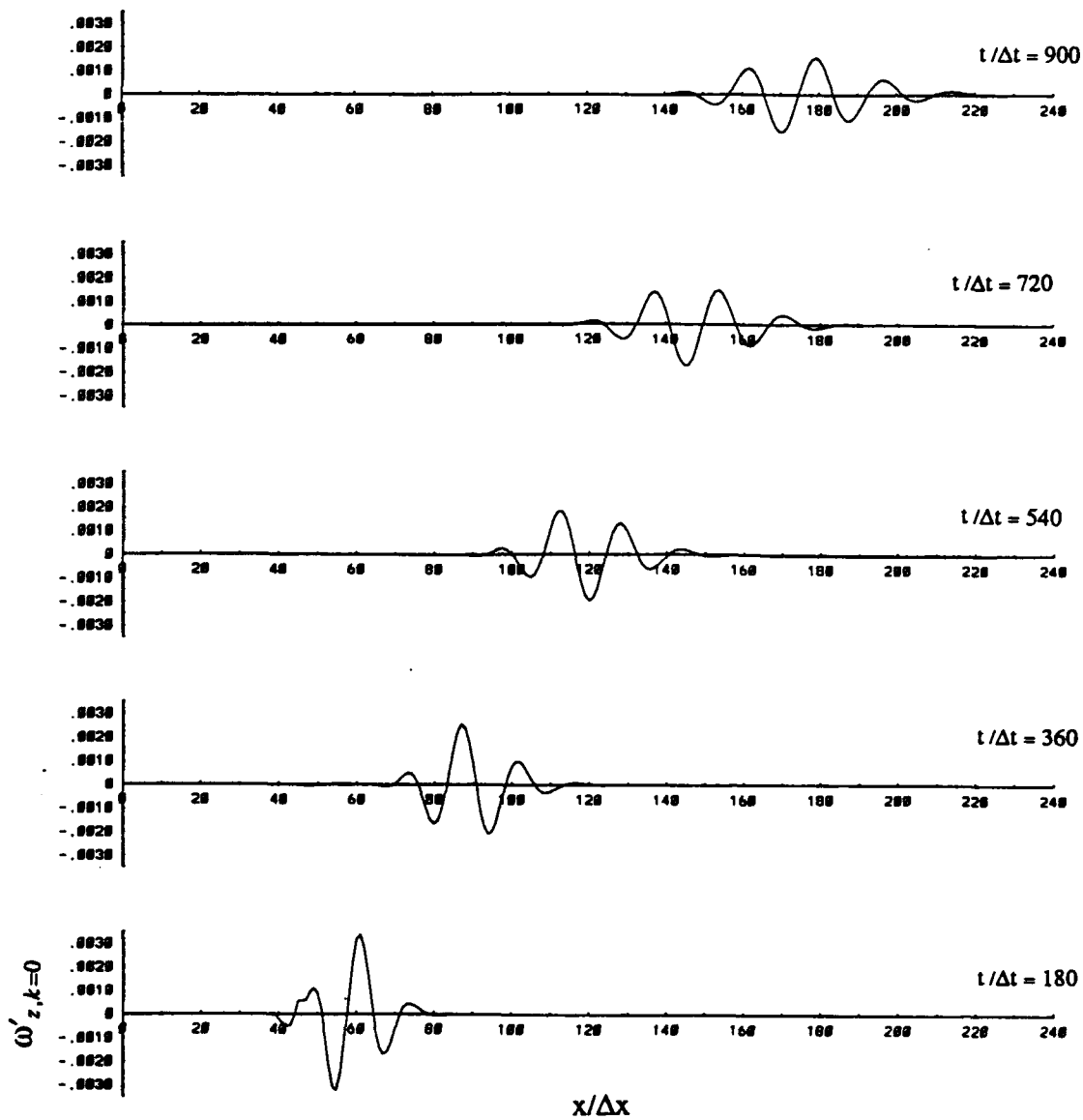


Fig. 27: Disturbance signal of the spanwise vorticity  $\omega'_{z,k=0}$  at several time levels for a) the two-dimensional mode, and b) the three-dimensional spanwise mode. End of forcing is at  $t/\Delta t = 120$ .

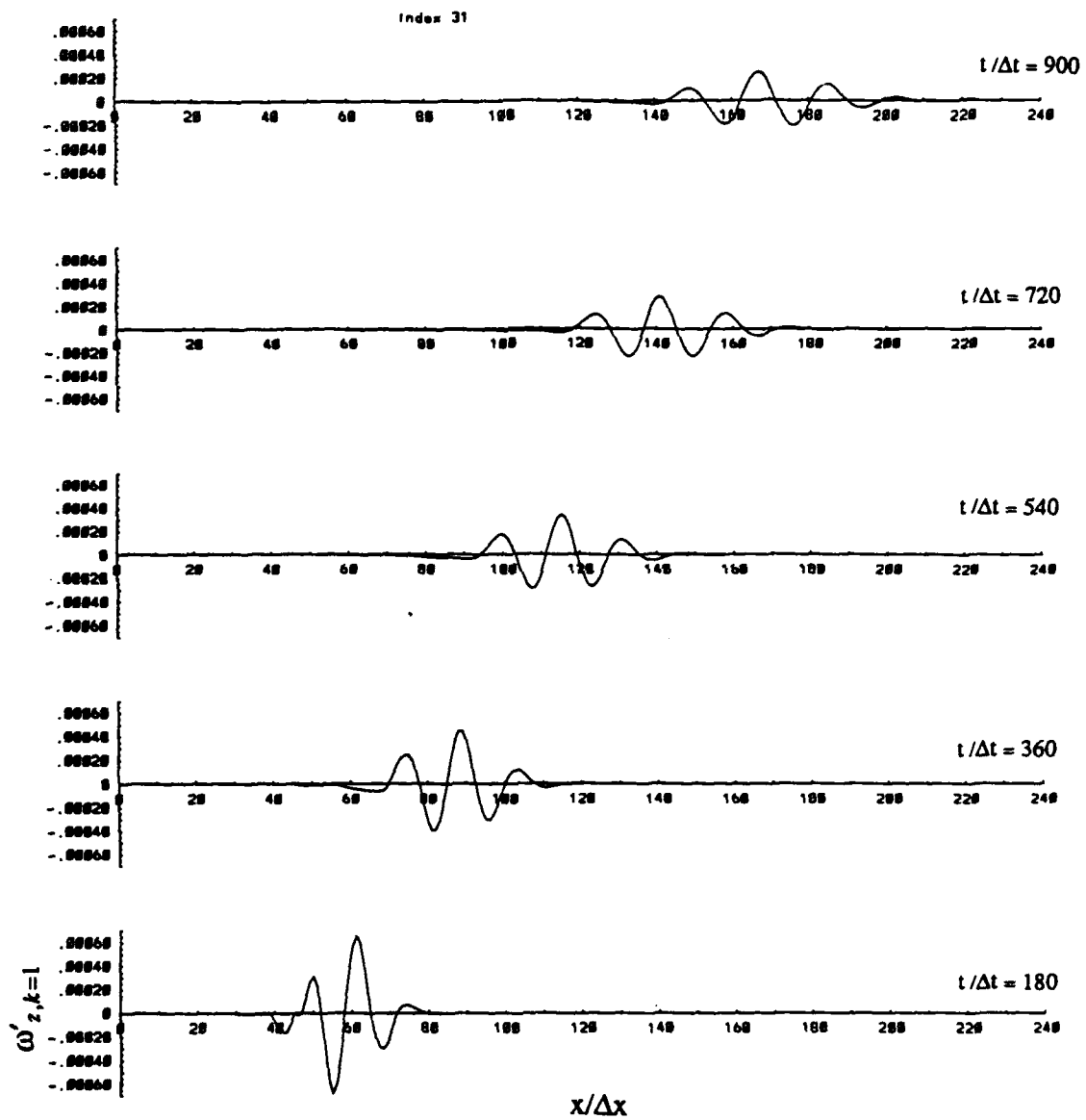


Fig. 27b: continued.

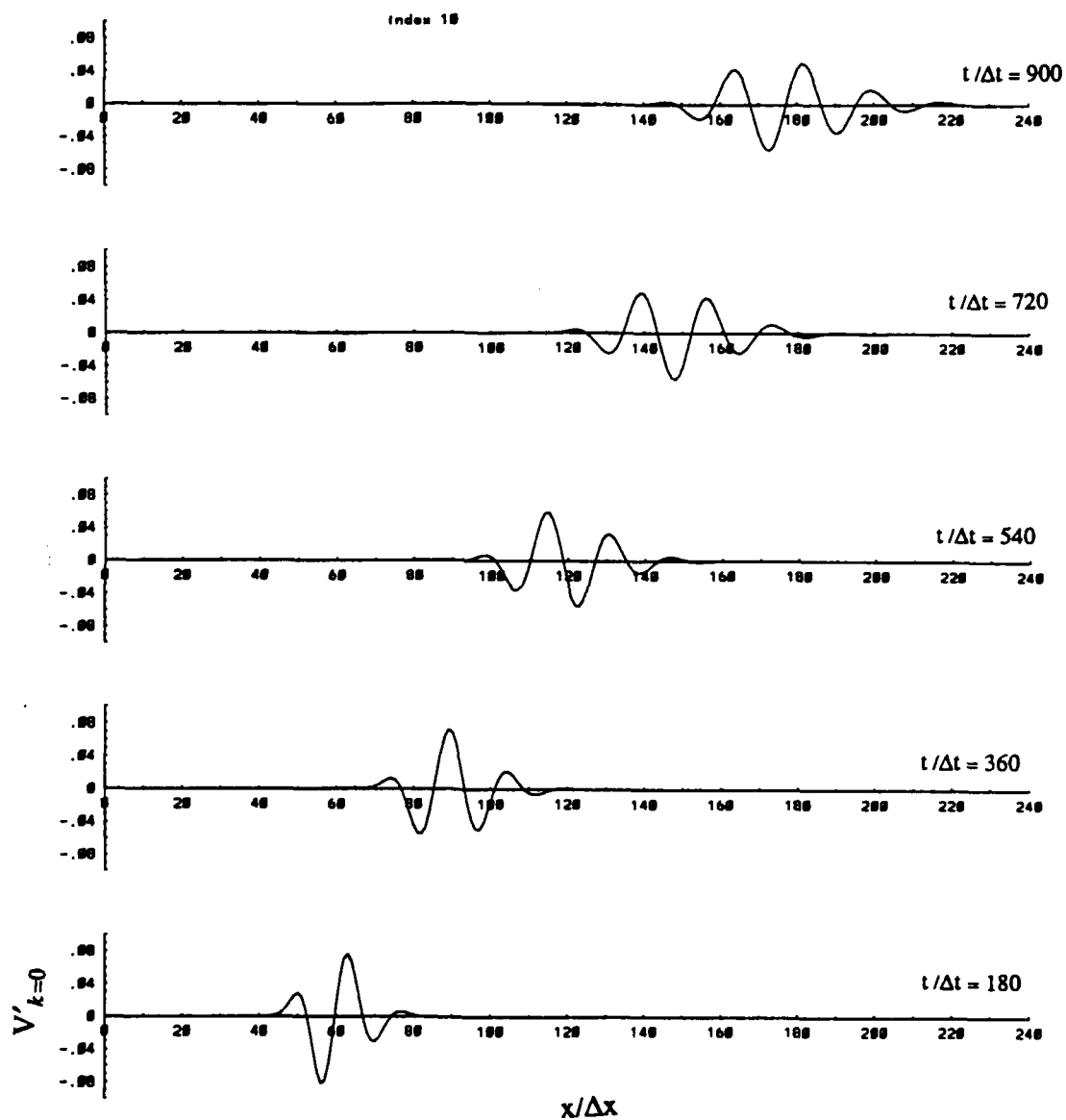


Fig. 28: Disturbance signal of the wall normal velocity  $v'_{k=0}$  at  $y/\Delta y = 40$  at several time levels for, a) the two-dimensional spanwise mode, and b) the three-dimensional spanwise mode. End of forcing is at  $t/\Delta t = 120$ .

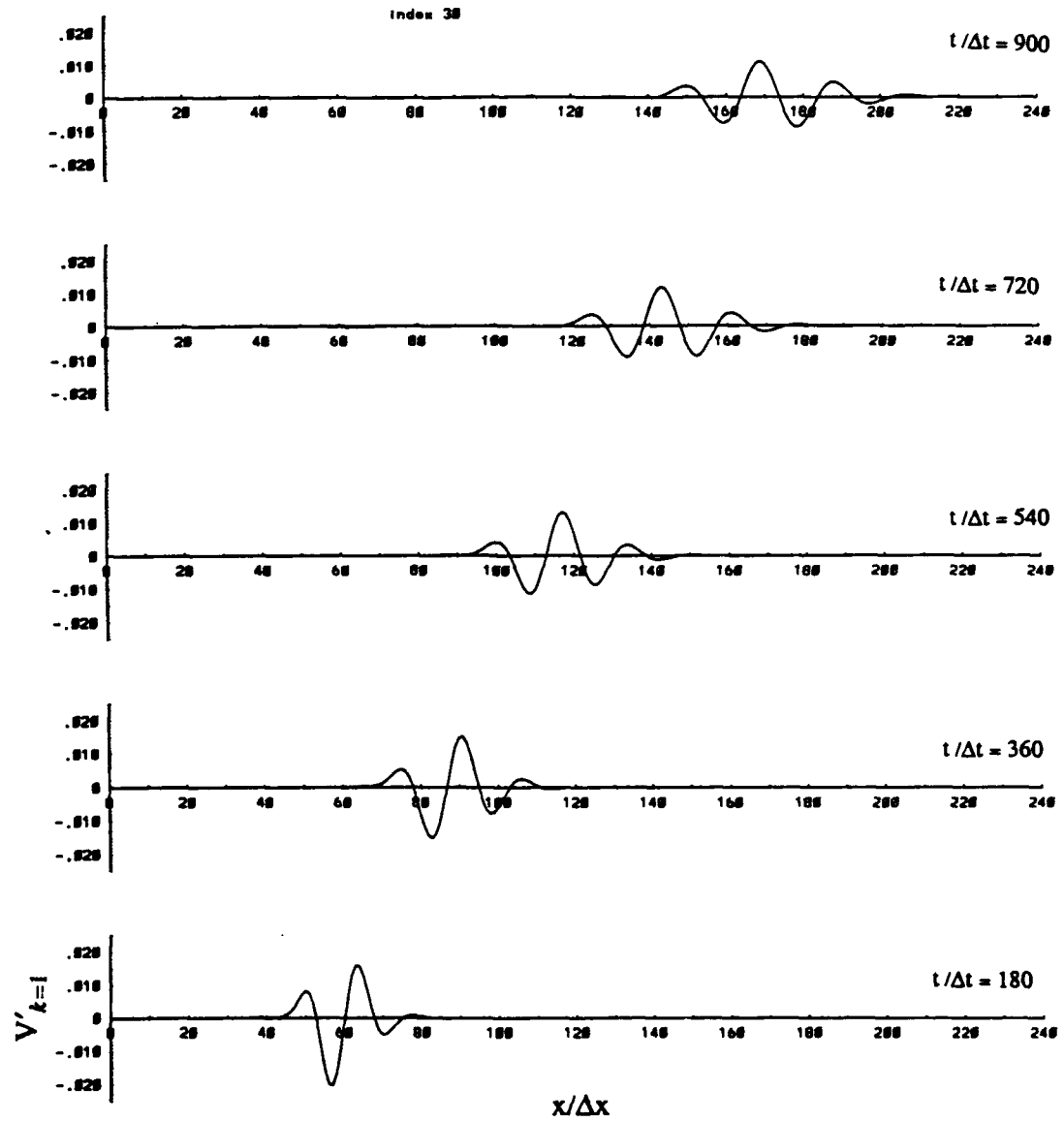


Fig. 28b: continued.

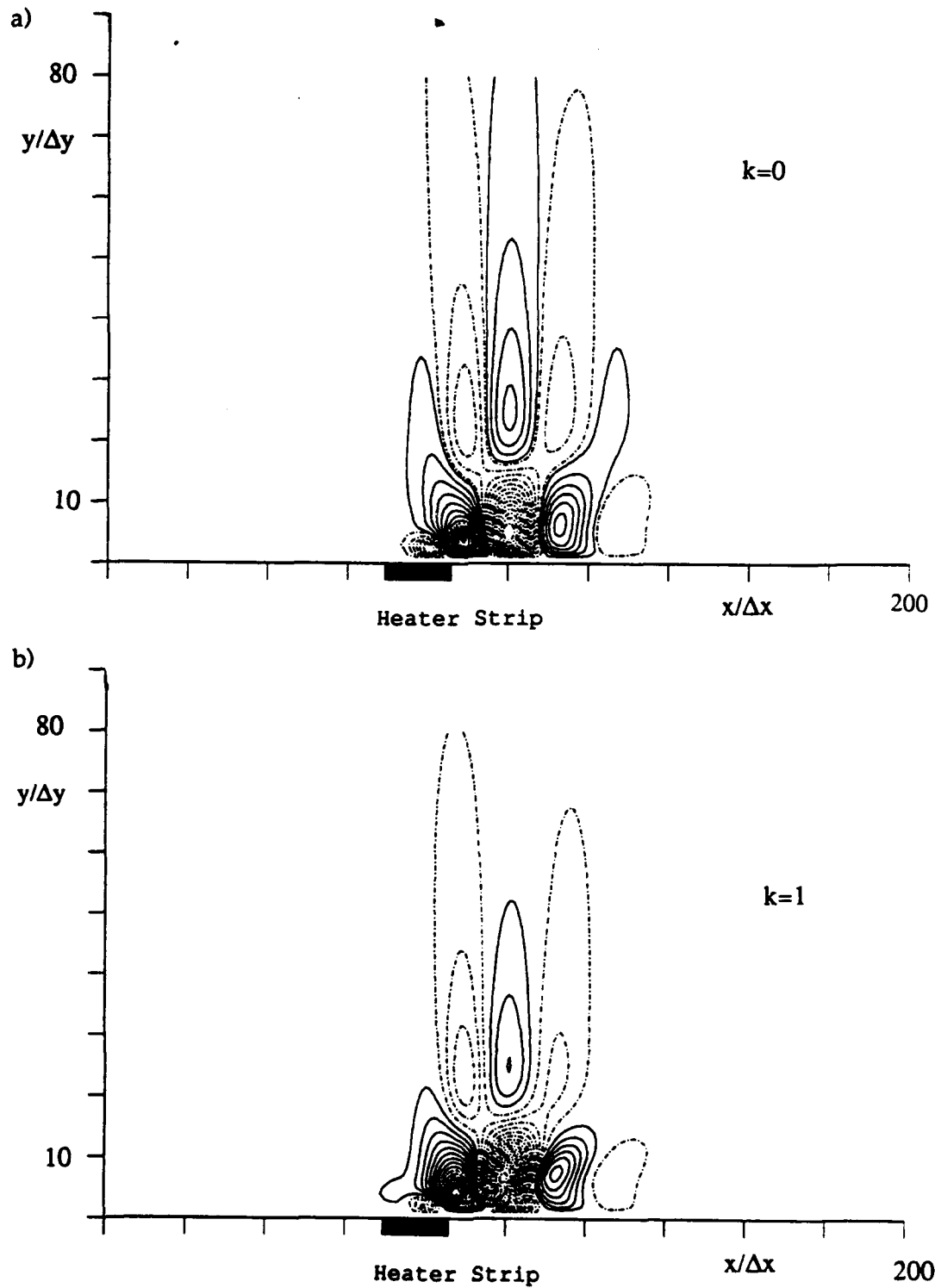


Fig. 29: Streamwise disturbance velocity component at  $t/\Delta t = 130$  for a) the two-dimensional mode  $u'_{k=0}$  and b) the three-dimensional spanwise mode  $u'_{k=1}$  with no control applied.

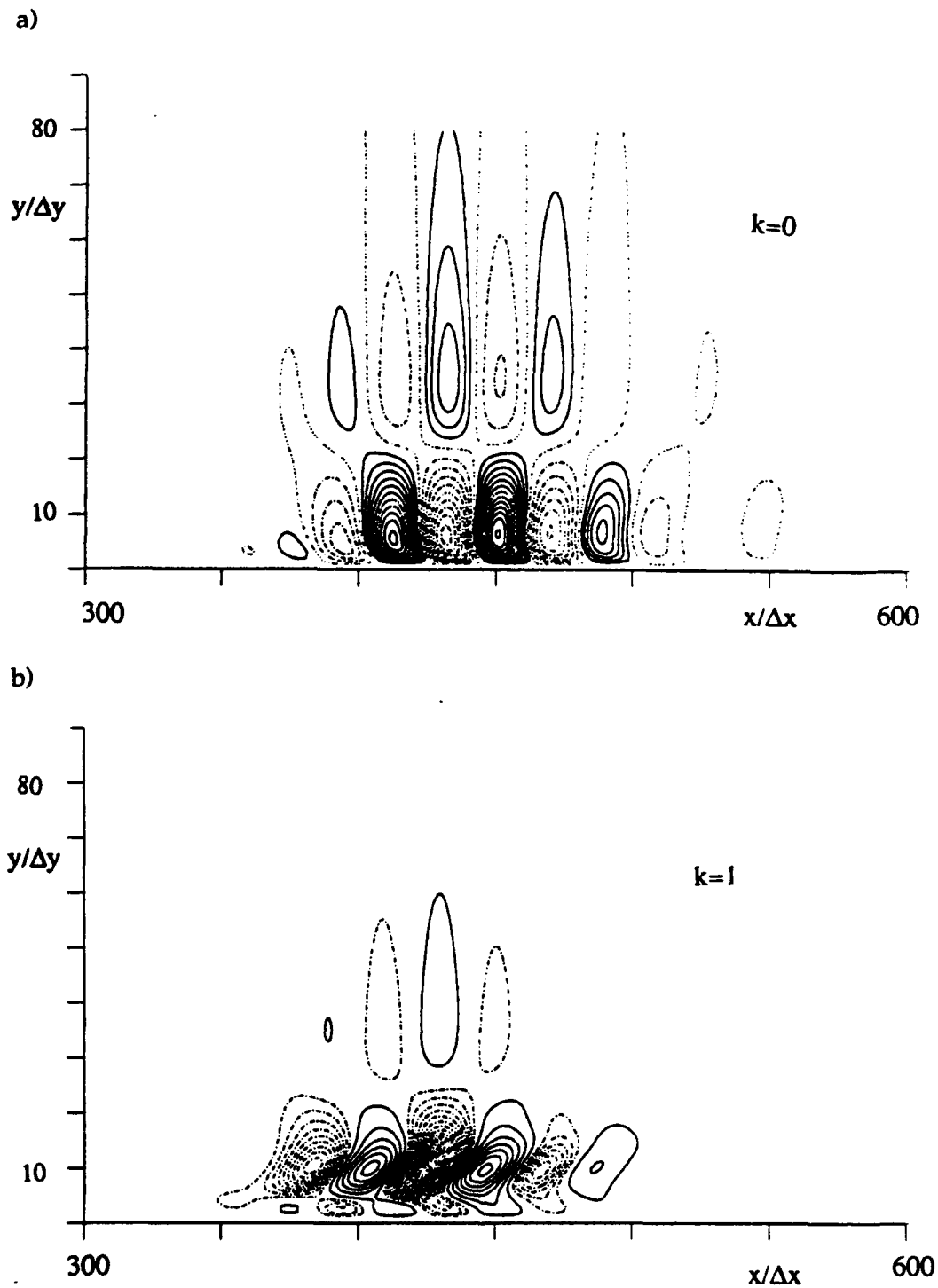


Fig. 30: Streamwise disturbance velocity component at  $t/\Delta t = 1200$ , for a) the two-dimensional mode  $u'_{k=0}$  and b) the three-dimensional spanwise mode  $u'_{k=1}$  with no control applied.

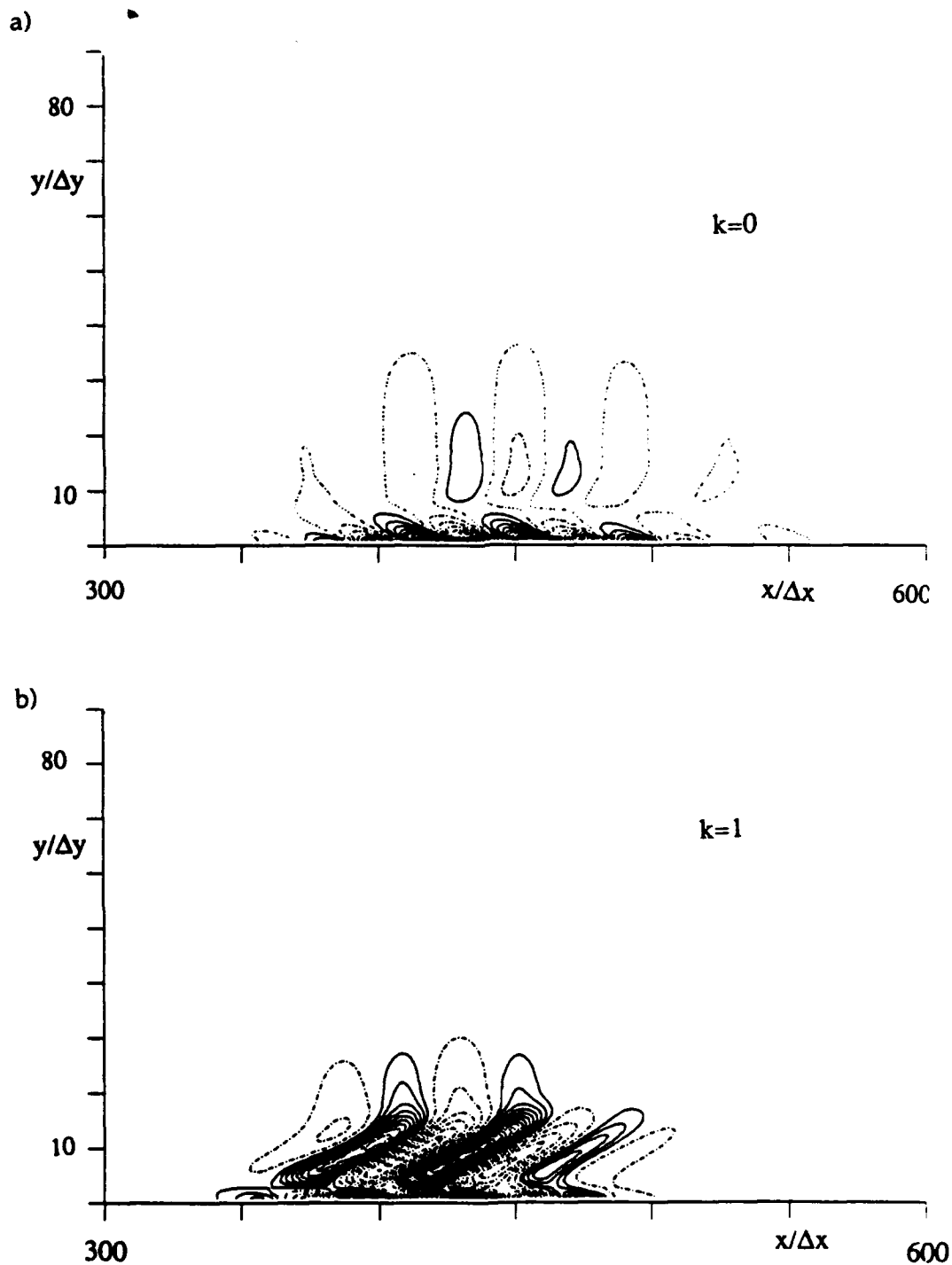


Fig. 31: Spanwise vorticity disturbance at  $t/\Delta t = 1200$  for a) the two-dimensional mode  $\omega_{z, k=0}$  and b) the three-dimensional spanwise mode  $\omega_{z, k=1}$  with no control applied.

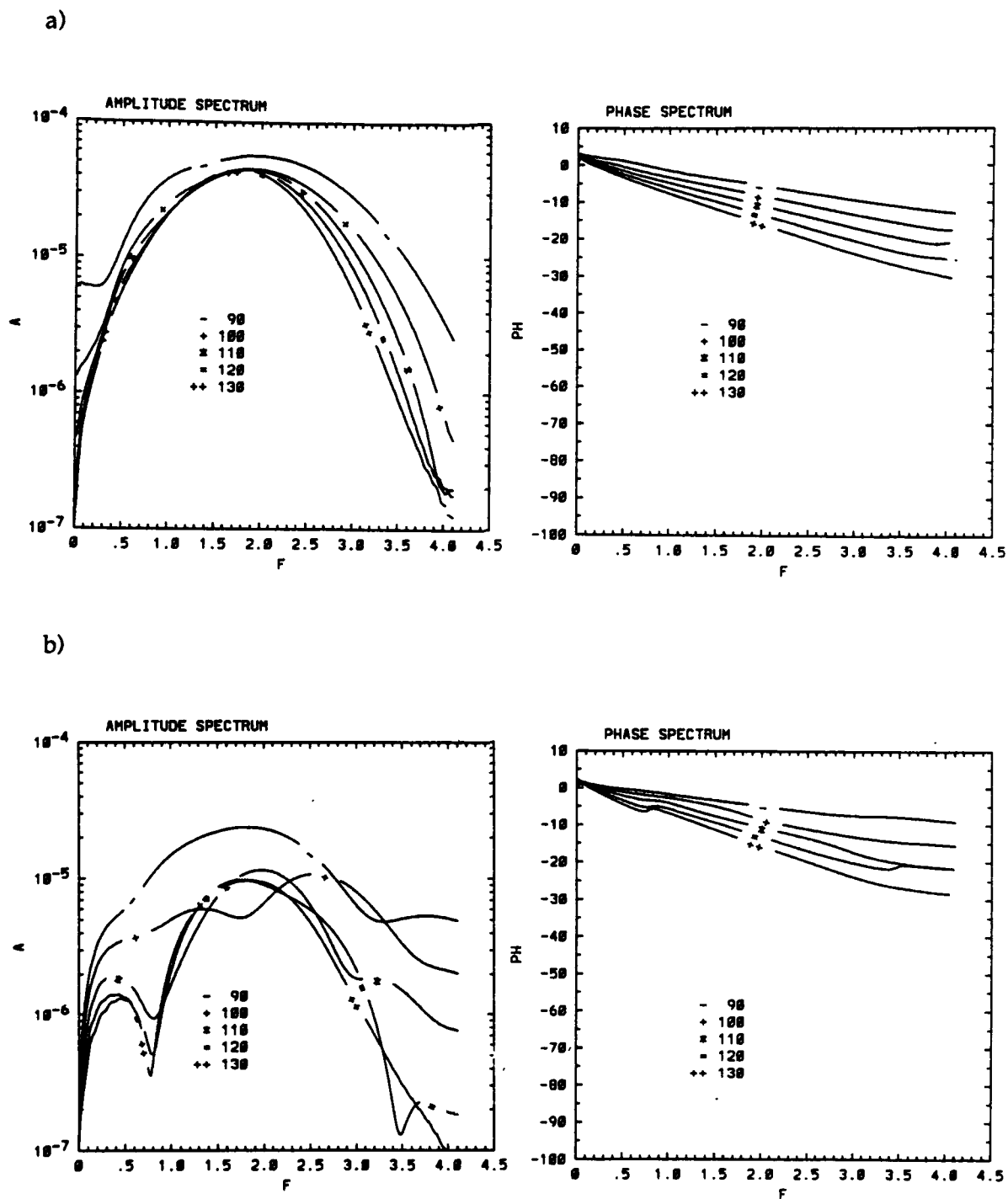


Fig. 32: Amplitude- and Phase- spectra of the spanwise wall vorticity signal for a) the two-dimensional mode  $\omega'_{z k=0}$  and for b) the three-dimensional mode  $\omega'_{z k=1}$  with no control applied, at  $x/\Delta x = 90, 100, 110, 120, 130$ .

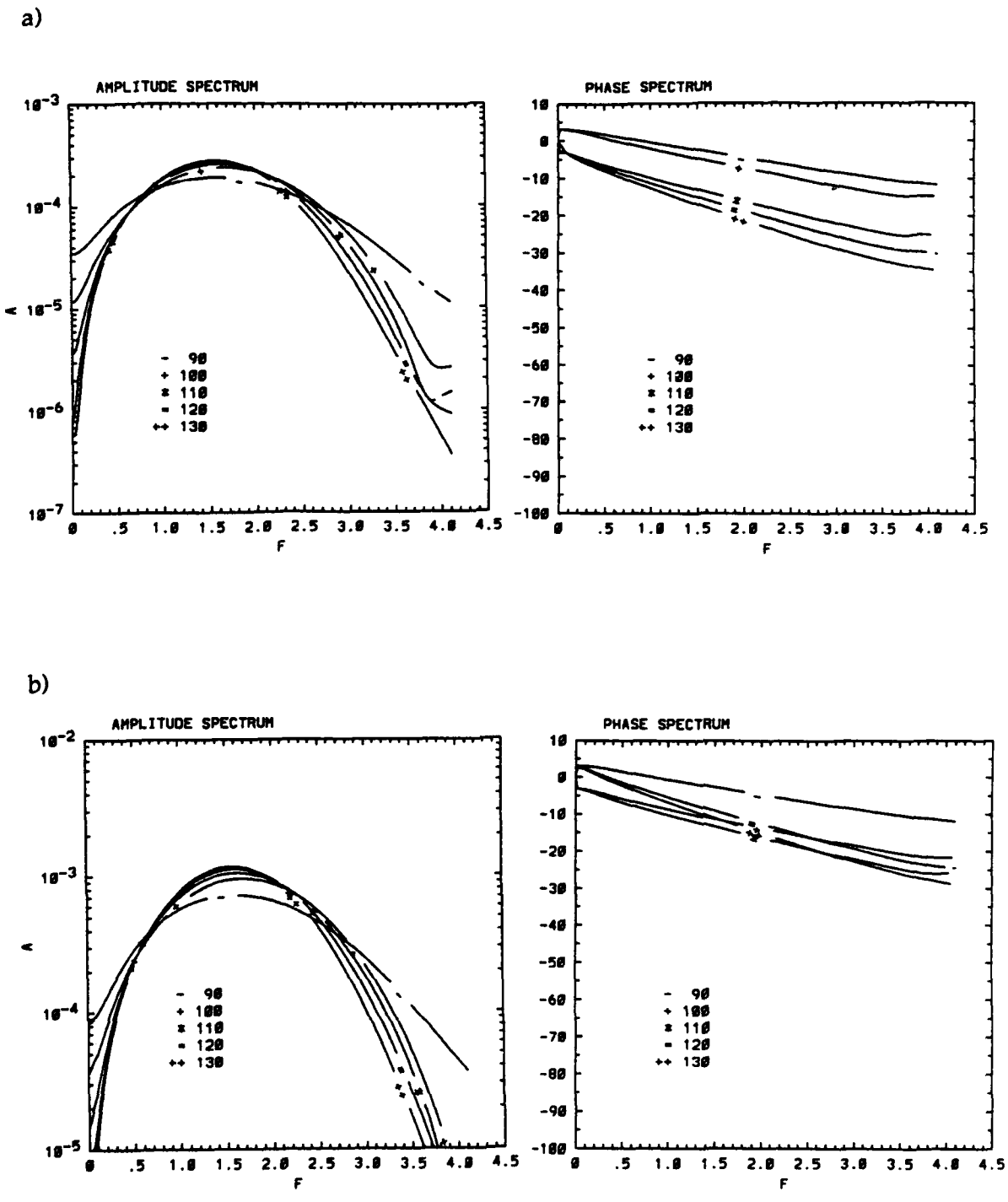


Fig. 33: Amplitude- and Phase- spectra of the wall normal velocity signal at  $y/\Delta y=40$  for a) the two-dimensional mode  $v'_{k=0}$  and for b) the three-dimensional mode  $v'_{k=1}$  with no control applied, at  $x/\Delta x = 90, 100, 110, 120, 130$ .

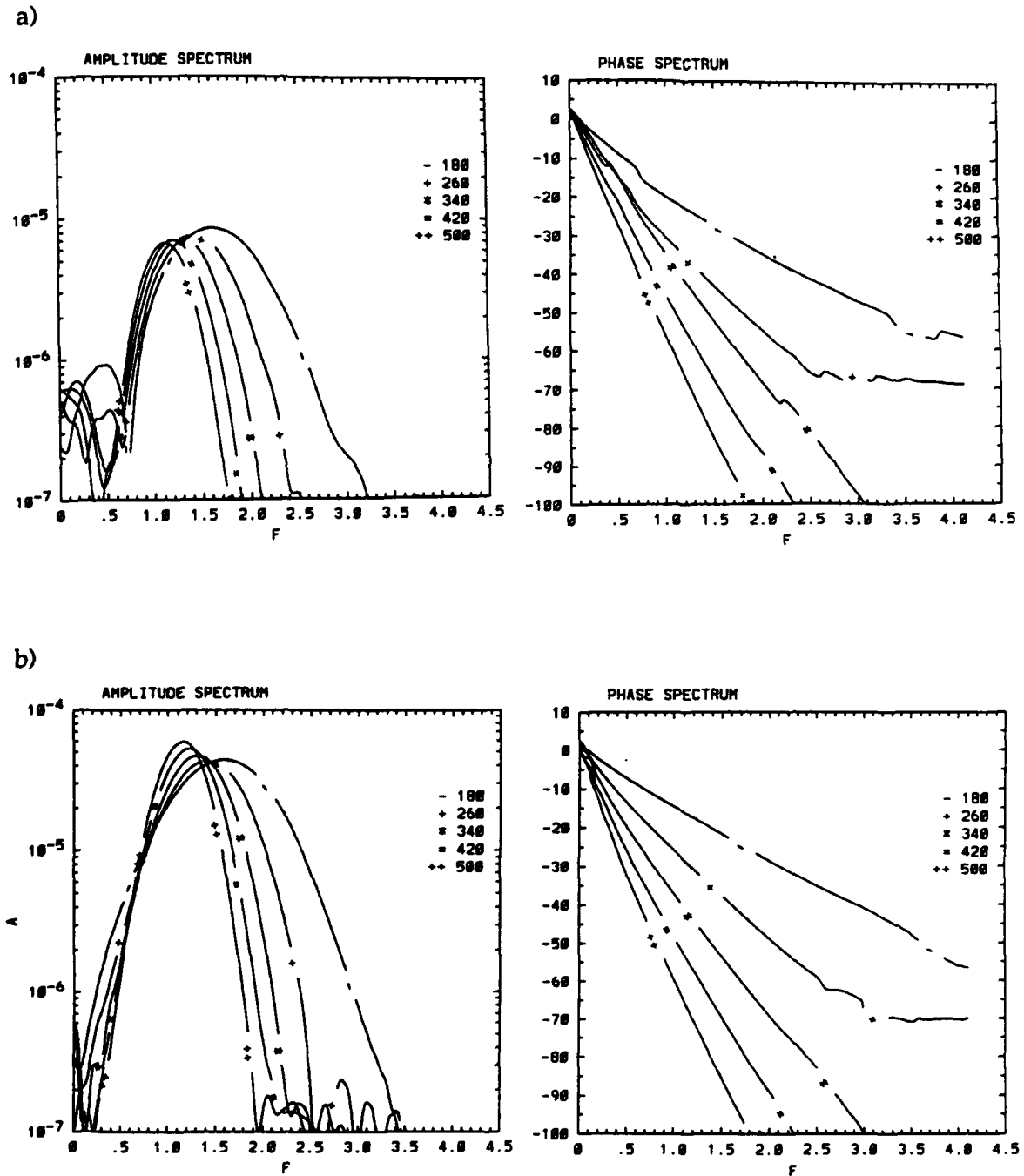


Fig. 34: Amplitude- and Phase- spectra of the spanwise vorticity signal with no control applied, for a) the two-dimensional mode  $\omega'_{z k=0}$  at the wall surface and b) the three-dimensional mode  $\omega'_{z k=1}$  at the wall surface, and for c) the three-dimensional mode  $\omega'_{z k=1}$  at  $y/\Delta y = 10$ , at the streamwise positions  $x/\Delta x = 180, 260, 340, 420, 500$ .

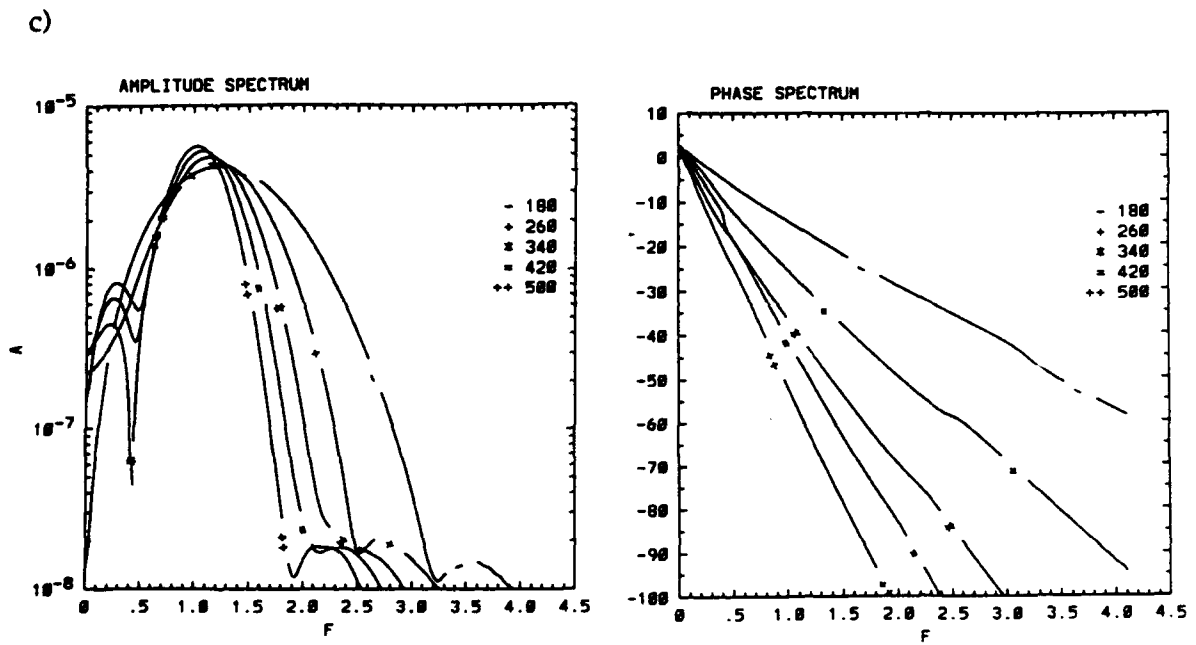


Fig. 34c: continued.

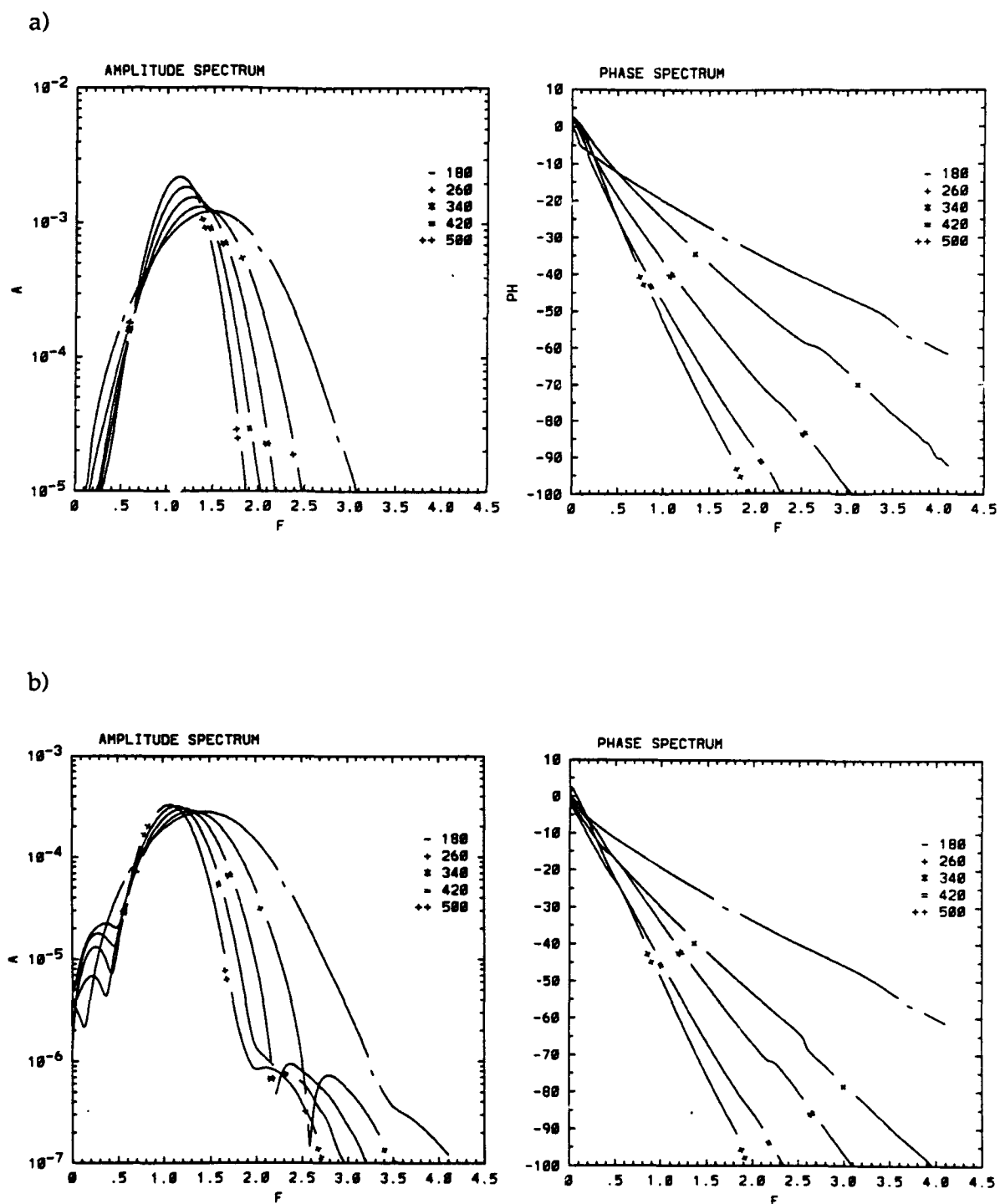


Fig. 35: Amplitude- and Phase- spectra of the wall normal velocity signal at  $y/\Delta y=40$  for a) the two-dimensional mode  $v'_{k=0}$  and for b) the three-dimensional mode  $v'_{k=1}$  with no control applied, at  $x/\Delta x = 180, 260, 340, 420, 500$ .

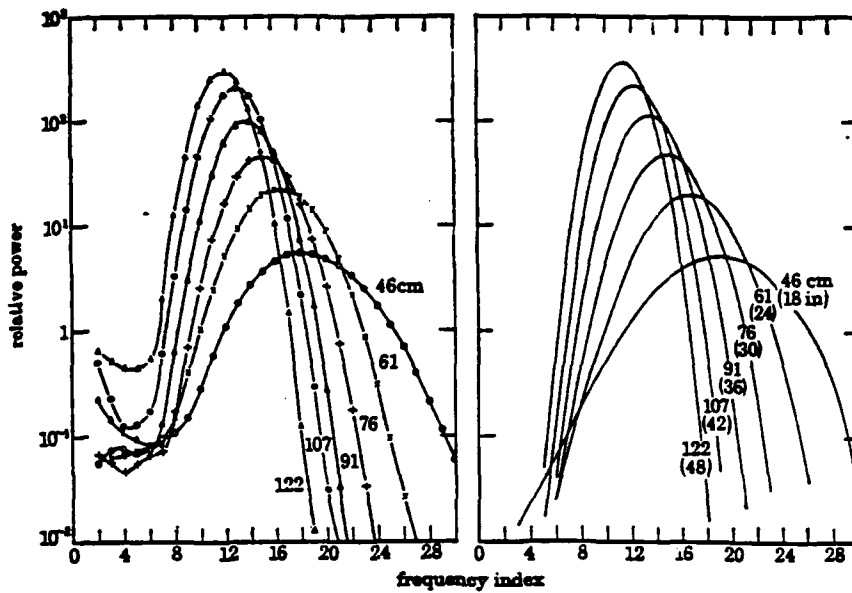


FIGURE 4

FIGURE 5

FIGURES 4 AND 5. The power spectra of two dimensional waves at different locations: figure 4, experimental measurements; figure 5, based on the model.

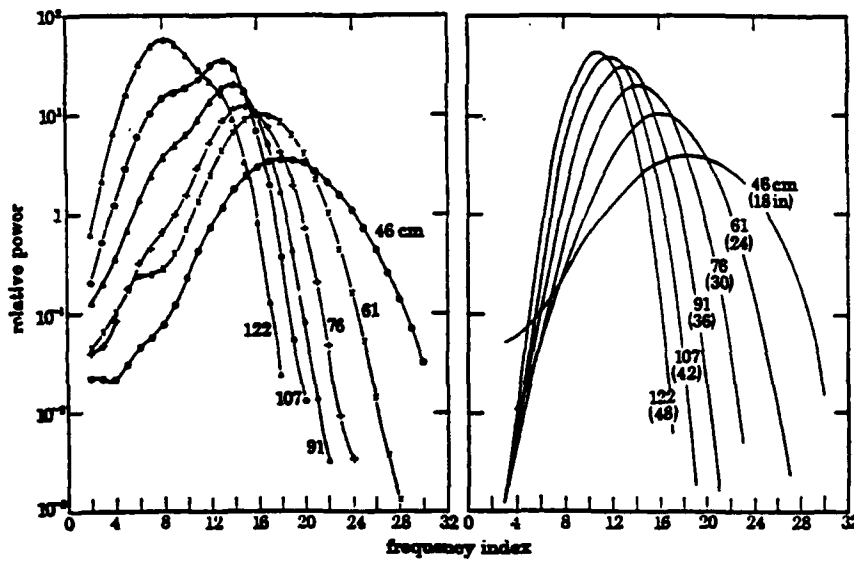


FIGURE 6

FIGURE 7

FIGURES 6 AND 7. Development of the spectra of oblique waves for  $m = 6$ , where  $\delta \delta^* = m \times R_1^* \times 19.4 \times 10^{-2}$ : figure 6, experimental results; figure 7 computed behaviour.

Fig. 36: Comparison of the experimental amplitude spectra with the computed spectra of the linear spatial stability theory from Gaster and Grant (1975). The measured spectra are taken at a wall normal distance outside the boundary layer  $y/\delta = 1.1$ .

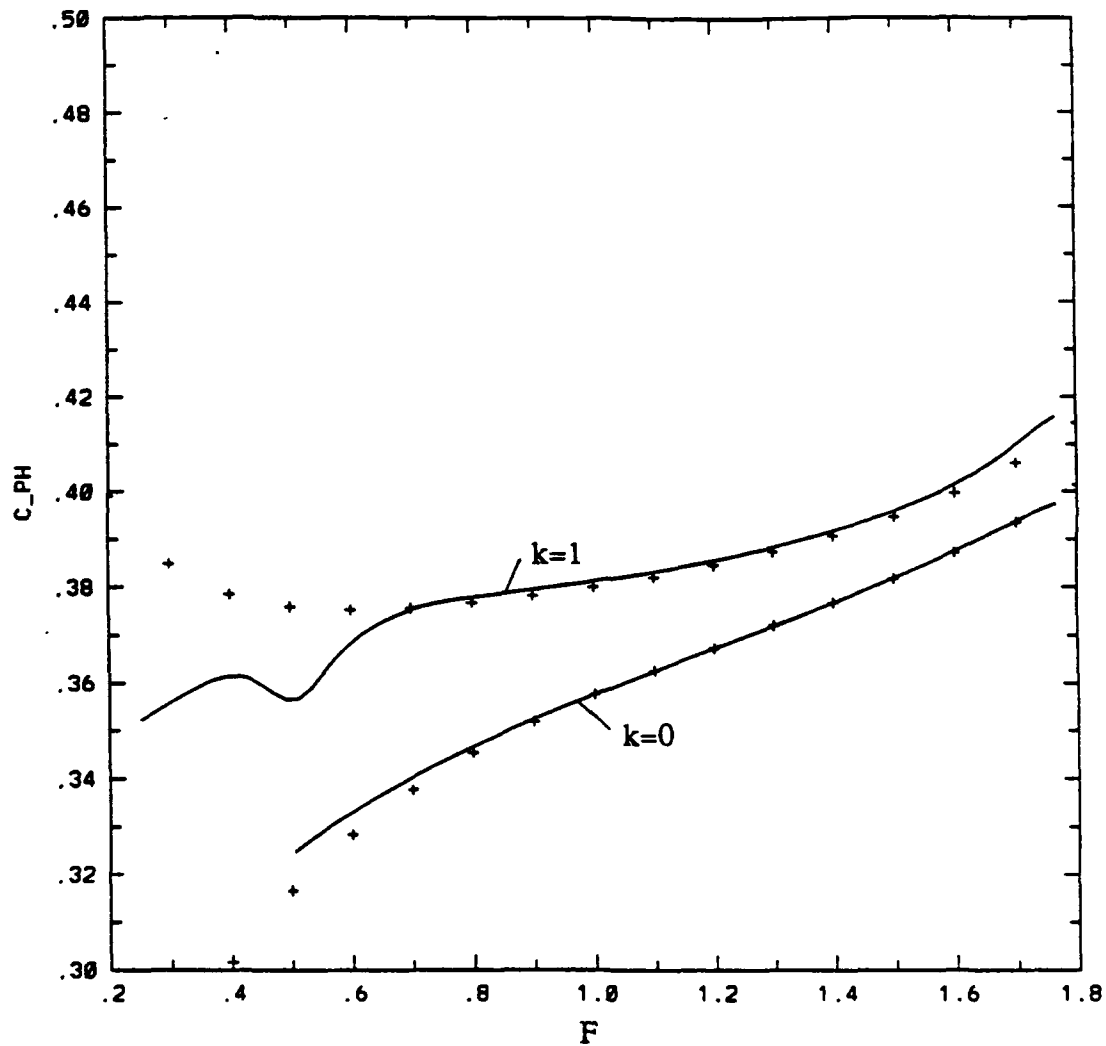


Fig. 37: Comparison of the phase velocities at  $x/\Delta x = 460$ , ( $Re_{\delta 1} = 1021$ ) with the linear stability theory ('+' symbols) for the two-dimensional ( $k=0$ ) and the three-dimensional ( $k=1$ ) spanwise modes of the wall normal velocity  $v'$  at  $y/\Delta y = 40$ .

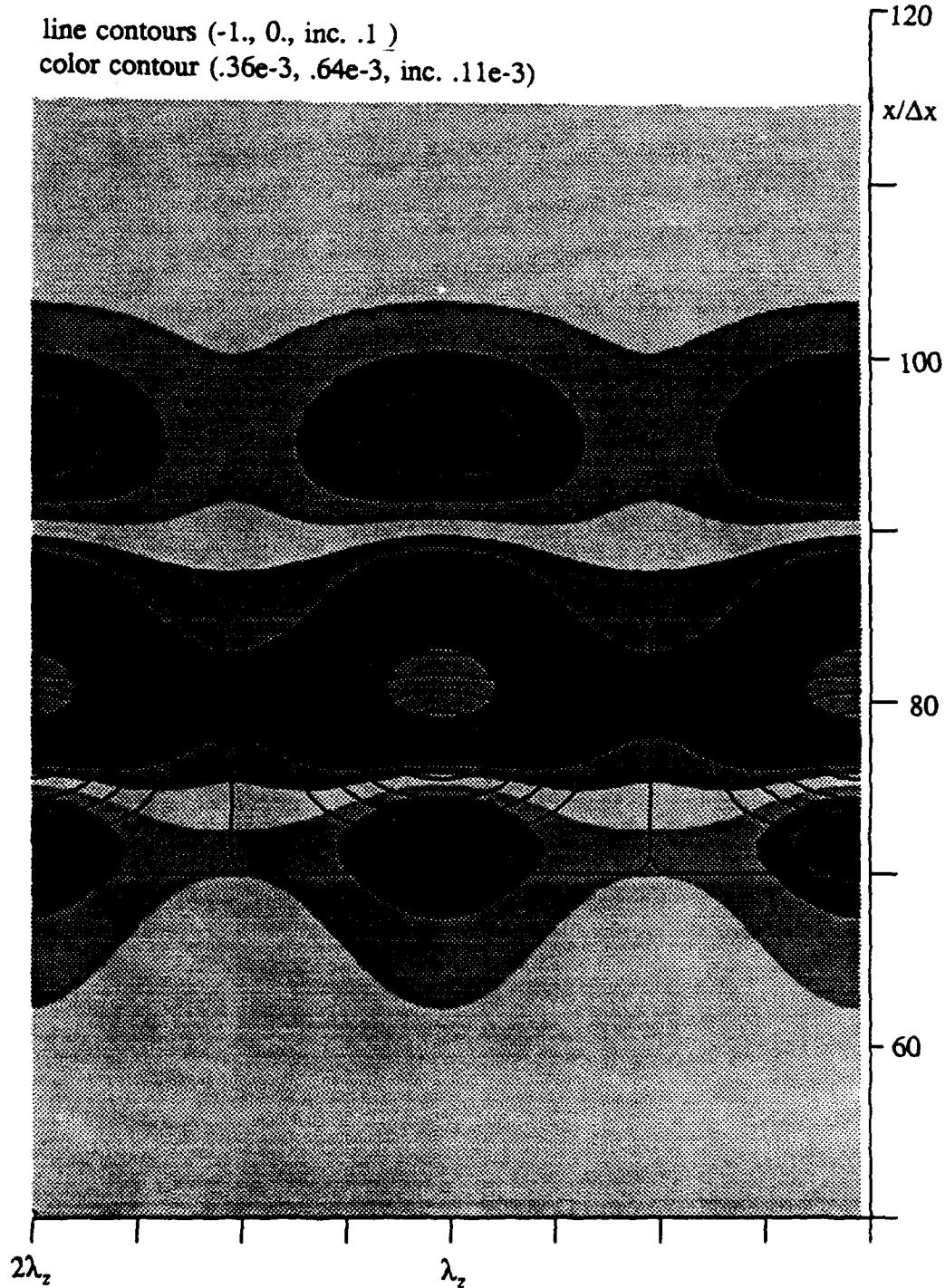


Fig. 38: The streamwise velocity component  $u'$  in the horizontal plane at the disturbance maximum (color contours) and the wall temperature disturbance  $\theta'$  (line contours) at  $t/\Delta t = 70$  during the forcing cycle.

line contours (-1., 0., inc. .1 )  
 color contour (-.16, .16, inc. .08e-1)

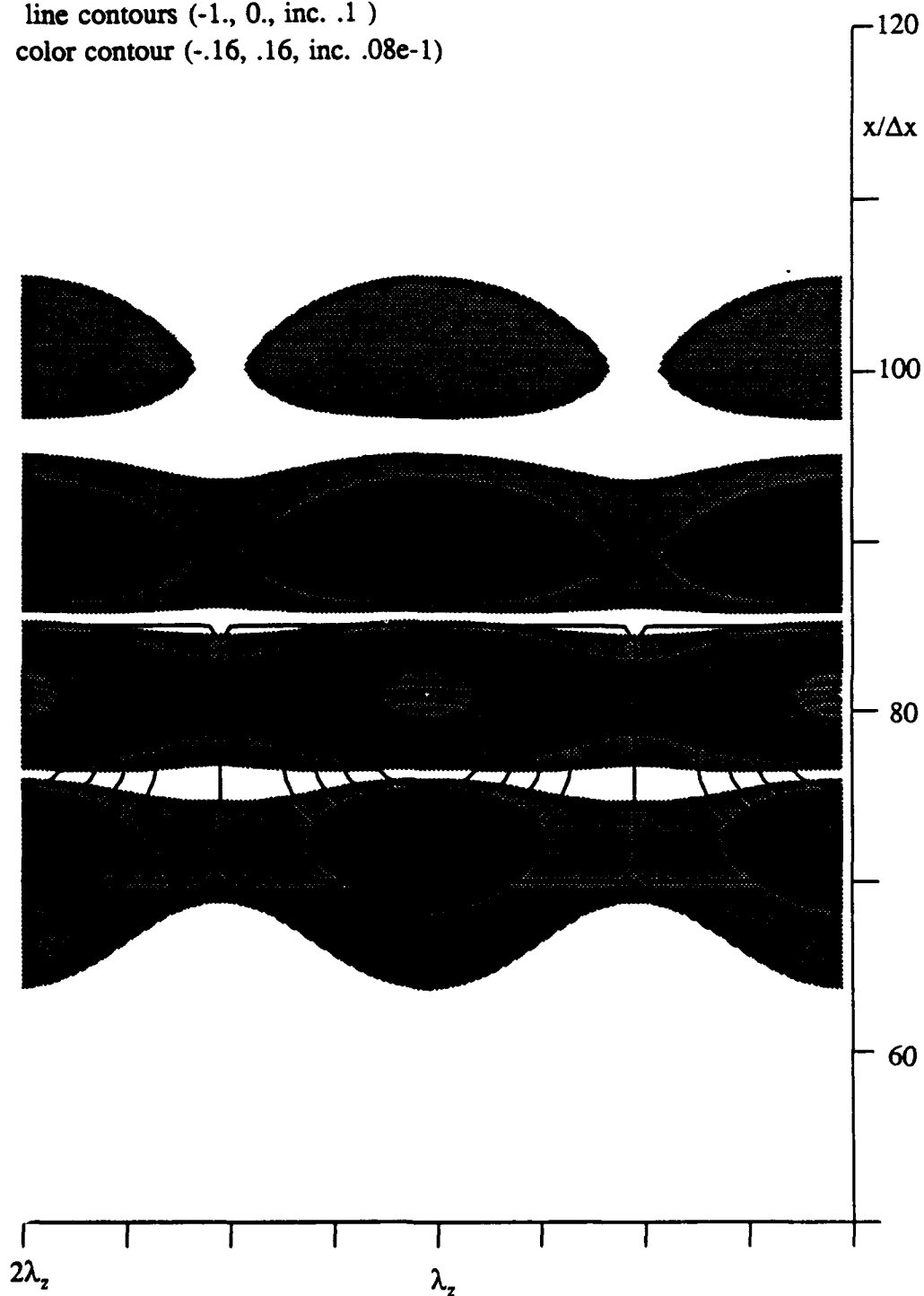


Fig. 39: The wall normal velocity component  $v'$  in the horizontal plane at the disturbance maximum (grey-shaded contours) and the wall temperature disturbance  $\theta'$  (line contours) at  $t/\Delta t = 70$  during the forcing cycle.

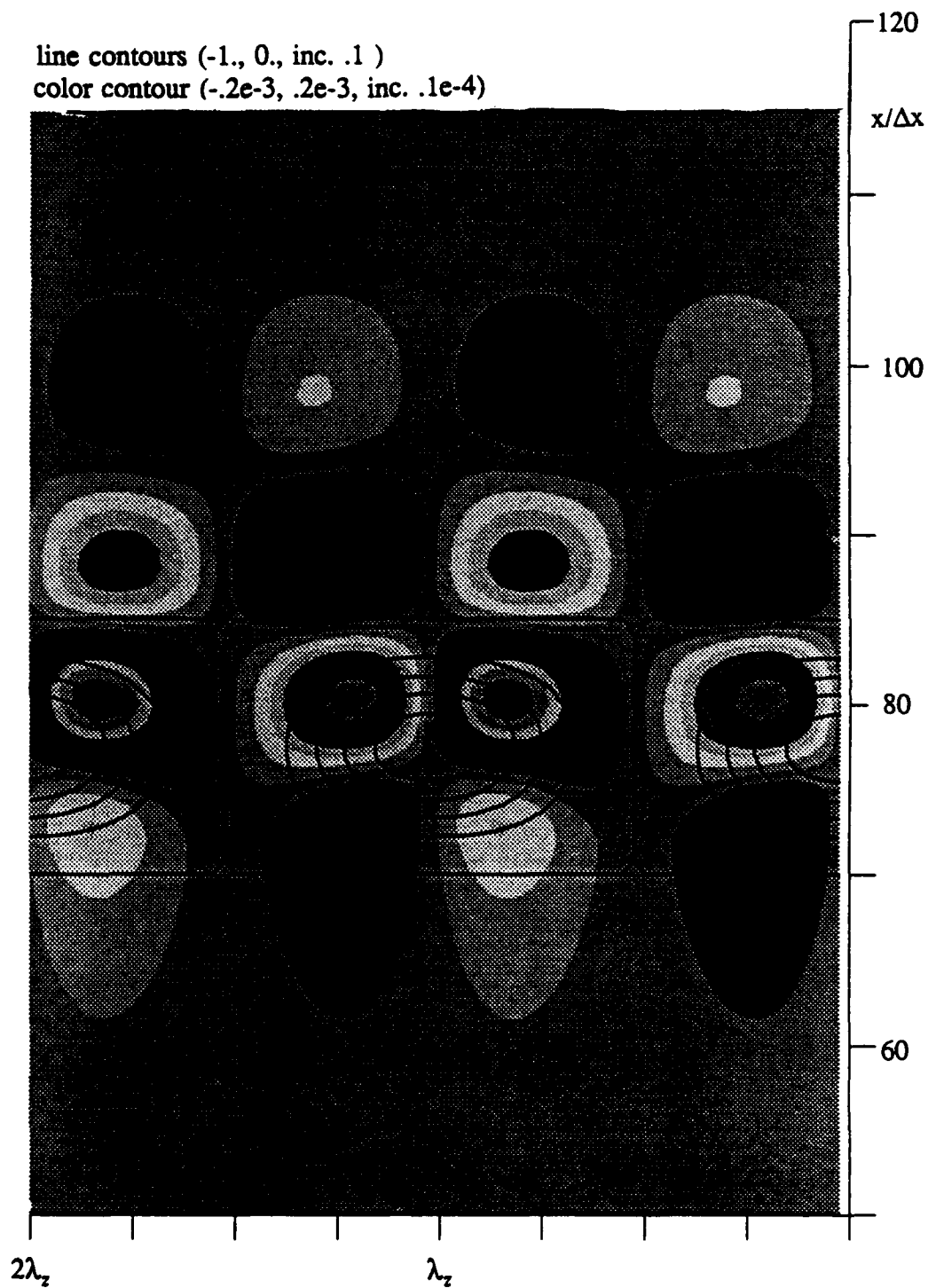


Fig. 40: The spanwise velocity component  $w'$  in the horizontal plane at the disturbance maximum (grey-shaded contours) and the wall temperature disturbance  $\theta'$  (line contours) at  $t/\Delta t = 70$  during the forcing cycle.

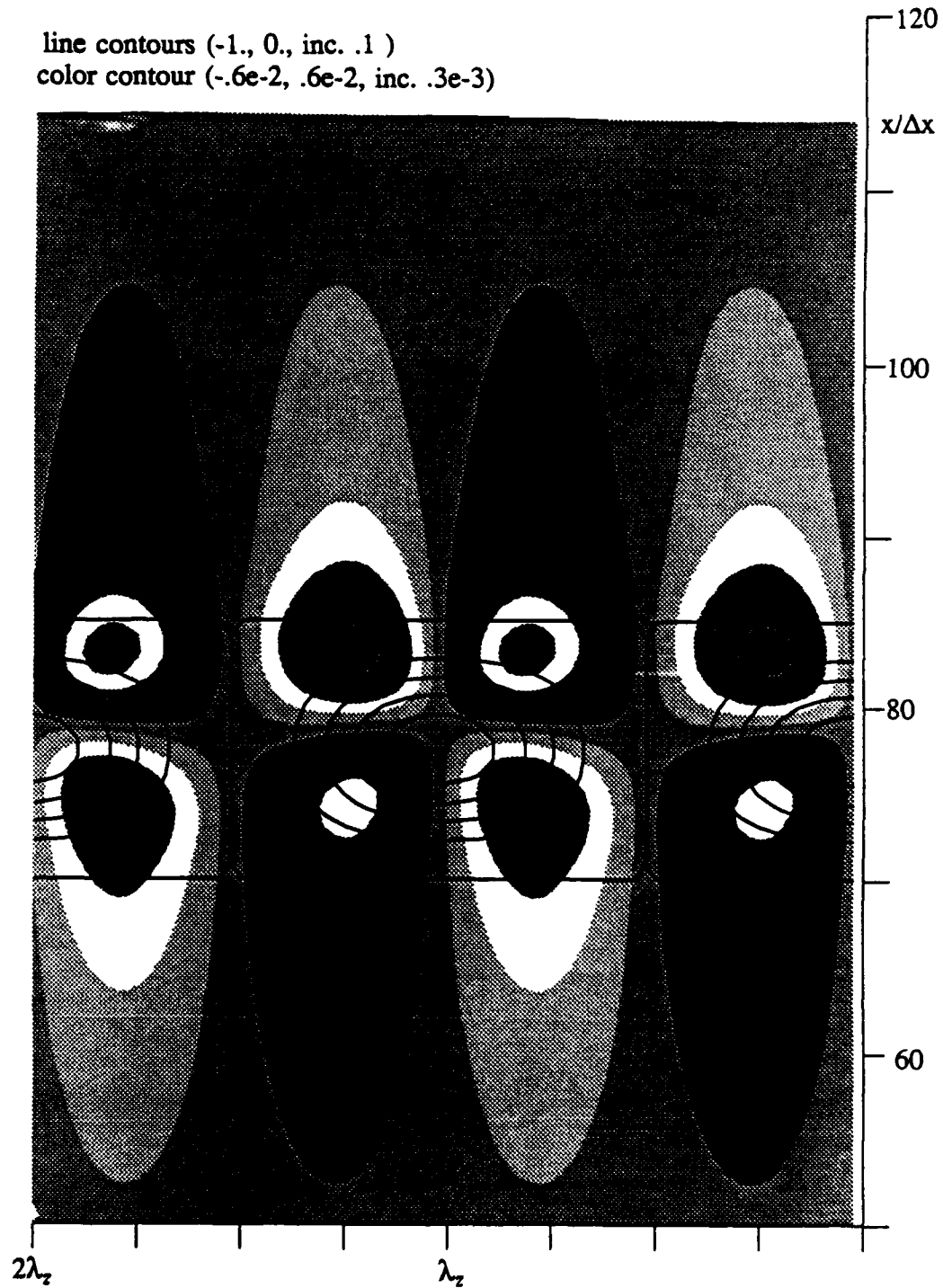


Fig. 41: The streamwise vorticity  $\omega'_x$  in the horizontal plane at the disturbance maximum (grey-shaded contours) and the wall temperature disturbance  $\theta'$  (line contours) at  $t/\Delta t = 70$  during the forcing cycle.

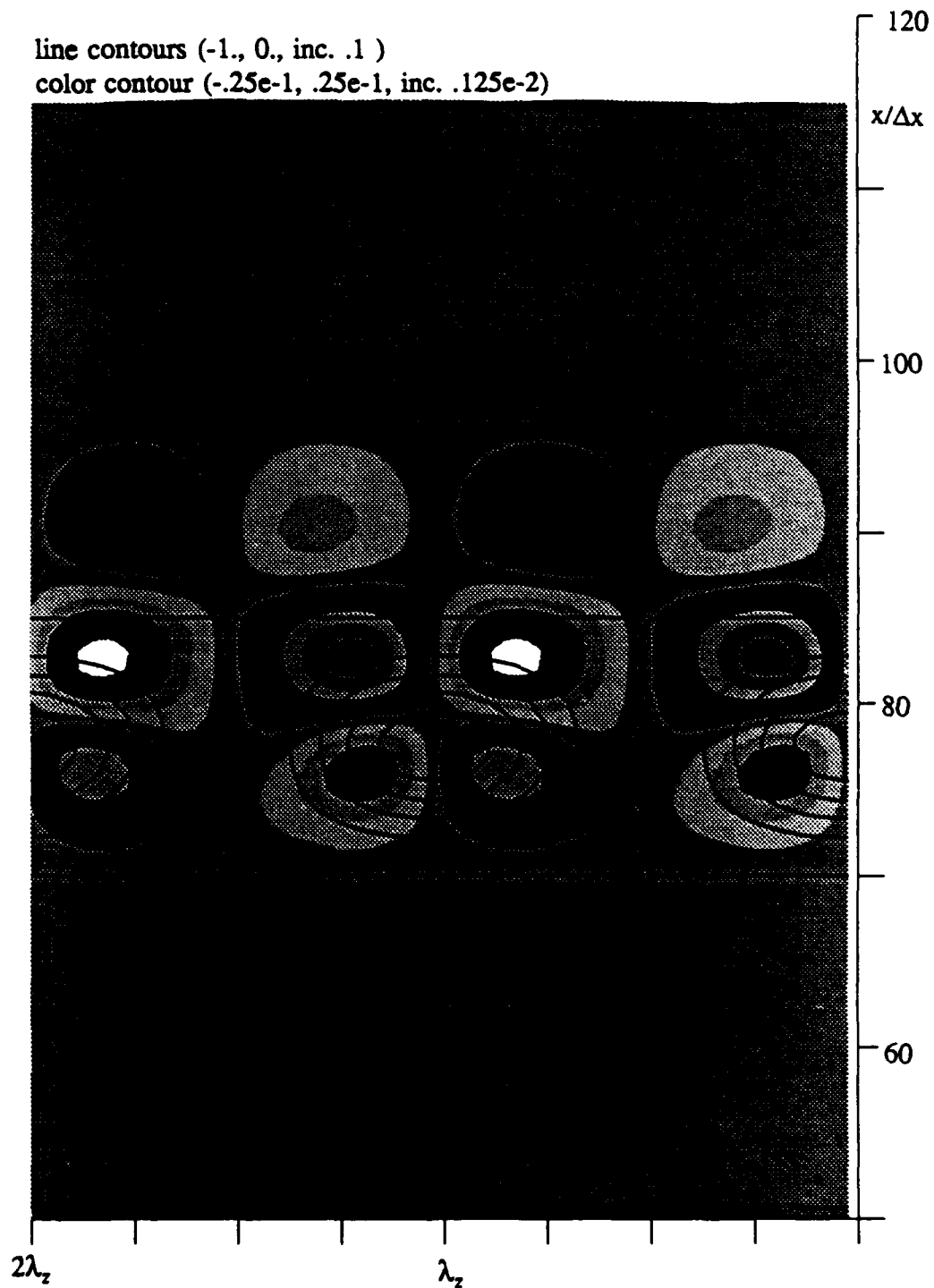


Fig. 42: The wall normal vorticity  $\omega'_y$  in the horizontal plane at the disturbance maximum (grey-shaded contours) and the wall temperature disturbance  $\theta'$  (line contours) at  $t/\Delta t = 70$  during the forcing cycle.

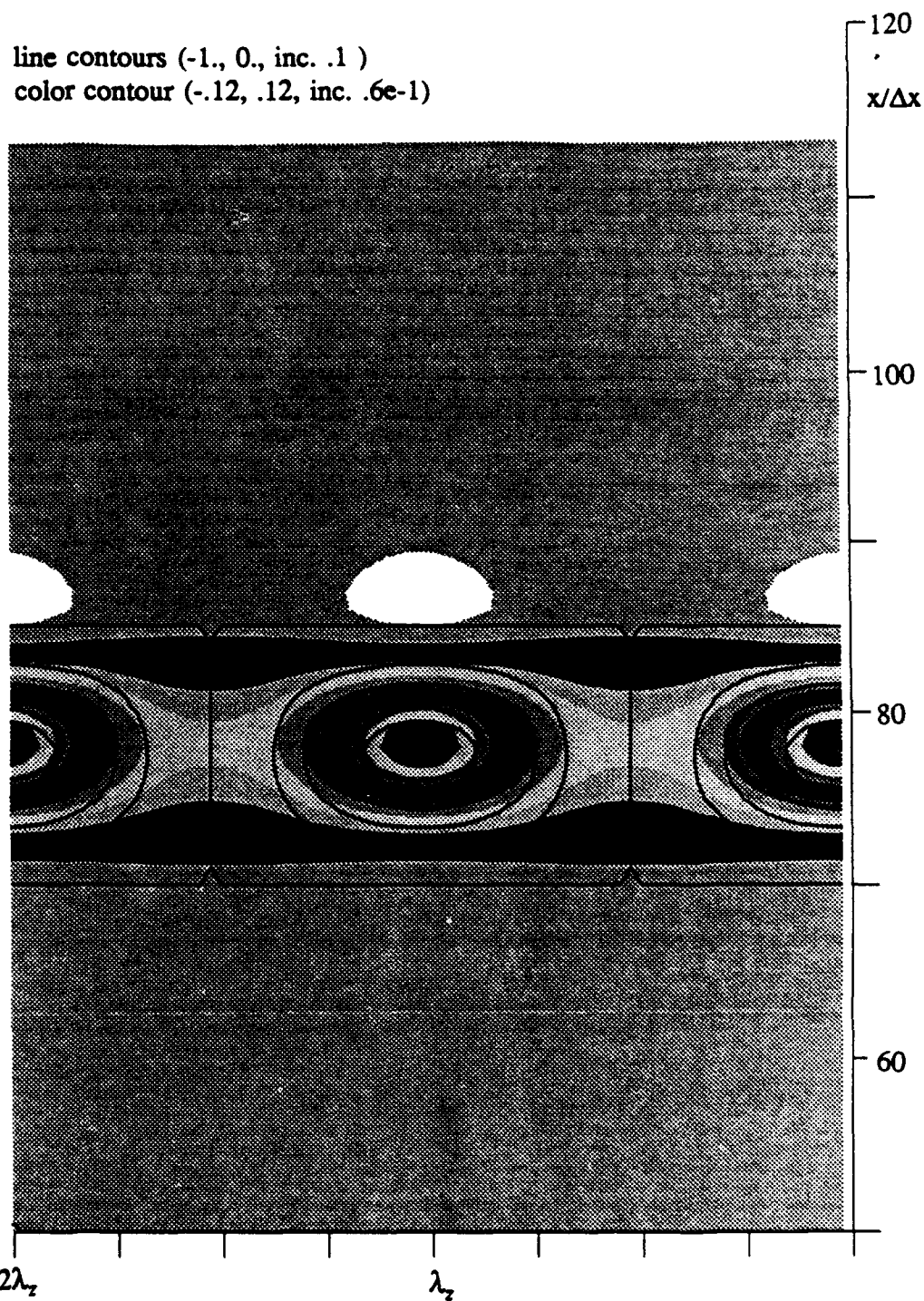


Fig. 43: The spanwise vorticity  $\omega'_z$  in the horizontal plane at the disturbance maximum (grey-shaded contours) and the wall temperature disturbance  $\theta'$  (line contours) at  $t/\Delta t = 70$  during the forcing cycle.

line contours (-.35e-3, .35e-3, inc. .7e-4)  
 color contours (-.2e-2, .2e-2, inc. .2e-3)

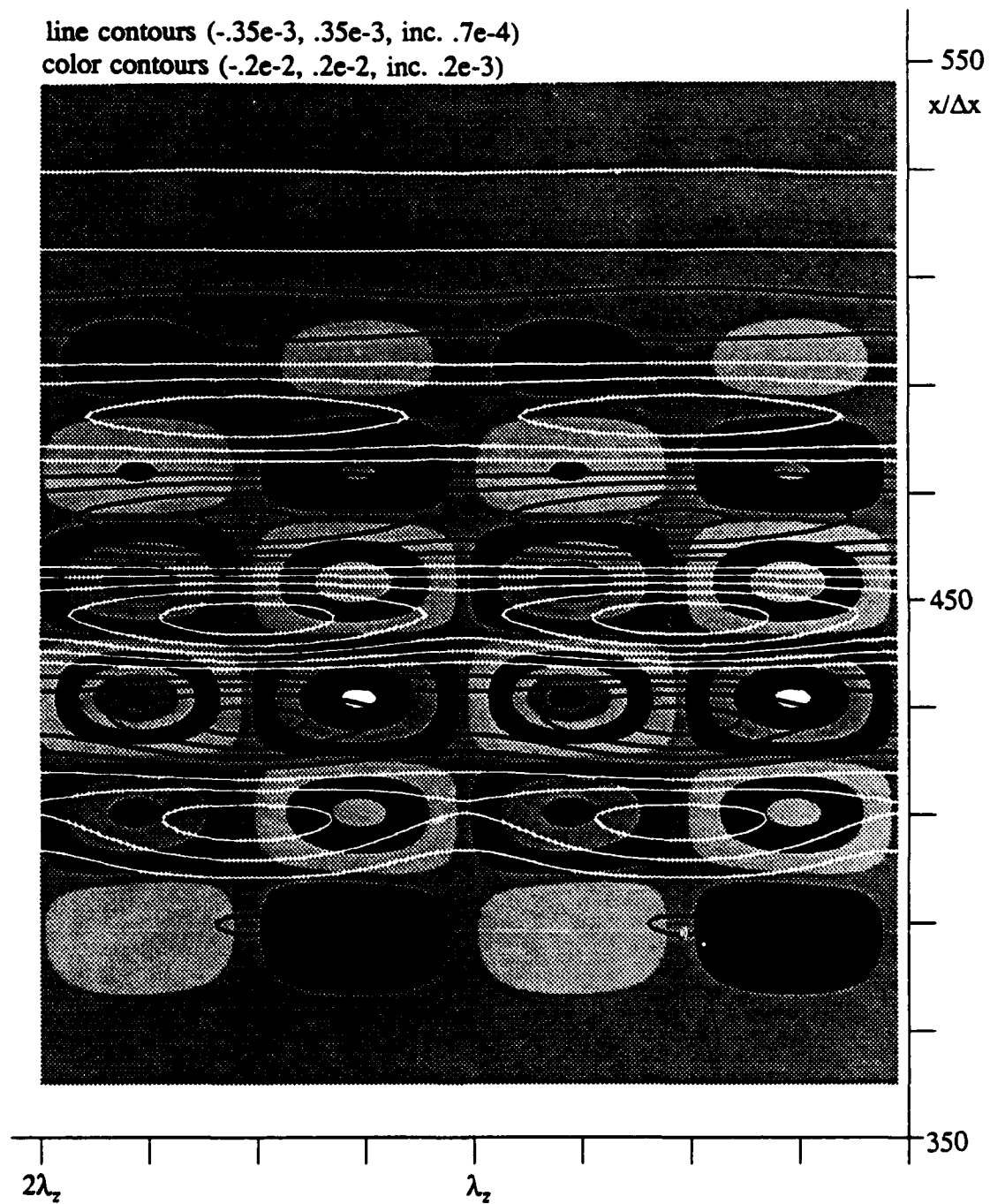


Fig. 44: The streamwise vorticity  $\omega'_x$  in the horizontal plane at the plate surface (grey-shaded contours) and the spanwise vorticity  $\omega'_z$  (line contours) at  $t/\Delta t = 1200$ .

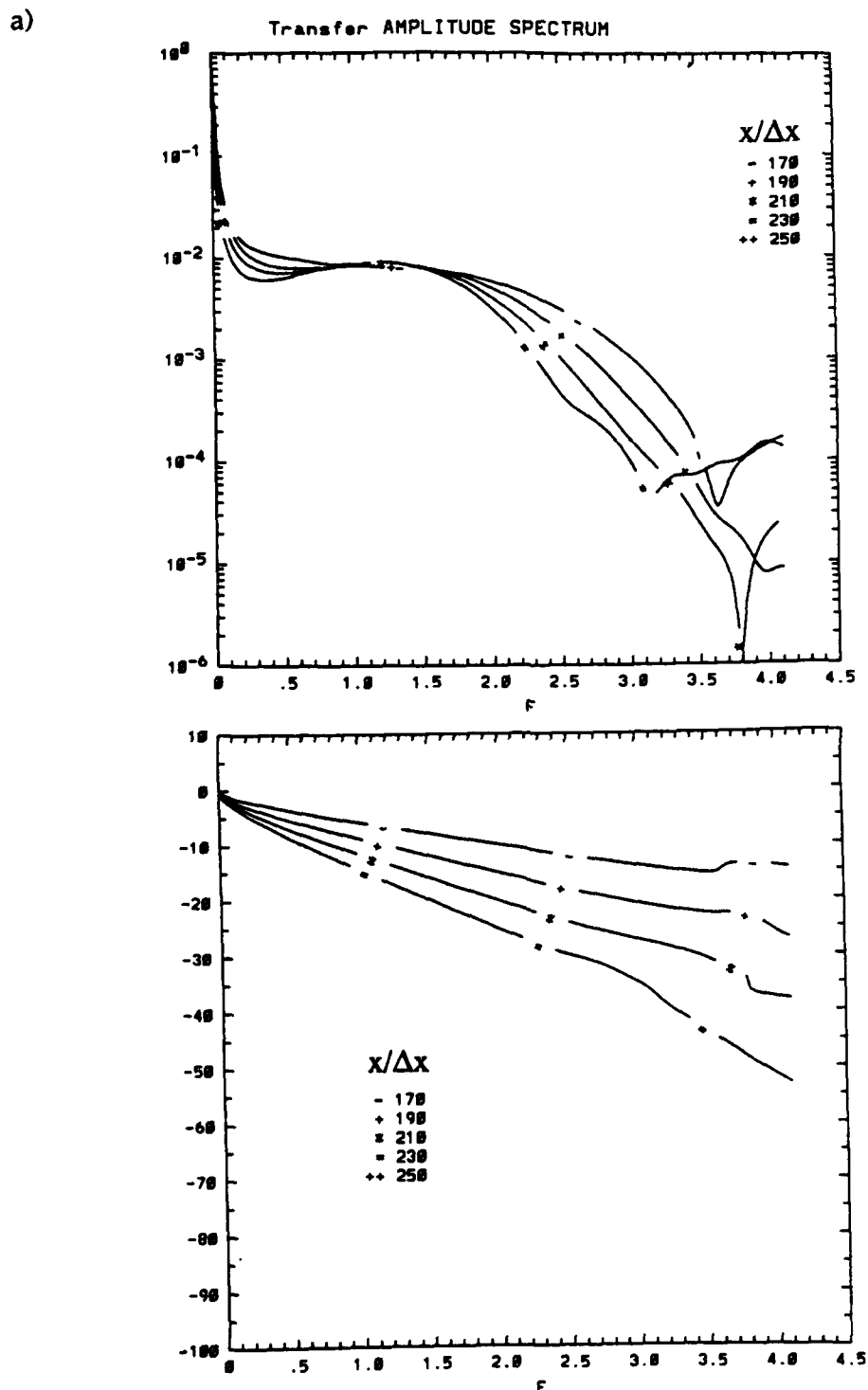


Fig. 45: Modulus and argument of the transfer function at several streamwise positions with the heater strip width  $130 \leq x/\Delta x \leq 145$  for a) the two-dimensional mode ( $k=0$ ) and b) the three-dimensional spanwise horizontal mode ( $k=1$ ).

b)

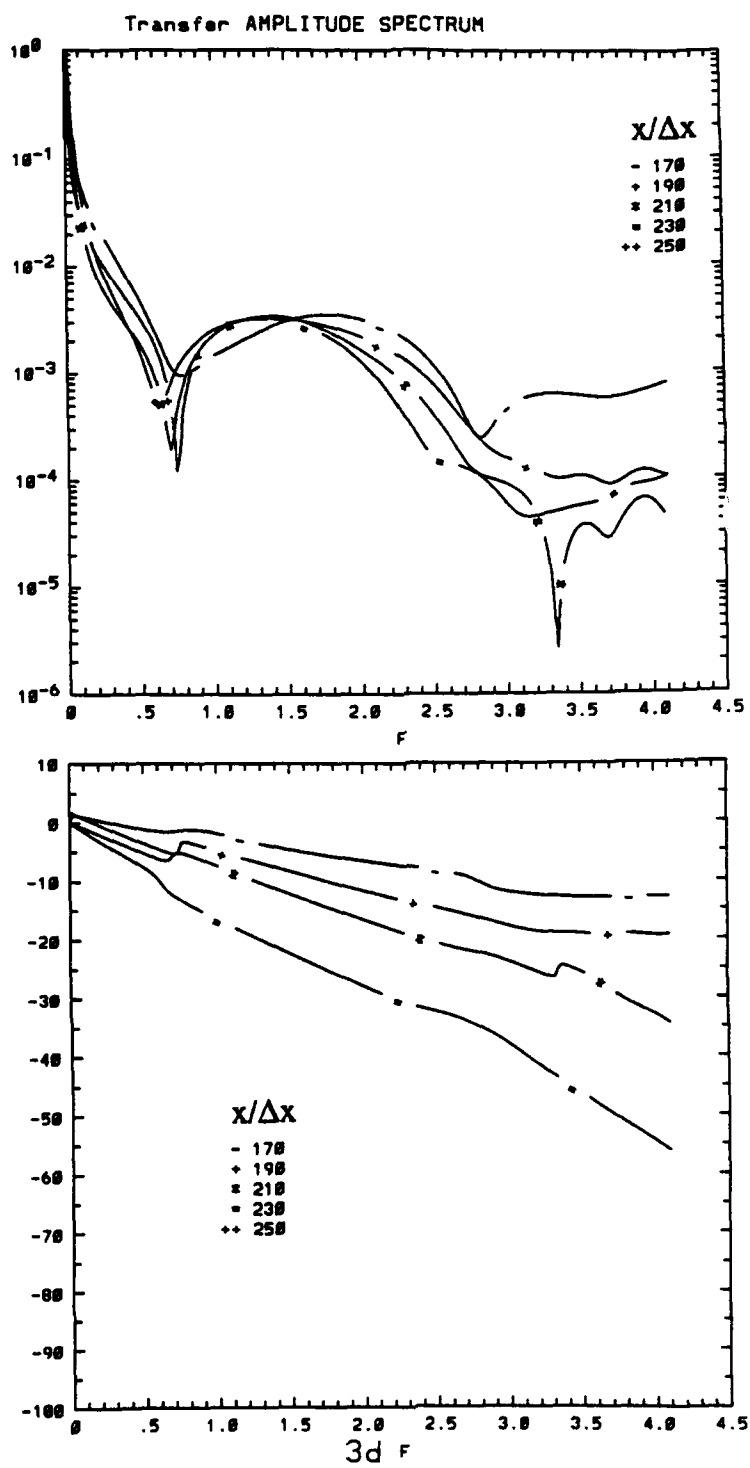


Fig. 45b: continued.

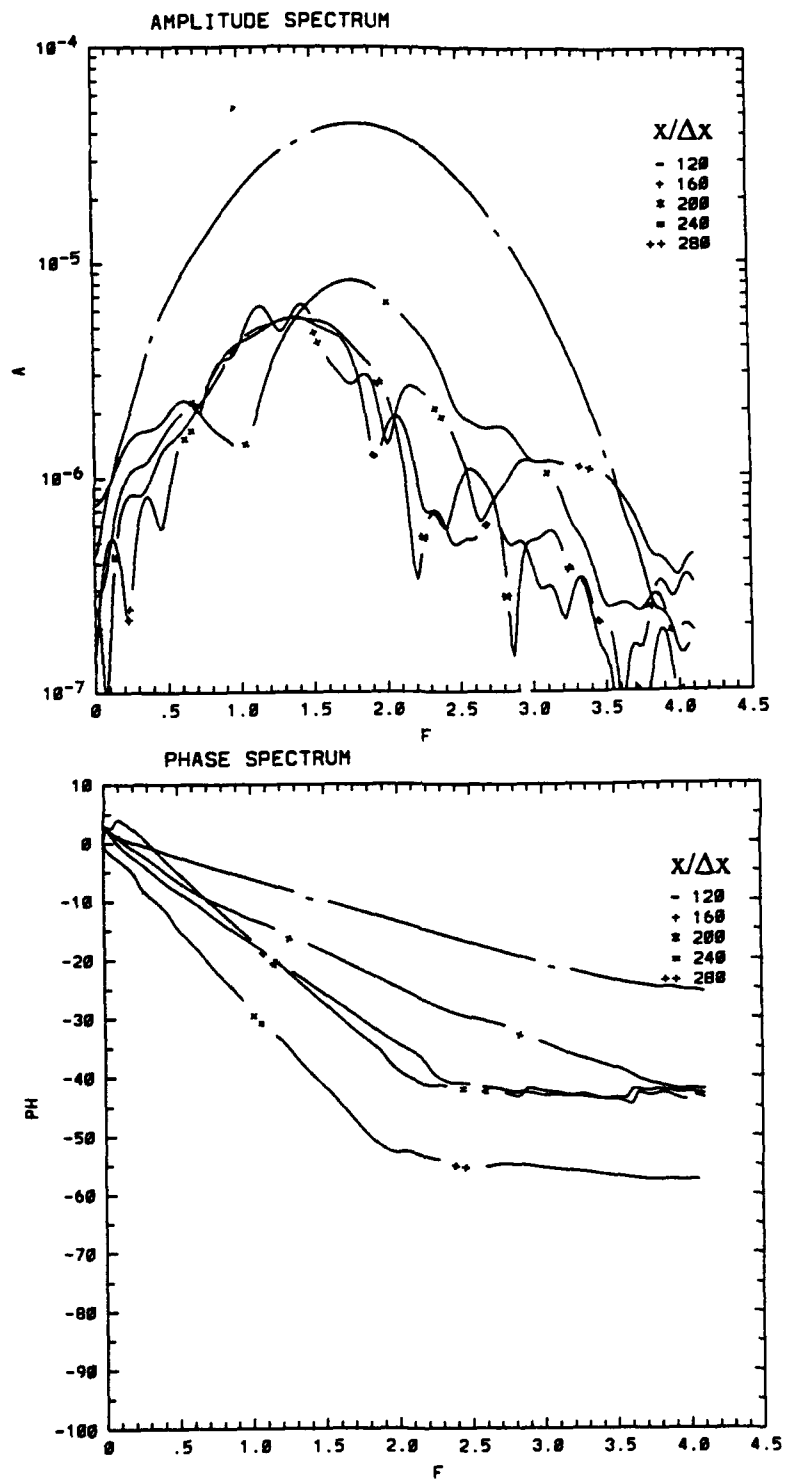


Fig. 46: Amplitude- and Phase- spectra of the spanwise vorticity signal  $\omega'_{z,k=0}$  at the wall surface for the two-dimensional mode at several streamwise positions, with control applied. The control strip is at  $130 \leq x/\Delta x \leq 145$ .

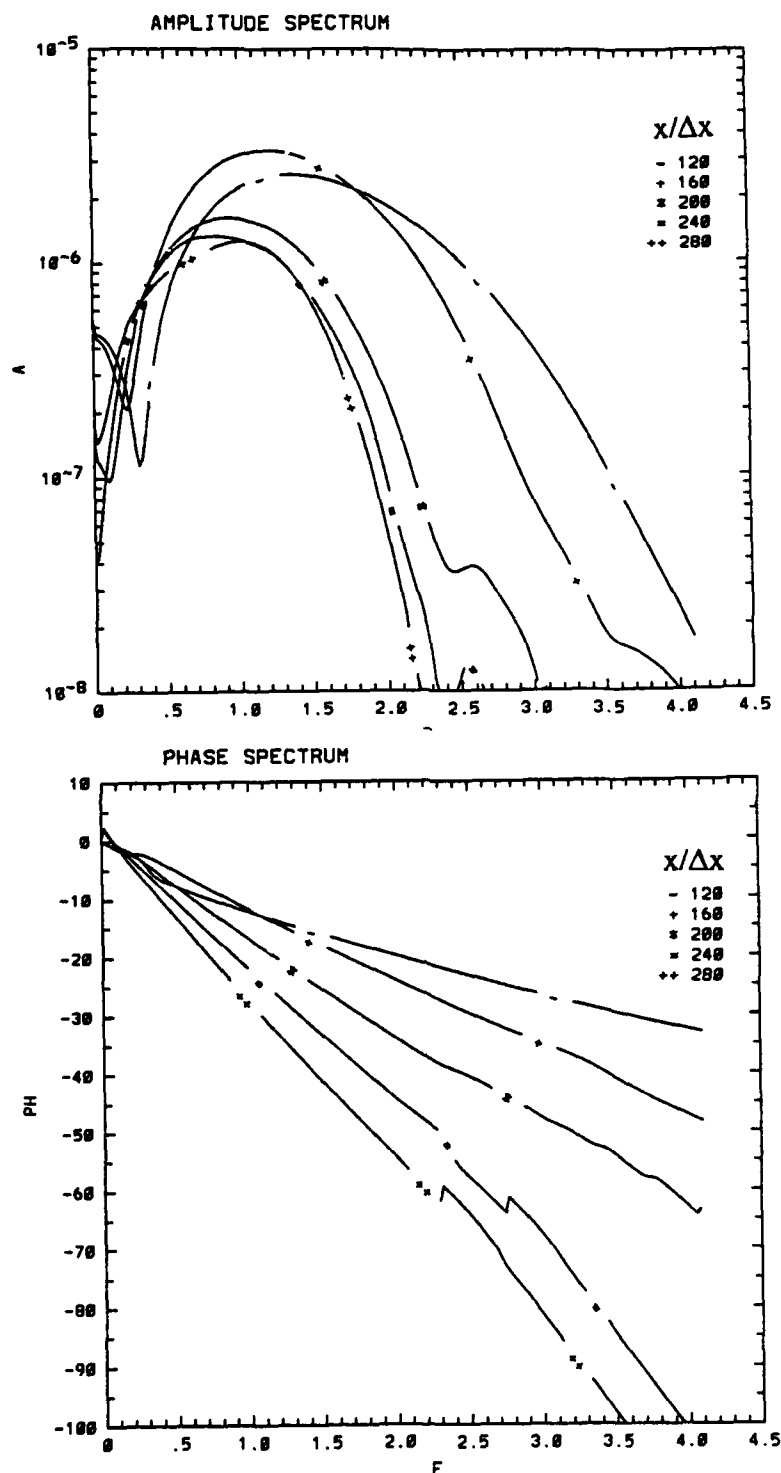


Fig. 47: Amplitude- and Phase- spectra of the spanwise vorticity signal  $\omega'_{z,k=1}$  at  $y/\Delta y=10$  for the three-dimensional mode at several streamwise positions, with control applied. The control strip is at  $130 \leq x/\Delta x \leq 145$ .

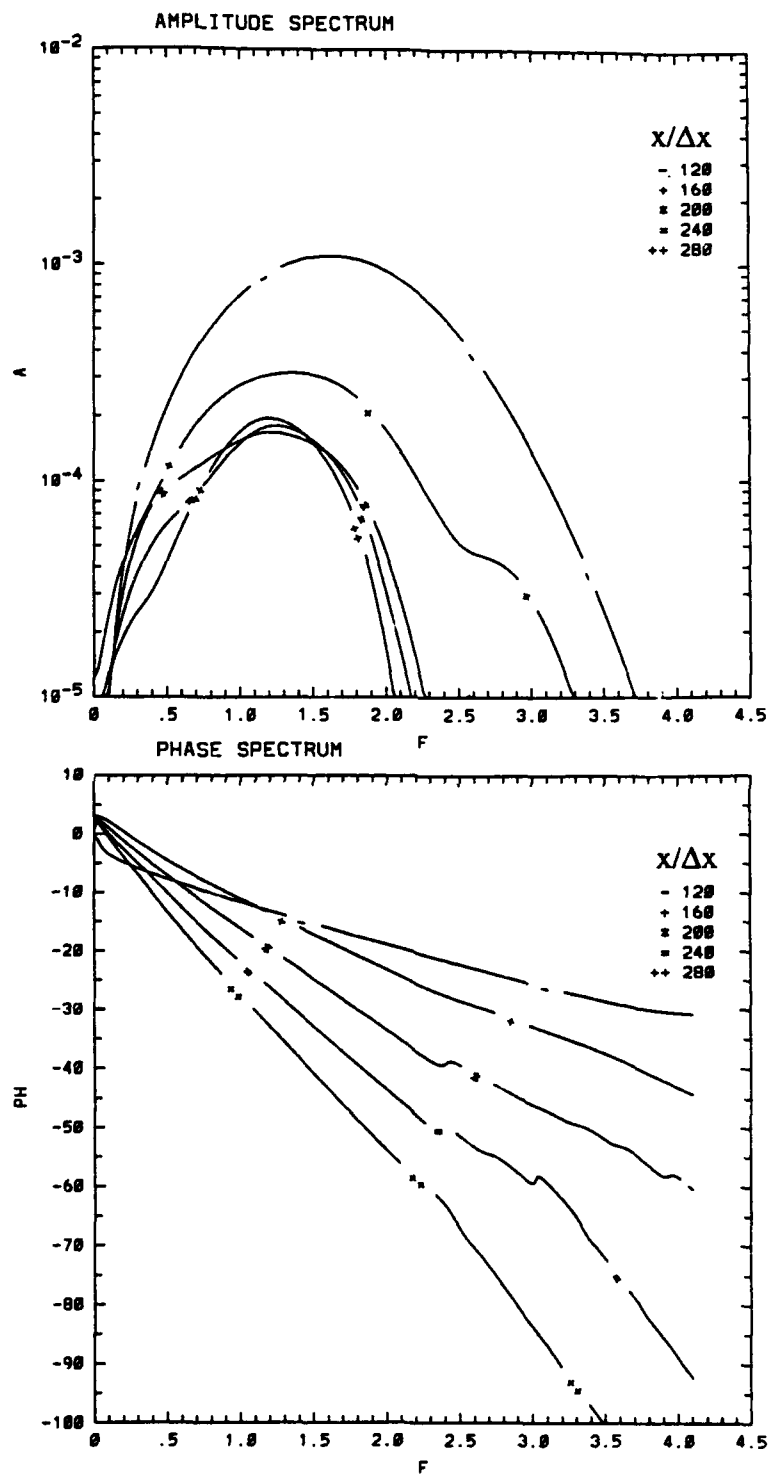


Fig. 48: Amplitude- and Phase- spectra of the wall normal velocity signal  $v'_{k=0}$  at  $y/\Delta y=40$ , for the two-dimensional spanwise mode at several streamwise positions with control applied. The control strip is at  $130 \leq x/\Delta x \leq 145$ .

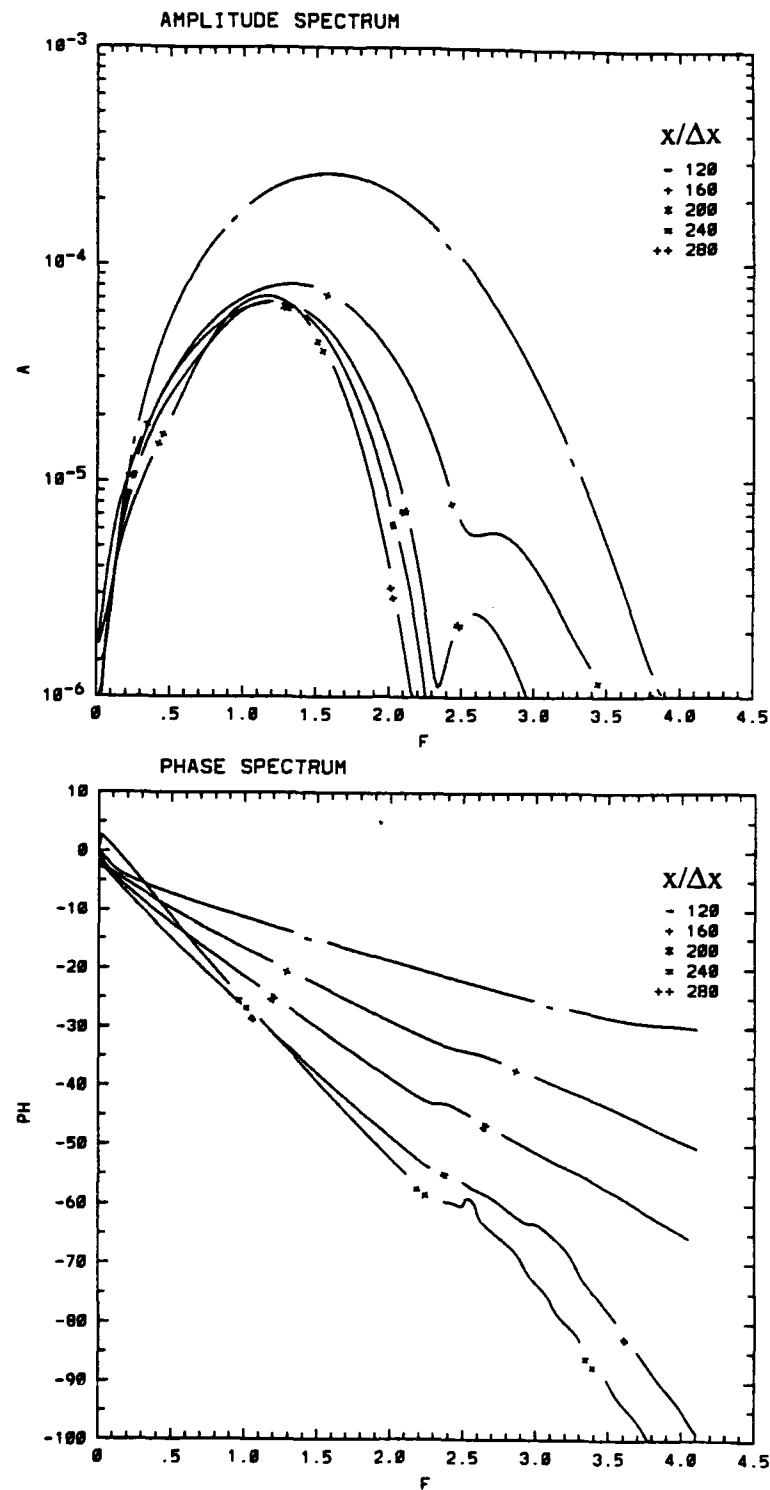


Fig. 49: Amplitude- and Phase- spectra of the wall normal velocity signal  $v'_{k=1}$  at  $y/\Delta y=40$ , for the three-dimensional spanwise mode at several streamwise positions with control applied. The control strip is at  $130 \leq x/\Delta x \leq 145$ .

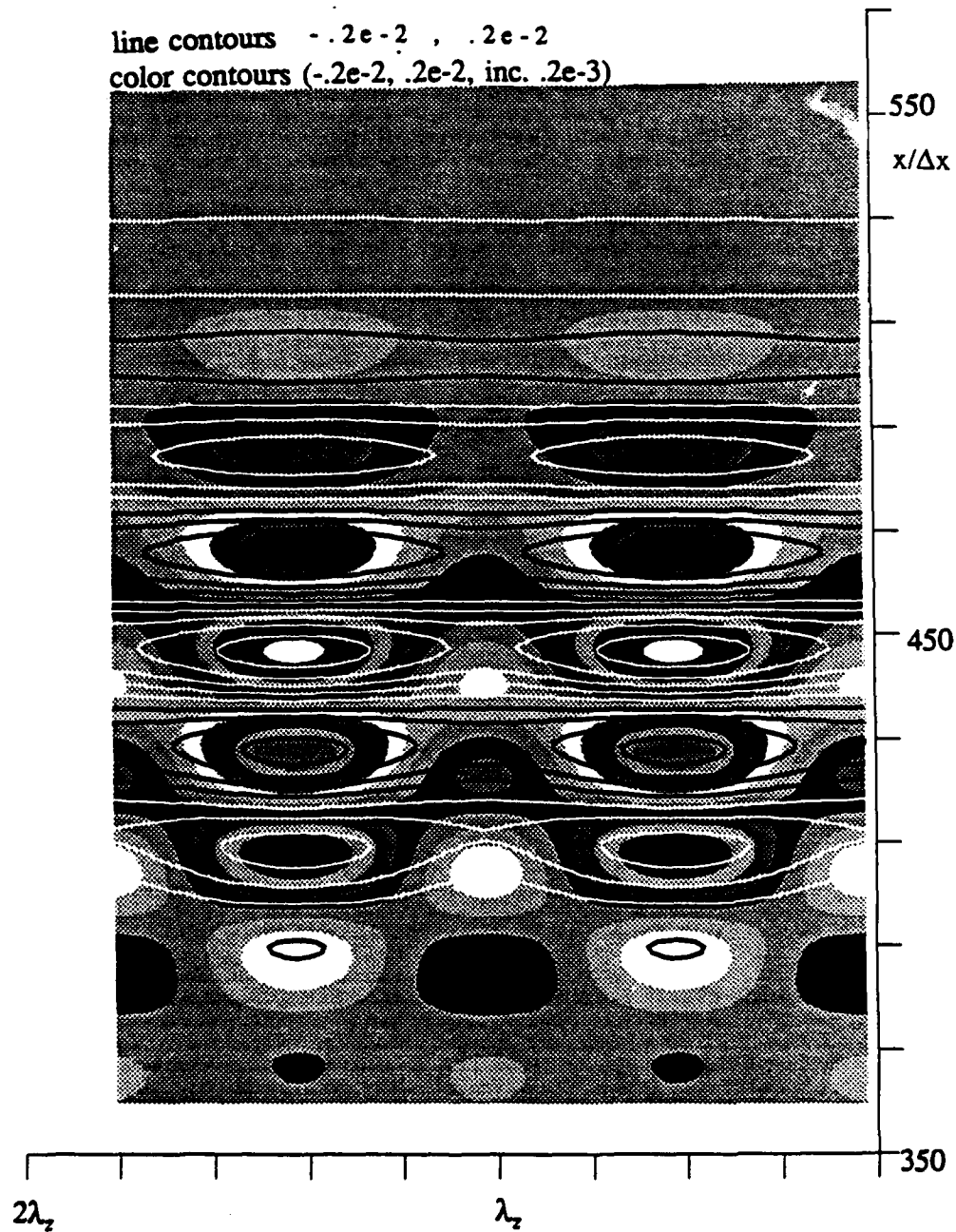


Fig. 50: The spanwise vorticity  $\omega'_z$  in the horizontal plane at the plate surface for the control of the two-dimensional spanwise mode only (grey-shaded contours) and the spanwise vorticity  $\omega'_z$  for no control (line contours) at  $t/\Delta t = 1200$ .

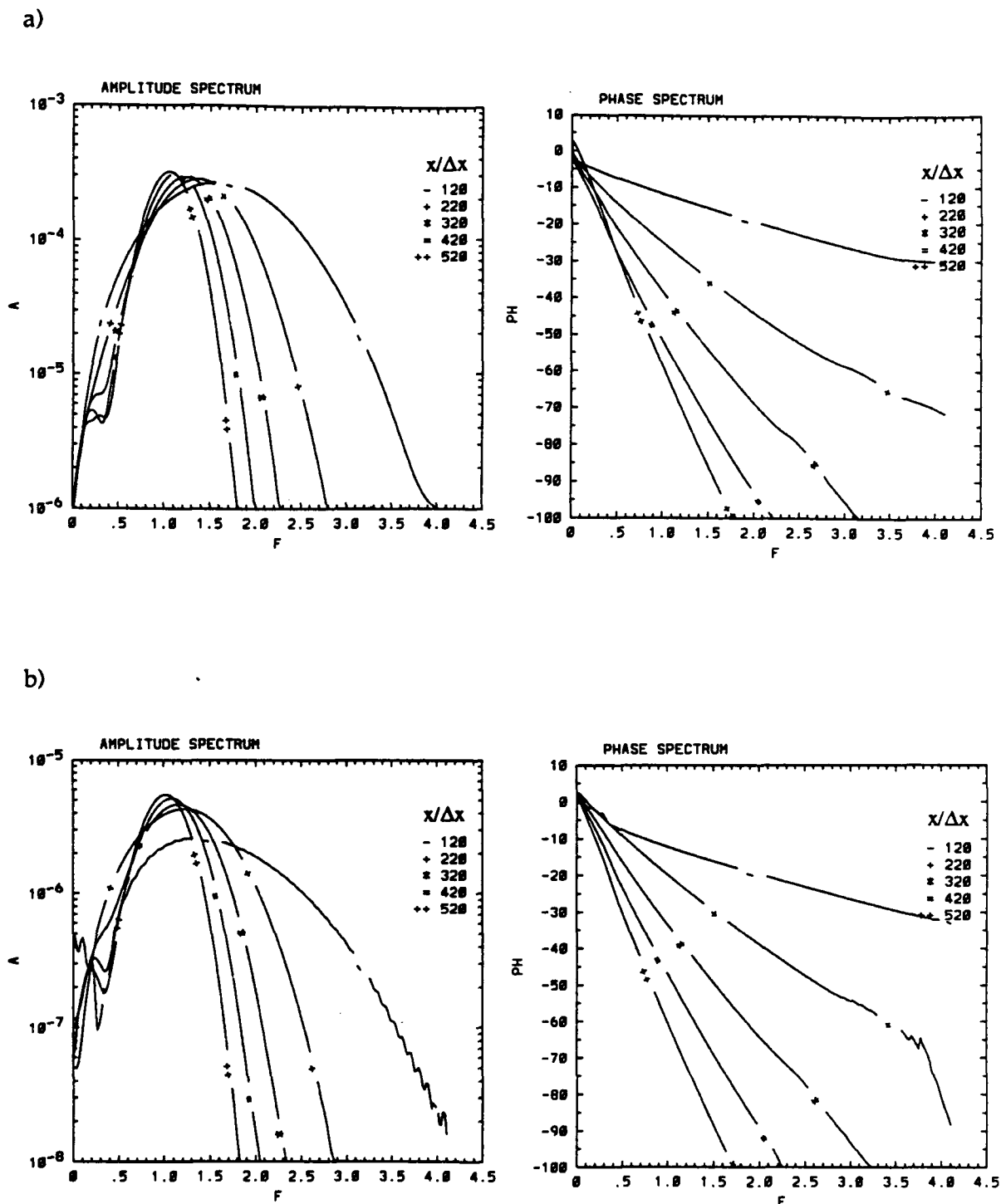


Fig. 51: Amplitude and Phase-spectra for the case of only the two-dimensional mode attenuated, for a) the three-dimensional wall normal velocity  $v'_{k=1}$  at  $y/\Delta y=40$  and b) the three-dimensional spanwise vorticity  $\omega'_{z,k=1}$  at  $y/\Delta y=10$ .

## Appendix A: Fourier Transform of Non-Periodic Signals and Estimation of the Transfer Function

For the practical implementation of the discrete Fourier Transform (DFT) we are restricted to finite length sequences of digital signals at selected values of the angular frequency. A periodic signal of period  $N$  has the property that

$$u(n+N) = u(n). \quad (\text{A.1})$$

This periodic sequence can be represented by the discrete Fourier Transform of a finite-length sequence  $u(0), u(1), \dots, u(N-1)$  by

$$u(n) = \sum_{m=0}^{N-1} U(m) e^{-i(2\pi/N)nm} \quad (n = 0, 1, 2, \dots, N-1) \quad (\text{A.2})$$

and the inverse discrete Fourier Transform (IDFT) of a finite-length frequency sequence  $U(0), U(1), \dots, U(N-1)$  by

$$U(m) = \frac{1}{N} \sum_{n=0}^{N-1} u(n) e^{i(2\pi/N)nm} \quad (m = 0, 1, 2, \dots, N-1) \quad (\text{A.3})$$

The equations A.2 and A.3 form a DFT pair. The digital signal  $u(n)$  and the frequency signal  $U(m)$  are assumed to be periodic sequences, since they are both associated with Fourier series. Hence if  $u(n)$  is actually zero for  $n < 0$  or  $n > N-1$ , the DFT will not be aware of this, since it assumes the digital signal is periodic and exists for all integers  $n$ . Thus one must be careful in interpreting the DFT and IDFT outside the range of  $0 \leq n \leq N-1$  and  $0 \leq m \leq N-1$ .

In A.2 and A.3 the quantity  $u(n)$ ,  $n = 0, 1, 2, \dots, N-1$  is the real, sampled time-data function of the computation at some position  $(x_0, y_0)$  in the flow field. The above formula assume, that the length of the sampled data to be transformed consists of  $N$  points spaced  $\Delta t$  apart. In our computations, the timestep is chosen as  $\Delta t = \frac{2\pi}{\beta L}$ ,

where  $L$  is an integer number for proper temporal resolution, and  $\beta$  is a typical frequency of the most amplified wave component in the wave packet. The DFT is defined at  $N$  discrete values of the frequency extending up to the frequency  $f_s = N\Delta f$ , where  $\Delta f = 1/T_p$  is the elementary bandwidth, and  $T_p$  is the time period of the data sample ( $T = N\Delta t$ ). For a time waveform to be faithfully reconstructed, it is necessary that the highest frequency  $f_h$  present in the signal is less than or equal to the folding frequency  $f_N = f_s/2$ . In our computations the folding frequency is determined by  $f_N = \beta L/4\pi$ .

Before the digital time waveform is analyzed a data windowing or tapering is applied to avoid a discontinuity at the end of the data set and to increase the number of the sample points to  $N^2$ . After the mean flow values were subtracted from the time traces a linear taper to the first and last 10% of the data is multiplied by

$$p_n = \begin{cases} \frac{1}{2} \left[ 1 - \cos\left(\frac{\pi n}{N_1}\right) \right] & 0 \leq n \leq N_1 \\ 1 & \text{elsewhere} \\ \frac{1}{2} \left[ 1 - \cos\left(\frac{\pi}{N_1}(n-N)\right) \right] & N-N_1 \leq n \leq N \end{cases} \quad (\text{A.4})$$

where  $N_1 = N/10$ .

After this tapering, zeros are added to the data samples so that a total sample length consists of  $2^{12}$ , or 4096 elements.

The Fourier transform of the discrete time data is then found by using an FFT algorithm based on the DFT pair A.2 and A.3. However one problem always arises when estimating the discrete spectra because of the finite length of the data. To represent the finite data length mathematically, the actual computationally generated data sequence  $u_{\text{comp}}$  can be expressed in terms of a sequence of infinite data length

$u_{\infty}(n)$  multiplied by a window function  $g(n)$  so that

$$u_{\text{comp}}(n) = u_{\infty}(n) g(n) \quad (\text{A.5})$$

with

$$g(n) = \begin{cases} 1 & n=0,1, \dots, N-1 \\ 0 & \text{elsewhere} \end{cases} \quad (\text{A.6})$$

In the Fourier transformed space the equation A.5 is expressed by

$$U_{\text{comp}}(m) = U_{\infty}(m) * G(m) \quad m=0,1, \dots, M-1 \quad (\text{A.7})$$

where  $U_{\infty}$  denotes the Fourier transform of the infinite data length record,  $m$  is the frequency index, and the asterisk denotes the convolution. The equation A.7 indicates that the computational Fourier transform is given by the true Fourier transform and its convolution with the window function in the frequency space. From the properties of the convolution integral, it is known that  $U_{\text{comp}}$  will approximate  $U_{\infty}$  only in the case when  $G(m)$  is confined to a narrow band of frequencies. In the limit, where  $G(m)$  approximates a delta function,  $U_{\text{comp}} = U_{\infty}$ . The wave packets in our computation consist of a nonperiodic signal which disappears once the disturbance has completely passed the recording station, thus leakage of frequency components through the sidebands of the window function (the taper function) plays a minor role. Instead, pruning of the nonperiodic signal by adding zeros to the time sequence greatly sharpens the peak of the box car function A.6 and improves the spectral estimate considerably. Finally, the amplitude spectrum  $A(m)$  and the phase spectrum  $\phi(m)$  of the Fourier transformed time data are found through the relationships

$$A(m) = (a_m^2 + b_m^2)^{1/2} \quad , \quad \phi(m) = \tan^{-1}\left(\frac{b_m}{a_m}\right). \quad (\text{A.8})$$

where  $a_m$  and  $b_m$  are the real and imaginary parts of  $U(m)$ , respectively.

The general relation between input and output in continuous time of a linear system is given by

$$y(t) = \int_{-\infty}^{\infty} h(\tau) x(t-\tau) d\tau \quad (\text{A.9})$$

For our computations we restrict the above integral to a physically realizable system by assuming that the input to the system for  $\tau < 0$  is zero. Then, by taking the Fourier transform on both sides of A.9, one arrives at:

$$Y(m) = H(m)X(m) \quad (\text{A.10})$$

where  $Y(m)$  and  $X(m)$  are the discrete Fourier Transform of the input and output signals respectively.

From the relation A.10, one can easily find the transfer function  $H(m)$ . The relation A.10 is strictly true only in the absence of any noise. In our numerical data, there will always be some computational noise present. This noise level is determined by the accuracy of the machine and the convergence criteria used in our numerical scheme. The convergence criteria is set so that the magnitude of the truncation is several orders lower compared to the level of flow perturbation.

The estimation of  $H(m)$  in A.14 is limited to the range of frequencies where neither  $X(m)$  or  $Y(m)$  is exactly zero. To avoid this mathematical dilemma of dividing by zero, a filter in the frequency domain is applied on  $H(m)$  whenever  $X(m)$  or  $Y(m)$  is below the machine accuracy. Below this threshold, the convolution loses all information, and reconstructing that frequency component becomes impossible. Since the transfer function gradually falls off to zero for higher frequency components, a simple step function filter is used when the threshold of machine accuracy is reached.

## Appendix B: Finite Difference Approximations for the Energy Equation

The integration domain is divided into  $N$  grid points in the  $x$ -direction and  $M$  grid points in the  $y$ -direction. The grid is uniform in both directions. In the following expressions, the subscripts  $m$  and  $n$  refer to constant grid lines in the  $y$ - and  $x$ -direction respectively. The subscript  $p$  denotes the time. As a result, the spatial coordinates are  $x = n\Delta x$  and  $y = m\Delta y$  and the time is  $t = p\Delta t$ .

The first derivative in time for  $p > 1$  at  $1 \leq n \leq N$  and  $1 \leq m \leq M$  is approximated by:

$$\frac{\partial \theta}{\partial t} \Big|_{n,m,p} = \frac{1}{2\Delta t} (3\theta_{n,m,p} - 4\theta_{n,m,p-1} + \theta_{n,m,p-2}) + O(\Delta t^2) \quad (\text{B.1})$$

and for  $p=1$ :

$$\frac{\partial \theta}{\partial t} \Big|_{n,m,p} = \frac{1}{\Delta t} (\theta_{n,m,p} - \theta_{n,m,p-1}) + O(\Delta t) \quad (\text{B.2})$$

where  $\theta$  is the temperature.

For the following spatial derivatives, the superscript  $p$  for the time has been dropped, and each derivative is evaluated at the current time step. Also the coordinate  $z$  refers to the either the streamwise ( $x$ ) or the wall normal direction ( $y$ ), respectively.

For  $2 \leq n \leq N-2$  and  $2 \leq m \leq M-2$ :

$$\frac{\partial \theta}{\partial z} \Big|_k = \frac{1}{12\Delta z} (\theta_{k-2} - 8\theta_{k-1} + 8\theta_{k+1} - \theta_{k+2}) + O(\Delta z^4) \quad (\text{B.3})$$

$$\frac{\partial^2 \theta}{\partial z^2} \Big|_k = \frac{1}{12\Delta z^2} (-\theta_{k-2} + 16\theta_{k-1} - 30\theta_k + 16\theta_{k+1} - \theta_{k+2}) + O(\Delta z^4) \quad (\text{B.4})$$

at  $m=1$  (the plate surface), the  $y$ -derivatives are given by:

$$\frac{\partial \theta}{\partial y} \Big|_1 = \frac{1}{120\Delta y} (-AF - 65\theta_0 + 40\theta_1 + 66\theta_2 - 40\theta_3 - \theta_4) + O(\Delta y^4) \quad (\text{B.5})$$

$$\frac{\partial^2 \theta}{\partial y^2} \Big|_1 = \frac{1}{120 \Delta y^2} (-AF + 145 \theta_0 - 304 \theta_1 + 174 \theta_2 - 16 \theta_3 + \theta_4) + O(\Delta y^4) \quad (\text{B.6})$$

$AF$  is a known scalar at the wall surface at the timestep  $p$ :

$$AF = 12 \Delta y^2 \cdot Pr \left[ \frac{\partial \theta}{\partial t} \Big|_{wall} - \frac{1}{Re Pr} \frac{\partial^2 \theta}{\partial x^2} \Big|_{wall} \right]. \quad (\text{B.7})$$

At the outflow boundary, at grid lines  $N$  and  $N-1$ , the first and second derivatives are approximated by:

$$\begin{aligned} \frac{\partial \theta}{\partial x} \Big|_N = \frac{1}{66 \Delta x} (-4 \theta_{N-3} + 27 \theta_{N-2} - 108 \theta_{N-1} + 85 \theta_N \\ - 18 \alpha^2 \Delta x^2 (\theta_N - \theta_N^{p=0})) + O(\Delta x^4) \end{aligned} \quad (\text{B.8})$$

$$\begin{aligned} \frac{\partial \theta}{\partial x} \Big|_{N-1} = \frac{1}{60 \Delta x} (+3 \theta_{N-5} - 20 \theta_{N-4} + 60 \theta_{N-3} - 120 \theta_{N-2} + 65 \theta_{N-1} \\ + 12 \theta_N) + O(\Delta x^4) \end{aligned} \quad (\text{B.9})$$

$$\begin{aligned} \frac{\partial^2 \theta}{\partial x^2} \Big|_{N-1} = \frac{1}{22 \Delta x^2} (-2 \theta_{N-3} + 30 \theta_{N-2} - 54 \theta_{N-1} + 26 \theta_N \\ + 2 \alpha^2 \Delta x^2 (\theta_N - \theta_N^{p=0})) + O(\Delta x^4) \end{aligned} \quad (\text{B.10})$$

At the grid line next to the inflow boundary  $n=1$ , and the grid line next to the upper boundary  $m = M-1$ , the following one-sided approximations are used for the  $y$ -derivatives

$$\frac{\partial \theta}{\partial y} \Big|_{M-1} = \frac{1}{12 \Delta y} (3 \theta_{M+10} + 10 \theta_{M-1} - 18 \theta_{M-2} + 6 \theta_{M-3} - \theta_{M-4}) + O(\Delta y^4) \quad (\text{B.11})$$

$$\frac{\partial^2 \theta}{\partial y^2} \Big|_{M-1} = \frac{1}{12 \Delta y^2} (10 \theta_{M+10} - 15 \theta_{M-1} - 4 \theta_{M-2} + 14 \theta_{M-3} - 6 \theta_{M-4} + \theta_{M-5}) + O(\Delta y^4) \quad (\text{B.12})$$

The temperature dependent terms of the vorticity transport equation (2.3) are reformulated with

$$R_1 = \frac{\partial v}{\partial x} = v' \cdot \frac{\partial \theta}{\partial x} \quad (\text{B.13})$$

$$R_2 = \frac{\partial v}{\partial y} = v' \cdot \frac{\partial \theta}{\partial y} \quad (\text{B.14})$$

$$R_3 = \frac{\partial^2 v}{\partial x^2} = v'' \cdot \left[ \frac{\partial \theta}{\partial x} \right]^2 + v' \cdot \frac{\partial^2 \theta}{\partial x^2} \quad (\text{B.15})$$

$$R_4 = \frac{\partial^2 v}{\partial y^2} = v'' \cdot \left[ \frac{\partial \theta}{\partial y} \right]^2 + v' \cdot \frac{\partial^2 \theta}{\partial y^2} \quad (\text{B.16})$$

$$R_5 = \frac{\partial^2 v}{\partial y^2} = v'' \cdot \frac{\partial \theta}{\partial x} \frac{\partial \theta}{\partial y} + v' \cdot \frac{\partial^2 \theta}{\partial x \partial y} \quad (\text{B.17})$$

The prime on the viscosity  $v$  indicates a derivative with respect to temperature  $\theta$ , which is known analytically from equation (2.7).

With the above approximations the temperature dependent terms can be evaluated:

$$R_1|_{n,m} = v' \cdot \frac{1}{12\Delta x} (\theta_{n-2,m} - 8\theta_{n-1,m} + 8\theta_{n+1,m} - \theta_{n+2,m}) \quad (\text{B.18})$$

$$R_2|_{n,m} = v' \cdot \frac{1}{12\Delta y} (\theta_{n,m-2} - 8\theta_{n,m-1} + 8\theta_{n,m+1} - \theta_{n,m+2})$$

$$R_3|_{n,m} = v'' \cdot \frac{1}{144\Delta x^2} (\theta_{n-2,m} - 8\theta_{n-1,m} + 8\theta_{n+1,m} - \theta_{n+2,m})^2 \quad (\text{B.21})$$

$$+ v' \cdot \frac{1}{12\Delta x^2} (-\theta_{n-2,m} + 16\theta_{n-1,m} - 30\theta_{n,m} + 16\theta_{n+1,m} - \theta_{n+2,m})$$

$$R_4|_{n,m} = v'' \cdot \frac{1}{144\Delta y^2} (\theta_{n,m-2} - 8\theta_{n,m-1} + 8\theta_{n,m+1} - \theta_{n,m+2})^2 \quad (\text{B.22})$$

$$+ v' \cdot \frac{1}{12\Delta y^2} (-\theta_{n,m-2} + 16\theta_{n,m-1} - 30\theta_{n,m} + 16\theta_{n,m+1} - \theta_{n,m+2})$$

$$R_5|_{n,m} = v'' \cdot \frac{1}{144\Delta y \Delta x} (\theta_{n,m-2} - 8\theta_{n,m-1} + 8\theta_{n,m+1} - \theta_{n,m+2}) \quad (\text{B.23})$$

$$(\theta_{n-2,m} - 8\theta_{n-1,m} + 8\theta_{n+1,m} - \theta_{n+2,m})$$

$$+ v' \cdot \frac{1}{144\Delta x \Delta y} (\theta_{n-2,m-2} - 8\theta_{n-1,m-2} + 8\theta_{n+1,m-2} - \theta_{n+2,m-2}$$

$$- \theta_{n-2,m-1} + 64\theta_{n-1,m-1} - 64\theta_{n+1,m-1} + 8\theta_{n+2,m-2}$$

$$+ 8\theta_{n-2,m+1} - 64\theta_{n-1,m+1} + 64\theta_{n+1,m+1} - 8\theta_{n+2,m+1}$$

$$+ \theta_{n-2,m+2} + 8\theta_{n-1,m+2} - 8\theta_{n+1,m+2} + \theta_{n+2,m+2})$$

## List of References

- Bestek, H., (1980) *Numerische Untersuchungen zur nichtlinearen räumlichen Störungsanfängung in der ebenen Poiseuille-Strömung*, Dissertation, Universität Stuttgart, Germany.
- Bestek, H., P. Dittrich and H. Fasel, (1987) *Einfluss der Wandtemperatur auf die Entwicklung von Tollmien-Schlichting Wellen in der Grenzschichtströmung*, ZAMM, 67, 5, pp. 256-258, E. Germany.
- Brown, G. L., (1967) *Theory and Application of Heated Films for Skin Friction Measurement*, Proceedings of the 1967 Heat Transfer and Fluid Mechanics Institute, p18.
- Bushnell, D. M., and M. R. Malik, (1985) *Application of Stability Theory to Laminar Flow Control - Progress and Requirements*, ICASE/NASA Workshop on Stability of Time Dependent and Spatially Varying Flows, Springer-Verlag, Eds. D. L. Dwoyer and M.Y. Hussaini.
- Chatfield, C., "The Analysis of Time Series", 4th ed., Chapman and Hall Ltd, London, 1989.
- Craik, A. D. D., (1971) *Nonlinear resonant instability in boundary layers.*, J. Fluid Mech. 50, pp 393-413.
- Corke, T. C., (1989) *Resonant Three Dimensional Modes in Transitioning Boundary Layers - Structure and Control*, AIAA 89-1001, Tempe, Arizona.
- Dittrich, P. A., (1985) *Numerische Integration der Navier-Stokes und Energiegleichung zur Untersuchung der Stabilität der Grenzschichtströmung entlang einer ebenen Platte*, Diplomarbeit, Universität Stuttgart.
- Drazin, P. G. and W. H. Reid, "Hydrodynamic Stability", Cambridge University Press, Cambridge, England, 1981.
- Fasel, H., (1976) *Investigation of the Stability of Boundary Layers by a Finite-Difference Model of the Navier-Stokes Equations*, J. Fluid Mech., Vol. 78, pp. 355-383.
- Fasel, H., (1983) *Numerical Simulation of Nonlinear Growth of Wave Packets in a Boundary Layer*, Proc. IUTAM Symposium on Turbulence and Chaotic Phenomena in Fluids, Kyoto, Japan.

- Fasel, H. F., U. Rist and U. Konzelmann, (1987) *Numerical Investigation of the Three-Dimensional Development in Boundary Layer Transition*, AIAA-87-1203, Honolulu, Hawaii.
- Fasel, H. F. and U. Konzelmann, (1990) *Non-parallel stability of a flat-plate boundary layer using the complete Navier-Stokes equation*, J. Fluid Mech., Vol 221, pp311-347.
- Gaster, M. and I. Grant, (1975) *An experimental investigation of the formation and development of a wave packet in a laminar boundary layer*, Proc. R. Soc. Lond., A. 347, pp. 253-269.
- Gaster, M., (1975) *A theoretical model of a wave packet in the boundary layer on a flat plate*, Proc. R. Soc. Lond., A. 347, pp. 271-289
- Gaster, M., (1984) *A non-linear transfer function description of wave growth in a boundary layer* Laminar Turbulent Transition, IUTAM Symposium, Editor V.V. Kozlov, Novosibirsk, USSR p.107-114
- Grosch, E. C. and H. Salwen, (1978) *The continuous spectrum of the Orr-Sommerfeld equation. Part 1. The spectrum and the eigenfunctions*, JFM 87, 33-54.
- Herbert, T., (1984) *Analysis of the Subharmonic Route to Transition in Boundary Layers*, AIAA - 84 - 0009, Reno, Nevada.
- Jordinson, R., (1971) *Spectrum of eigenvalues of the Orr-Sommerfeld equation for Blasius flow*, Phys. Fluids 14, 2535-7, p156.
- Kachanov, Y. S., and V. Y. Levchenko, (1984) *The Resonant Interaction of Disturbances at Laminar-Turbulent Transition in a Boundary Layer*, J. Fluid Mech., vol. 138, pp. 209-247.
- Klebanoff, P. S., K. D. Tidstrom, and L.M. Sargent, (1962) *The Three-Dimensional Nature of Boundary-Layer Instability*, J. Fluid Mech., vol. 12, pp. 1-41.
- Kloker, M., U. Konzelmann and H. Fasel, (1991) *Outflow Boundary Conditions for Spatial Navier-Stokes Simulations of Laminar-Turbulent Transition in Boundary Layers*, AIAA Journal (to be published).
- Konzelmann, U., (1991) *Numerische Untersuchungen zur räumlichen Entwicklung dreidimensionaler Wellenpakete in einer Plattengrenzschichtströmung*, Dissertation, Universität Stuttgart.

- Kral, L. D., (1988) *Numerical Simulation of Three-Dimensional Transition Control in a Flat Plate Boundary Layer*, Dissertation, University of Arizona, Tucson.
- Kral, L. D. and H. F. Fasel, (1989) *Numerical Investigation of the Control of the Secondary Instability Process in Boundary Layers*, AIAA 89-0984, Tempe, Arizona.
- Lenz, K., (1986) *Numerische Simulation der Ausbreitung von Wellenpaketen in einer Laminaren Grenzschicht Strömung*, Dissertation, Universität Stuttgart.
- Liepmann, H. W., G. L. Brown, and D. M. Nosenchuck, (1982a) *Control of Laminar-Instability Waves Using a New Technique*, J. Fluid Mech., vol. 118, pp. 187-200.
- Liepmann, H. W. and D. M. Nosenchuck, (1982b) *Active Control of Laminar-Turbulent Transition*, J. Fluid Mech., vol. 118, pp. 200-204.
- Laurien, E. and L. Kleiser, (1989) *Numerical simulation of boundary layer transition and transition control*, J. Fluid Mech., vol. 199, pp. 403-440.
- Lowell, R. L., (1974) *Numerical Study of the Stability of a Heated, Water Boundary Layer*, Dissertation, Case Western Reserve University.
- McMurray, J. T., R. W. Metcalfe, and J. J. Riley, (1983) *Direct Numerical Simulation of Active Stabilization of Boundary Layer Flow*, Proc. of the Eighth Biennial Symposium on Turbulence, University of Missouri.
- Milling, R. W., (1981) *Tollmien-Schlichting Wave Cancellation*, Phys. Fluids, vol. 24, no. 5.
- Nygaard, K. J., (1991) *Spanwise-nonuniform excitation and active control of a plane mixing layer* Dissertation, University of Arizona, Tucson.
- Nosenchuck, D. M., (1982) *Passive and Active Control of Boundary Layer Transition*, Dissertation, California Institute of Technology.
- Pupator, P. and W. Saric, (1989) *Control of Random Disturbances in a Boundary Layer*, AIAA 89-1007, Tempe, Arizona.
- Robey, H. F., (1986) *On the nature of oblique instability waves in boundary layer transition*, Dissertation, Cal. Inst. of Tech., Pasadena.

- Saric, W. S. and A. S. W. Thomas, (1983) *Experiments on the Subharmonic Route to Turbulence in Boundary Layers* Proc. IUTAM Symposium on Turbulence and Chaotic Phenomena in Fluids, Kyoto, Japan.
- Schlichting, H., "Grenzschicht-Theorie", Verlag G. Braun, Karlsruhe, Germany, 1982.
- Schubauer, G. B. and H. K. Skramstad, (1948) *Laminar Boundary-Layer Oscillations and Transition on a Flat Plate*, NACA Report No. 909, pp. 327-357.
- Strazisar, A. J., E. Reshotko, and J. M. Prahl, (1977) *Experimental Study of the Stability of Heated Laminar Boundary Layers in Water*, J. Fluid Mech., vol. 83, pp. 225-247.
- Thomas, A. S. W., (1983) *The Control of Boundary-Layer Transition Using a Wave-Superposition Principle*, J. Fluid Mech., vol. 137, pp. 233-250.
- Truckenbrodt, E., "Fluidmechanik, Band 1", Springer Verlag 1981.
- Wagner, R. D., D. W. Bartlett, and F. S. Collier, (1989) *Laminar Flow- The Past, Present and Prospects*, AIAA 89-0989, Tempe, Arizona.
- Wazzan, A. R., T. T. Okamura, and A. M. O. Smith, (1968) *The Stability of Water Flow Over Heated and Cooled Flat Plates*, J. of Heat Transfer, pp. 109-114.
- Wehrmann, O. H., (1965) *Tollmien-Schlichting Waves under the Influence of a Flexible Wall*, Physics Fluids, 8, pp 1389-1390.